



저작자표시-비영리-변경금지 2.0 대한민국

이용자는 아래의 조건을 따르는 경우에 한하여 자유롭게

- 이 저작물을 복제, 배포, 전송, 전시, 공연 및 방송할 수 있습니다.

다음과 같은 조건을 따라야 합니다:



저작자표시. 귀하는 원저작자를 표시하여야 합니다.



비영리. 귀하는 이 저작물을 영리 목적으로 이용할 수 없습니다.



변경금지. 귀하는 이 저작물을 개작, 변형 또는 가공할 수 없습니다.

- 귀하는, 이 저작물의 재이용이나 배포의 경우, 이 저작물에 적용된 이용허락조건을 명확하게 나타내어야 합니다.
- 저작권자로부터 별도의 허가를 받으면 이러한 조건들은 적용되지 않습니다.

저작권법에 따른 이용자의 권리는 위의 내용에 의하여 영향을 받지 않습니다.

이것은 [이용허락규약\(Legal Code\)](#)을 이해하기 쉽게 요약한 것입니다.

[Disclaimer](#)

공학박사학위논문

**A study on the microstructure  
formation and drying behavior of  
Li-ion battery anode slurry**

리튬 이온 배터리 음극 슬러리의 미세 구조와  
건조 거동에 관한 연구

2015년 8월

서울대학교 대학원

화학생물공학부

임 상 혁

# **A study on the microstructure formation and drying behavior of Li-ion battery anode slurry**

리튬 이온 배터리 음극 슬러리의 미세구조와  
건조 거동에 관한 연구

지도 교수 이 승 중

이 논문을 공학박사 학위논문으로 제출함  
2015년 7월

서울대학교 대학원  
화학생물공학부  
임 상 혁

임상혁의 공학박사 학위논문을 인준함  
2015년 7월

위원장	<u>안 경 현</u>	(인)
부위원장	<u>이 승 중</u>	(인)
위원	<u>성 영 은</u>	(인)
위원	<u>남 재 욱</u>	(인)
위원	<u>정 현 욱</u>	(인)

## **Abstract**

# **A study on the microstructure formation and drying behavior of Li-ion battery anode slurry**

Sanghyuk Lim

School of Chemical and Biological Engineering

Seoul National University

The effect of binders used in Li-ion battery anode slurry on the microstructure formation and drying behavior was investigated. The microstructure formation of the anode slurry was studied by analyzing the rheological properties and cryo-SEM images. The graphite particles aggregated with each other due to their hydrophobicity and formed a gel structure in an aqueous slurry. In the case of graphite/SBR slurry, the microstructure was changed from the gel structure formed by graphite particles to dispersion due to the adsorption of SBR on the graphite surface. In the graphite/CMC slurry, the structural change was observed which was from gel to dispersion by adsorbing CMC on the graphite surface as in the graphite/SBR slurry. On the other hand, the dispersion was changed to gel structure again at high CMC concentration because the CMC molecules formed a network structure at high concentration and the polymeric network structure played a dominant role in the gel behavior of the battery slurry. In the

graphite/CMC/SBR slurry, the SBR could affect the dispersion of the graphite particles at low CMC concentration in the slurry, while the microstructure was not changed regardless of adding SBR at high CMC concentration because the SBR could not adsorb on the graphite surface due to the CMC which was preferably adsorbed on the graphite.

The drying behavior of the anode slurry was investigated by measuring the drying stress and by observing the microstructure in the dried film. The drying stress and the microstructure of the film were evaluated by a cantilever deflection method and a mercury intrusion porosimetry, respectively. We discovered that the SBR in the graphite/SBR slurry fills the voids among the graphite particles as the SBR concentration increases. In addition, the CMC in graphite/CMC slurry surrounded the particles by adsorbing on the surface of the graphite particles, thus helping the graphite particles to get together. In the case of graphite/CMC/SBR slurry, the effect of SBR on the drying stress depended on the CMC concentration. The residual stress increased as the SBR concentration was increased at low CMC concentration, while it maintained constant although the SBR concentration was increased at high CMC concentration. The residual stress in the film could be regarded as the mechanical strength of the film. In order to increase the mechanical strength of the film in low concentration region of CMC, a large amount of SBR was needed. On the other hand, in high concentration region of CMC, the SBR did not affect the mechanical strength of the film any longer. In other words, the CMC played a leading role in enhancing the mechanical strength of the film. Based on the drying stress of the slurries, we could draw a processing window map that clearly showed the effect of CMC and SBR on the mechanical strength of the film, which will be useful in the design of anode slurries.

In addition, the latex migration in anode slurries during drying process was investigated by replacing SBR with fluorescent PS particles. The time evolution of the fluorescence signals revealed the particle migration in the film during drying. In CMC solution without graphite, the migration of the latex particles was suppressed above the entanglement concentration of CMC because the CMC molecules interrupted the latex migration. Thus, the uniform distribution of the particles in the film was produced at high CMC concentration, while the latex was distributed non-uniformly due to the migration at low concentration of CMC. In anode slurry, the latex migration was affected by the microstructure of the slurry. When the graphite particles were aggregated by depletion attraction, the latex migration was observed. On the other hand, when the graphite particles were well dispersed by adsorbed CMC on the graphite surface, the latex particles neither migrated nor segregated.

This work provides the information about the effect of the binders, CMC and SBR used in anode slurry, on the microstructure formation and the drying behavior of the slurry. It is expected that the information about the microstructure and the drying behavior will be useful in designing the slurries for optimum performance of the Li-ion battery.

**Keywords:** Li-ion battery anode slurry, microstructure, drying stress development, film formation, latex migration

**Student Number:** 2012-30957

# Contents

Abstract.....	i
List of Contents.....	iv
List of Figures.....	viii
List of Tables.....	xv
<b>Chapter 1. Introduction.....</b>	<b>1</b>
1.1. General introduction.....	2
1.2. Outline of the thesis.....	7
<b>Chapter 2. Background.....</b>	<b>9</b>
2.1. Li-ion battery.....	10
2.1.1. Characteristics of Li-ion battery.....	10
2.1.2. Operating principle of Li-ion battery.....	11
2.1.3. Composition of Li-ion battery.....	11
2.2. Characteristics of particulate system.....	16
2.2.1. Yielding behavior of particulate system.....	16
2.2.2. Microstructure of particulate system.....	20
2.2.3. Microstructure of Li-ion battery.....	22
2.3. Drying process of particulate system.....	24
2.3.1. Drying mechanism.....	24
2.3.2. Drying stress of particulate system.....	30

2.3.2.1. Origin of drying stress.....	30
2.3.2.2. Stress development during drying process .....	33
2.3.2.3. Effect of drying temperature on drying stress.....	37
2.3.2.4. Effect of relative humidity on drying stress.....	37
2.4. Particle migration during drying .....	41
2.4.1. Particle migration in a vertical direction of film.....	41
2.4.2. Particle migration in a lateral direction of film.....	43
<b>Chapter 3. Experimental methods .....</b>	<b>47</b>
3.1. Sample preparation.....	48
3.2. Characterization of microstructure of battery slurry .....	51
3.2.1. Measurement of rheological property .....	51
3.2.2. Measurement of adsorption amount of CMC .....	51
3.2.3. Cryo-SEM .....	52
3.3. Measurement of drying stress development.....	54
3.4. Fluorescence microscopy during drying .....	57
3.5. Characterization of microstructure of film.....	60
3.5.1. Pore size distribution in dried film.....	60
3.5.2. Images of dried film .....	61
<b>Chapter 4. Results and discussion .....</b>	<b>63</b>
4.1. Microstructure of anode slurry .....	64
4.1.1. Graphite/SBR slurry.....	64



4.1.2. Graphite/CMC slurry.....	70
4.1.3. Graphite/CMC/SBR slurry.....	85
4.2. Drying behavior of anode slurry .....	95
4.2.1. Graphite/SBR slurry.....	95
4.2.1.1. Drying stress of graphite/SBR slurry.....	95
4.2.1.2. Microstructure of film for graphite/SBR slurry.....	101
4.2.2. Graphite/CMC slurry.....	106
4.2.2.1. Drying stress of graphite/CMC slurry.....	106
4.2.2.2. Microstructure of film for graphite/CMC slurry.....	111
4.2.3. Graphite/CMC/SBR slurry.....	116
4.2.3.1. Drying stress of graphite/CMC/SBR slurry.....	116
4.2.3.2. Microstructure of film for graphite/CMC/SBR slurry.....	119
4.2.4. Processing window map for anode slurry .....	122
4.3. Latex migration during drying in anode slurry .....	125
4.3.1. Validation of intensity of fluorescent light.....	125
4.3.2. Latex migration in CMC solution .....	127
4.3.2.1. Evolution in particle consolidation layer .....	132
4.3.2.2. Suppressed migration in dense CMC solution.....	137
4.3.3. Latex migration in anode slurry .....	143
4.3.3.1. Accelerated migration in anode slurry .....	149
<b>Chapter 5. Summary.....</b>	<b>159</b>
<b>References .....</b>	<b>165</b>

국문 초록.....	181
<b>Curriculum Vitae.....</b>	<b>184</b>

## List of Figures

<b>Figure 2.1.</b> A schematic of cell configuration of the Li-ion battery and the electrochemical reactions during charge (a) and recharge (b) of the battery .....	13
<b>Figure 2.2.</b> Yielding behavior for graphite suspension in log-log plot of viscosity against shear stress; ■: 30wt%, ▼: 40wt% ◆: 50wt% of graphite particle .....	19
<b>Figure 2.3.</b> Schematic about difference between ideal stress-free state and actual drying state [81] .....	32
<b>Figure 2.4.</b> Drying stress development and weight loss of anode slurry during drying .....	36
<b>Figure 2.5.</b> The development of the drying stress for the anode slurry containing 50wt% of graphite and 0.7wt% of CMC at different drying temperature, 25 and 70 °C. The relative humidity is 40%.....	39
<b>Figure 2.6.</b> The development of the drying stress for the anode slurry containing 50wt% of graphite and 0.9wt% of CMC at different relative humidity from 20 to 80%. The drying temperature is 25 °C.....	40
<b>Figure 3.1.</b> Schematic of specimen preparation for cryo-SEM.....	53
<b>Figure 3.2.</b> Schematic of cantilever deflection measurement .....	56
<b>Figure 3.3.</b> (a) Schematic of drying apparatus, (b) image captured by CCD camera, (c) image captured by CCD beam profiler .....	59

**Figure 4.1.1.** Rheological properties of anode slurries containing 50 wt% of graphite and various concentration of SBR. (a) Viscosity as a function of shear rate and as a function of shear stress (inset in (a)); obtained from stress controlled (closed symbol) and rate controlled (open symbol) rheometer, (b) Storage (closed symbol) and loss (open symbol) moduli as a function of frequency; SBR concentration in (a) and (b): (●○) 0 wt%, (▲△) 3 wt%, (■□) 8 wt%, (▼▽) 15 wt%, (◆◇) 30 wt%.....66

**Figure 4.1.2.** Cryo-SEM images of anode slurries containing 50 wt% of graphite and different concentrations of SBR; (a)&(b) graphite 50wt% + SBR 3wt%, (c)&(d) graphite 50wt% + 30wt% ..... 69

**Figure 4.1.3.** Viscosity as a function of shear stress for anode slurries containing 50wt% of graphite and various concentration of CMC; (●) 0wt%, (▲) 0.07wt%, (▼) 0.1wt%, (×) 0.4wt%, (◆) 0.7wt%, (★) 1.0wt%, (■) 1.4wt%, (+) 1.7wt% ..... 72

**Figure 4.1.4.** Storage (closed symbol) and loss (open symbol) moduli as a function of frequency for anode slurries containing 50 wt% of graphite and various concentration of CMC; (●) 0wt%, (▲) 0.07wt%, (▼) 0.1wt%, (×) 0.4wt%, (◆) 0.7wt%, (★) 1.0wt%, (■) 1.4wt%, (+) 1.7wt%..... 73

**Figure 4.1.5.** The specific viscosity as a function of polymer concentration for the CMC solution..... 75

**Figure 4.1.6.** Storage (closed symbol) and loss (open symbol) moduli as a function of frequency for CMC solutions containing various concentration of CMC;

(●): 0.6wt%, (▲): 1.0wt%, (■): 1.4wt%, (▼): 2.0wt%, (◆):  
 3.0wt%. ..... 76

**Figure 4.1.7.** Tan  $\delta$  as a function of CMC concentration for anode slurries containing  
 50 wt% of graphite (●) and CMC solution (○)..... 79

**Figure 4.1.8.** Cryo-SEM images of anode slurries containing 50 wt% of graphite and  
 different concentrations of CMC; (a)&(b) graphite 50wt% + CMC  
 0.07wt%, (c)&(d) graphite 50wt% + CMC 0.7wt%, (e)&(f) graphite  
 50wt% + CMC 1.7wt%..... 80

**Figure 4.1.9.** Cryo-SEM images of 2wt% CMC solution with magnification of 15,000  
 (a) and 30,000 (b)..... 84

**Figure 4.1.10.** Rheological properties of anode slurries containing 50wt% of graphite,  
 0.07wt% of CMC, and various concentration of SBR. (a) Viscosity as a  
 function of shear rate; obtained from the stress controlled (closed symbol)  
 and rate controlled (open symbol) rheometer, (b) Storage (closed symbol)  
 and loss (open symbol) moduli as a function of frequency; (●○) 0 wt%,  
 (▲△) 2 wt%, (■□) 5 wt% of SBR concentration..... 86

**Figure 4.1.11.** Rheological properties of anode slurries containing 50wt% of graphite,  
 0.7wt% of CMC, and various concentration of SBR. (a) Viscosity as a  
 function of shear rate, (b) Storage (closed symbol) and loss (open  
 symbol) moduli as a function of frequency; (●○) 0 wt%, (▲△) 2 wt%,  
 (■□) 5 wt% of SBR concentration ..... 89

**Figure 4.1.12.** Rheological properties of anode slurries containing 50wt% of graphite,  
 1.7wt% of CMC, and various concentration of SBR. (a) Viscosity as a

function of shear rate, (b) Storage (closed symbol) and loss (open symbol) moduli as a function of frequency; (●○) 0 wt%, (▲△) 2 wt%, (■□) 5 wt% of SBR concentration ..... 90

**Figure 4.1.13.** Cryo-SEM images of anode slurries containing 50 wt% of graphite and different concentrations of CMC and SBR; (a)&(b) graphite 50wt% + CMC 0.07wt% + SBR 5wt%, (c)&(d) graphite 50wt% + CMC 0.7wt% + SBR 5wt%, (e)&(f) graphite 50wt% + CMC 1.7wt% + SBR 5wt% ..... 93

**Figure 4.1.14.** Enlarged image by Cryo-SEM for slurry containing 50wt% of graphite, 1.7wt% of CMC and 5wt% of SBR..... 94

**Figure 4.2.1.** Drying stress of graphite slurries containing 50wt% of graphite and various concentration of SBR. Drying temperature is 25°C and relative humidity is 20% ..... 99

**Figure 4.2.2.** Residual and maximum stress as a function of SBR concentration .... 100

**Figure 4.2.3.** SEM images of dried film for anode slurries containing 50wt% of graphite and various concentration of SBR: (a) graphite 50wt% + SBR 3wt%, (b) graphite 50wt% + SBR 8wt%, (c) graphite 50wt% + SBR 15wt%, and (d) graphite 50wt% + SBR 30wt%. Insets in (a) ~ (c) are enlarged images of surfaces, respectively..... 102

**Figure 4.2.4.** Pore size distribution in dried film containing 50wt% of graphite and various concentration of SBR. The interval in y-axis (horizontal grey dashed line) represents 1.5 mL/g ..... 104

<b>Figure 4.2.5.</b> Stress development of graphite slurries containing 50wt% of graphite and various concentration of CMC during drying. Drying temperature is 25 °C and relative humidity is 20 %.....	109
<b>Figure 4.2.6.</b> Final stress of battery slurries containing 50wt% of graphite as a function of CMC concentration.....	110
<b>Figure 4.2.7.</b> SEM images of the dried film for anode slurries containing 50wt% of graphite and different concentration of CMC: (a) graphite 50wt% + CMC 0.3wt%, (b) graphite 50wt% + CMC 1.7wt% .....	113
<b>Figure 4.2.8.</b> Pore size distribution of the dried film containing 50wt% of graphite and various concentration of CMC. The interval in y-axis (horizontal grey dashed line) represents 1.5 mL/g .....	114
<b>Figure 4.2.9.</b> Stress development of graphite slurries containing 50wt% of graphite and various concentration of CMC and SBR during drying. Drying temperature is 25 °C and relative humidity is 20 % .....	118
<b>Figure 4.2.10.</b> Pore size distribution in dried film containing 50wt% of graphite and various concentration of CMC and SBR. Each interval in y-axis (horizontal grey dashed line) represents 1.5 mL/g.....	121
<b>Figure 4.2.11.</b> Processing window map for dried film of anode slurry. Symbol X indicates poor mechanical strength, Δ indicates less mechanical strength and ○ indicates good mechanical strength of the film.....	124
<b>Figure 4.3.1.</b> Dependence of intensity of fluorescent light on coating height and concentration of fluorescent particles: (a) intensity of fluorescent light plotted as a function of coating height for various concentrations of latex	

particles and (b) normalized intensity of fluorescent light plotted as a function of latex concentration for various coating heights .....	126
<b>Figure 4.3.2.</b> Intensity of fluorescent light developed for latex-CMC suspension dried at various temperatures: (a) 0.5, (b) 1.0 wt% CMC solution and (c) divided regimes depending on the development of intensity of fluorescent light.....	128
<b>Figure 4.3.3.</b> Development of beam spot during drying of 0.5 wt% CMC solution: (a) at initial drying, (b) at minimum size of beam spot, (c) at end of constant rate period, and (d) during final drying.....	130
<b>Figure 4.3.4.</b> Development of beam spot during drying of 1.0 wt% CMC solution: (a) at initial drying, (b) at end of constant rate period, (c) during falling rate period, and (d) during final drying.....	131
<b>Figure 4.3.5.</b> (a) $\ln \eta_{rel}/c$ and $\eta_{sp}/c$ plotted as functions of CMC concentration. (b) log-log plot of specific viscosity plotted as function of CMC concentration.....	140
<b>Figure 4.3.6.</b> Development of intensity of fluorescent light emitted from graphite slurries at 70°C.....	145
<b>Figure 4.3.7.</b> Images for 1 (a)–(c), and 5 wt% (d)–(f) graphite slurries: (a) and (d) are coating surfaces observed using optical microscope, (b) and (e) are coating surfaces observed using atomic force microscope, and (c) and (f) are cross-sections observed using SEM.....	146



**Figure 4.3.8.** Development of intensity of fluorescent light emitted from 5wt% graphite suspension depending on CMC concentration at various drying temperatures: (a) 0.5 and (b) 1.0wt% CMC..... 148

**Figure 4.3.9.** Isotherms for CMC adsorption onto surface of graphite particles, plotted as function of CMC concentration and ratio of CMC/graphite (graphite concentration was 5wt%)..... 151

**Figure 4.3.10.** Sedimentation behavior of graphite slurries depending on concentration of CMC. (a) 5wt% graphite slurry (ratio of CMC/graphite varied from 0 to 0.2) and (b) 1wt% graphite slurry containing 0.7wt% CMC (ratio of CMC/graphite is 0.7)..... 154

**Figure 4.3.11.** Critical development of intensity of fluorescent light emitted from graphite-free suspension ( $\circ$ ) and 5wt% graphite slurry ( $\Delta$ ) plotted as functions of CMC concentration at 30°C of drying temperature: (a) minimum, (b) maximum, and (c) final intensity of fluorescent light..... 158

## List of Tables

<b>Table 4.2.1.</b> Average pore diameter and porosity for dried film containing 50wt% of graphite and various concentration of SBR .....	105
<b>Table 4.2.2.</b> Average pore diameter and porosity for dried film containing 50wt% of graphite and various concentration of CMC.....	115
<b>Table 4.3.1.</b> Constants and dimensionless numbers for latex particles in 0.5 wt% CMC solution .....	136



# **Chapter 1.**

## **Introduction**

## 1.1. General introduction

Li-ion battery is a secondary battery that can charge and discharge through moving lithium ions. It consists of cathode and anode, which contain active materials made of lithium oxide and carbon, respectively. The Li-ion battery has a lot of advantage such as high energy density, high voltage, long life cycle, and no memory effect [1-5]. In addition, stability is better compared to other batteries which consist of Li-metals. Hence the Li-ion battery has been used in many areas, ranging from portable devices such as laptop, digital camera, and smart phone, to huge equipment such as electric vehicle, satellite, and so on. With this trend of battery application, it is required to enhance battery performances and stability of the Li-ion battery. Therefore, there are many efforts to solve various issues such as improvement of energy density, electrical stability, and safety problems.

The Li-ion battery is a typical particulate system which consists of graphite or carbon black as a particle, PVDF or CMC as a binder, and organic or aqueous medium as a solvent. Previously, polyvinylidene difluoride (PVDF) has been used as a binder in the organic solvent for anode slurry. However, an aqueous system is preferred over the non-aqueous system due to a high cost and safety problems. The advantages of the aqueous anode slurry are low cost, environment-friendly, and fast drying during manufacturing process of electrode [6]. So, the PVDF in non-aqueous system needs to be changed to CMC and SBR as binders in aqueous system. Sodium carboxymethyl cellulose (CMC) has been used as a thickening agent, binder, stabilizer, etc. in various industries such as food, cosmetics, battery, paper, and pharmaceutical industry [7-11]. Especially, the

CMC has been used as a thickening agent for the aqueous anode slurry to prevent the sedimentation of the particles. The CMC is a linear polymeric derivative of cellulose which contains two anhydroglucose units ( $\beta$ -linked glucopyranose residues) with each anhydroglucose unit having three hydroxyl groups. The hydrogen in hydroxyl group is substituted by carboxymethyl group, and the average number of hydroxyl groups substituted per anhydroglucose unit is defined as a degree of substitution (DS). When all hydroxyl groups are substituted, the DS value is 3. The CMC shows a variety of characteristics depending on the concentration, molecular weight, pH, DS, and so on [10-17]. Lee et al. [11] investigated the effect of DS of CMC on the electrokinetic behavior and the electrochemical performance of the anode. As the DS becomes lower, the adsorption amount of CMC on the graphite particles becomes larger than the CMC with higher DS because the interaction of low DS CMC with graphite particles becomes stronger. The adsorption amount of CMC affects the dynamic mobility and dispersion stability of graphite particles in the suspension. Furthermore, it also affects the electrochemical performance of the anode such as charge-discharge capacity and adhesion strength. Styrene-butadiene rubber (SBR) has been used as a reinforcing agent, binder, flexibility enhancer, etc. in many industries such as tire, paper, membrane, battery, and so on [18-23]. The SBR is a kind of synthetic rubber consisting of styrene and butadiene units. The SBR in the anode slurry is used as a binder to enhance the adhesion force between the film and the current collector.

There are many on-going researches on Li-ion batteries to improve their performance and stability. In the case of a cathode, for example, the battery performance can be enhanced by controlling the dispersion state of the particles, such as active material or

carbon black, through the improvement of manufacturing protocol [24,25] and adding additives [26-28]. Meanwhile, the anode has to meet the characteristics such as high energy density and good mechanical strength [5,29]. There are many researches about active materials and binders in order to manufacture anodes with high energy density [5]. An anode film must have the mechanical strength which is the adhesion strength between film and copper foil in order to attain good electrochemical performance such as cyclability and specific capacity [29,30]. Lee et al. [29] reported the effect of poly (acrylic acid) (PAA) on both the adhesion strength and the electrochemical performance. PAA can improve the dispersion state of the particles and the adhesion strength between the film and substrate by adsorbing on the surface of graphite particles. The slurry containing both CMC and PAA showed a much better dispersion, adhesion strength, and electrochemical performance than that containing only CMC. Nguyen et al. [30] reported the effect of poly (acrylic-co-maleic) acid (PAMA) on the slurry dispersion and the effect of dispersion on the battery performance. For example, by adding PAMA into the slurry, the dispersion of carbon black was reinforced, and the porosity in the dried film was also decreased. In other words, the better the dispersion state of the particles in the film was, the more improvement in the battery performance was observed. On the other hand, if the excessive PAMA was added into the slurry, the battery performance got worse again. Thus, there exists an optimum concentration of PAMA for the best performance. Therefore, in the design of battery slurry, it is important to understand the microstructure which is formed by the interaction between the particle and polymer, and to optimize the composition in order to improve the battery performance.

The graphite particles tend to be aggregated in an aqueous solvent due to non-polar surface and hydrophobicity, and the dispersion of carbon particles in an aqueous solution is one of the crucial issues. It is also important to understand the effect of CMC and SBR on the dispersion of graphite particles as well as on the microstructure formation of the slurry in the aqueous anode slurry. However, there is a lack of studies about the mechanism of microstructure formation by binders in the aqueous anode slurry.

With the composition design, it is important to understand the drying process in order to obtain optimum battery performance and the microstructure of the film. There have been many efforts to understand the microstructure formation for the particulate systems during drying. For instance, the microstructure formation during drying was investigated both directly and indirectly by small-angle X-ray scattering [31], diffusing wave spectroscopy [32], Cryo-SEM [33,34], fluorescence microscopy [35], Raman spectroscopy [23], modelling [33]. In particular, Lim et al. [35] and Hagiwara et al. [23] investigated the latex migration in anode slurries during drying process. Porcher et al. [36] and Li & Wang [37] investigated the effect of particle distribution in film on the performance of the battery, and concluded that the homogeneous morphology of the electrode induced good electrochemical performance of the battery. Most of researches focused on the microstructure formation during drying, however the research on the drying mechanism has rarely been performed yet.

Stress is developed due to the shrinkage of coating liquid while it dries. The drying stress can induce film defects such as crack, curl, and delamination. In order to manufacture the film with good mechanical performance, it is important to understand



the mechanism of stress development during drying. When the coatings are coated onto a substrate, in-plane tensile stress is developed due to the constrained shrinkage [38]. The cantilever deflection method can measure the in-plane stress during drying, and has been used to characterize the drying mechanism for polymer solutions [38-40] and suspensions [41-50].

In this thesis, the microstructure and drying behavior for Li-ion battery anode slurry is introduced. Firstly, the microstructure of the anode slurry is investigated by analyzing the rheological properties of the slurry. In addition, the microstructure can be confirmed by cyro-SEM images. Secondly, the behavior of anode slurries is quantified by measuring the stress which is developed during drying process. The effect of binders on the microstructure formation is also investigated by analyzing the pore size distribution in the dried film. In addition, an optimum formulation guideline is suggested for obtaining the film with sufficient mechanical strength in a slurry. In order to figure out the effect of binders on the microstructure formation and the drying behavior of the anode slurry, I investigate the three different kinds of anode slurry; graphite/SBR, graphite/CMC, and graphite/CMC/SBR. Finally, particle migration in the anode slurry during drying is investigated by fluorescence microscopy.

## 1.2. Outline of the thesis

The thesis consists of background, experimental methods, and results and discussion chapters.

Chapter 2 describes the background of the thesis which is divided into Li-ion battery, characteristics of particulate system and drying process. The first part of Chapter 2 describes about the characteristics and compositions of Li-ion battery. The second part of Chapter 2 explains the yielding behavior which can appear in concentrated suspension or slurry and the microstructure of particulate system which is affected by the polymer concentration such as bridging and depletion flocculation. In addition, some researches about the microstructure of Li-ion battery are introduced in the second part of Chapter 2. The last part of Chapter 2 describes drying process of particulate system. Firstly, the drying mechanism which the solidifying process of the coating from liquid to solid state is introduced. In addition, the drying stress of particulate system is described which consists of origin of drying stress, stress development during drying process and the effect of drying temperature and relative humidity on the drying stress. Finally, the particle migration which can occur in a vertical and lateral direction of film during drying is describes.

Chapter 3 describes the information of materials such as graphite particle, sodium carboxymethyl cellulose (CMC) and styrene-butadiene rubber (SBR) used in the thesis, and the characterization of microstructure and drying behavior for battery slurry. One of the majorities of the thesis is to establish the effect of binders, such as SBR and CMC, on the microstructure formation and drying stress development for anode slurry. So, the

measurement of rheological properties and cryo-SEM to investigate the microstructure formation and the cantilever deflection method to investigate the development of drying stress are introduced in Chapter 3. In addition, the fluorescence microscopy which can detect the migration of particles during drying in real time is described. Finally, the mercury intrusion porosimetry (MIP) which is used to characterize the microstructure of dried film is introduced.

Chapter 4 describes the results about microstructure formation and drying behavior of battery slurry. In Chapter 4.1, the microstructure of the anode slurry by analyzing the rheological properties of the slurry is described. In addition, the cryo-SEM images can confirm the microstructure in liquid-state of the slurry. The effect of binders on the microstructure formation of the slurry is discussed by investigating the graphite/SBR, graphite/CMC and graphite/CMC/SBR slurry, separately. In Chapter 4.2, the behavior of anode slurry is quantified by measuring the stress which is developed during the drying process. In addition, the effect of binders on the microstructure of the dried film is described by analyzing the pore size distribution in the film. Finally, an optimum formulation guideline for obtaining the film with sufficient mechanical strength in a slurry containing both CMC and SBR is introduced. Chapter 4.3 describes the latex migration during drying in anode slurry. The fluorescence microscopy which is a method to measure the particle migration in drying film is described.

Chapter 5 summarizes the results on the works about the microstructure and drying behavior of Li-ion battery anode slurry.

## **Chapter 2.**

# **Background**

## **2.1. Li-ion battery**

### **2.1.1. Characteristics of Li-ion battery**

A rechargeable battery is a type of chemical battery which can be repeatedly charge and discharge by reversible interconversion between chemical and electrical energy. Historically, Lead acid and Ni-Cd have been widely used, but the energy density reached the technical limit and an environmental regulation was introduced. So, Ni-MH and Li-rechargeable battery were developed to replace the Lead acid and Ni-Cd batteries. Li-rechargeable battery is divided into Li-ion, Li-ion polymer, Li-metal polymer batteries. In this thesis, the Li-ion battery will be discussed.

Li-ion battery has many advantages such as high energy density, high capacity per unit area, and minimal-self discharge comparing with Ni-Mn or Ni-Cd batteries. In addition, it has no memory effect, so it shows characteristic of long life cycle. However, there also exist some disadvantages of Li-ion battery. Because the Li-ion is delivered through electrolyte, the battery can explode when the electrolyte leaks and is exposed to the air. In addition, the pressure in the battery case increases by chemical reaction and the battery can explode when the battery is overcharged, so the protective circuit has to be adopted to shut out the over-activation. Li-ion battery has been used in various industries such as cell phone, laptop, electric vehicle, and so on. Thus, the researches on weight reduction and low power technology of the battery for miniaturizing and high capacity are required.

### 2.1.2. Operating principle of Li-ion battery

A basic operating principle of the battery is based on the behavior of electron transfer which appears due to a potential difference between materials. Li-ion battery consists of cathode, anode, electrolyte, and separator. Figure 2.1 shows the schematic of cell configuration of the Li-ion battery and the electrochemical reactions during charging and recharging of the battery. The half-reaction of the cathode is given as



and the half-reaction of the anode is given as



When the Li-ion battery is charging, the Li ions are extracted from the cathode and it moves through the electrolyte followed by inserts into the anode. When the battery is discharging, the reverse takes place.

### 2.1.3. Composition of Li-ion battery

#### *Cathode*

A cathode consists of active material, current collector, and binder. Priority purpose of the cathode is to embody maximum capacity of the battery. So, the quantity of the active materials needs to be as maximum as possible to increase the electrode density.

The electrode density depends on the characteristics of active material such as particle size, size distribution, and particle density. The structure of the active material for cathode is layered or three-dimensional because Li ions can insert and extract freely. The kinds of the active material for cathode are  $\text{LiCoO}_2$ ,  $\text{LiNiO}_2$ ,  $\text{LiMn}_2\text{O}_4$ , and so on. The electron conductivity of the active material is low because it is a type of ceramic material. Thus, an extra conductive material, such as carbon black or graphite powder, is needed.

### *Anode*

An anode consists of active material, current collector, and binder like the cathode. In the beginning, a Li metal is used as the active material for the anode. The Li-metal has large specific capacity (3,860mAh/g), thus having an excellent energy density. However, its low melting temperature and morphological irreversibility when oxidation-reduction reactions became a significant trouble. In addition, the dendrite which comes from the collapse and reformation of the Li-ion reducing the morphological irreversibility is a major cause of short circuit. So, a carbon-based material which can intercalate the Li ions (Lithium Intercalated Carbon; LIC) is used to solve the safety problem. The electrochemical potential of the carbon-based material with Li is close to a Li-metal, and there is little change of the formation of the crystal structure when electrochemical reactions. Therefore, the continuous oxidation-reduction reactions and long life cycle is possible when operating the battery. The graphite or carbon material is used as the LIC.

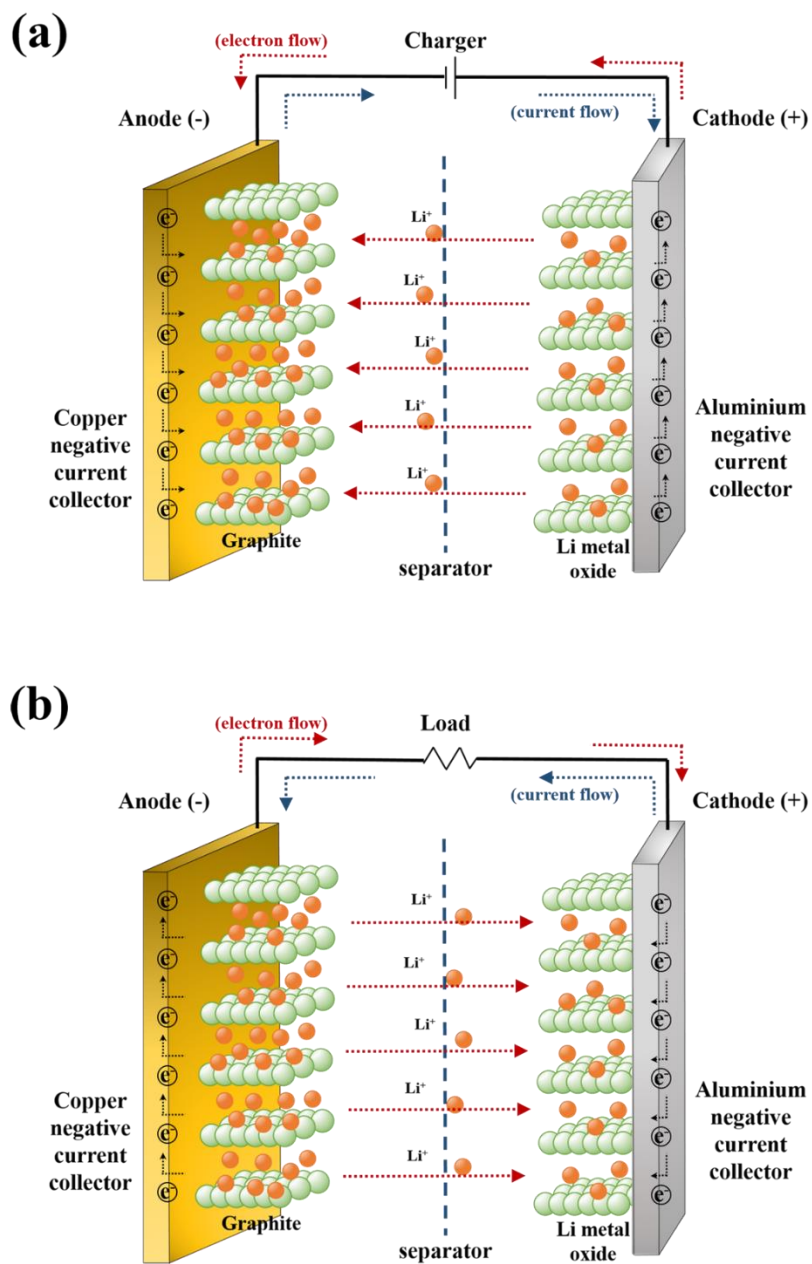


**Figure 2.1.** A schematic of cell configuration of the Li-ion battery and the electrochemical reactions during charge (a) and recharge (b) of the battery.



### ***Electrolyte***

The electrolyte play a role as a link to move the Li-ions between cathode and anode. The electrolyte is composed of a salt, solvent, and additives. In general, a Li-ion battery is imposed a ceiling on the power as 4.1~4.2V. In such high voltage, an electrolysis can occur in an aqueous solution, preventing the use of the aqueous solution as the solvent. Therefore, a non-aqueous solution is used as the solvent because it can withstand high voltage. The non-aqueous solution has to be a highly dielectric solvent. The dissociation degree of ion is large in the highly dielectric solvent, and it is possible to have many Li ions existing in the solvents. The viscosity of the electrolyte has to be low because the Li ions have to move easily. In addition, the electrolyte has to be stable chemically and electrically because it must not react with other component of the battery. The Lithium salt, such as  $\text{LiPF}_6$ , is used in electrolyte because of its high ion conductivity and stable characteristic. Various characteristics of the electrolyte can be achieved according to the kinds of salt or solvent, concentration of salt, mixture ratio, and so on. Thus, the composition in the electrolyte have to be optimized according to the kind of electrodes used. An anti-overcharge is used to prevent overcharge of the battery as additive in the electrolyte.

### ***Separator***

A separator is used to prevent a short circuit by separating the cathode and the anode. The Li ions as well as the electrolyte can migrate through the micro pores in the separator except for the electron. General properties of the separator are 1) to separate the cathode and the anode in order to prevent a short circuit by physical contact of two

electrodes, 2) to have characteristic of electrical insulation for membrane material, 3) to have good penetrability of electrolyte and ion, and low electric resistance, 4) to be stable chemically and electrochemically for electrolyte, 5) to have good wettability in electrolyte, 6) to be able to form a thin membrane for high density packing of battery, 7) to have good physical properties, and 8) to secure the stability of battery through shut-down of the pores in membrane when a short circuit occurs. The polyethylene (PE) and polypropylene (PP)-based membrane are widely used as the separator.

## **2.2. Characteristics of particulate system**

A particulate system consists of particle, polymer and solvent. It has been widely used in various industries such as paper, paint, display, battery, etc. In the particulate system, a variety of microstructure can be formed depending on the interaction between particles and binders, and it induces the change of rheological behavior as well as physical properties of the suspension or slurry. Therefore, it is important to understand and control the microstructure of the particulate for commercial success of the product in manufacturing industries.

### **2.2.1. Yielding behavior of particulate system**

It is widely understood that an increase in solid concentration is commonly characterized by an increase in suspension viscosity and escalating non-Newtonian flow behavior above a critical concentration. Flocculated systems common to filtration and dewatering processes typically exhibit these properties at very low solids fractions - concentrations significantly lower than the theoretical hard-sphere packing fraction of 0.64, ordinarily restricted to mono-dispersed spherical particles. As the particulate concentration of these flocculated systems increases, the suspension attains a critical concentration at which a continuous networked structure spans the vessel, classically defined as the gel point,  $\phi_g$ .

Suspensions at solids concentrations in excess of the gel point are observed to exhibit a yield stress,  $\tau_y$  - a measure of mechanical rigidity arising from attractive inter-particle forces between suspended particles [51-53]. Figure 2.2 shows the yielding behavior for

the graphite suspension. The plateau of the viscosity is observed at low shear region, indicating that the graphite suspension exhibits solid-like behavior. The viscosity started to decrease dramatically after a critical point, which is defined as the yield stress [54]. When the applied shear stress exceeds the yield stress, the graphite suspension exhibits liquid-like behavior. Yield stresses are exploited in a multitude of industrial systems to promote the efficient production, storage, transport and utilization of pigments, dyes, cosmetics, foodstuffs, pharmaceuticals, and of course, mineral systems. Slurry formulation with a consideration of suspension rheology and more importantly, the yield stress behavior, provides a more effective strategy for thickened tailings disposal through dry stacking or paste backfilling [55].

The relationship between suspension yield stress and parameters such as the state of dispersion, particle size, and particle shape has been investigated by a number of authors [52,53,56-60]. It is typically defined as the mechanical resistance that must be overcome before a networked structure fails and flow is detected. Traditional methods of measuring an yield value involved extrapolation of shear stress vs. shear rate curves to zero shear. However, accurate equilibrium data is difficult to obtain and reproduce when testing weakly-gelled systems with this model. To overcome many of the artefacts associated with weakly flocculated systems, Nguyen and Boger [61] adopted a static yield stress technique incorporating a vane. Correlation of yield stress to slump behavior is also widely used [62].

There is an abundance of existing literature investigating the link between surface chemistry, flow behavior, and yield stress [63-65]; more recent publications build on these findings and provide substantial discussion into the effects of particle size

distribution, solids concentration, pH, and subsequently, the electrokinetics of particulate suspensions [52,53,57,58,66,67]. These authors have established the mathematical framework to successfully predict trends in the yield behavior of metal oxide suspensions, using the inter-particle spacing between flocculated particles as a fitting parameter.

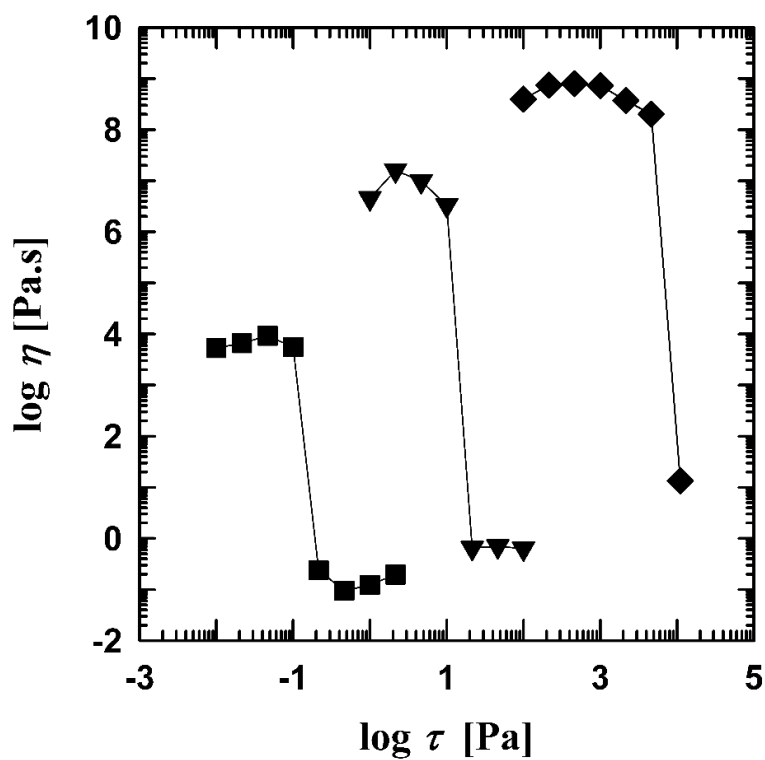


**Figure 2.2.** Yielding behavior for graphite suspension in log-log plot of viscosity against shear stress; ■: 30wt%, ▼: 40wt% ◆: 50wt% of graphite particle.

### **2.2.2. Microstructure of particulate system**

The polymer has been used to prevent sedimentation and aggregation of the particles in the suspension. In addition, the polymers cause the change of rheological properties in many kinds of suspension or slurry. At a molecular level, there are two mechanisms of flocculation formation, bridging and depletion.

The particles are stabilized by electrostatic charges on the surface of the particles, and it can be described by DLVO (Derjaguin-Landau-Verwey-Overbeek) theory [68]. The charged particles are not stabilized by direct repulsion between each particles, but by the counter-ions surrounding the surface of particles from the atmosphere. So, the interaction between the clouds of counter-ions causes the electrostatic repulsion, and the particles with same charges are well dispersed as a result.

When low concentration of polymer is added to the suspension, bridging flocculation can appear. Generally, the bridging flocculation occurs when the molecular weight of the polymer is high. The polymers adsorb on two or more particle surface, and physically holds the particles together. The polymer adsorption on the particle surface is affected by various factors including not only physicochemical conditions such as molecular weight, ionic strength and pH [41-43,69], but also process conditions such as mixing time and temperature [41-43,70,71]. Especially, Ahn's group investigated microstructural change depending on the adsorption amount of polymer in Silica/PVA system [41-43]. The adsorption amount of PVA on the surface of silica depended on the mixing time, and pH, and induced bridging flocculation. In addition, they observed that the microstructure of the suspension affected the microstructure of dried film because

of microstructural change during drying by interaction between adsorbed and non-adsorbed polymer in the suspension.

As the concentration of polymer is increased, the adsorption amount of polymer is also increased. The configuration of adsorbed polymer is brush-like, and the adsorbed layer can extend over large distance to reduce the effect of van der Waals attraction between the particles. Then, the flocculation by bridging polymer becomes dispersed by the adsorbed polymer, and it is known as a steric stabilization [72].

As the concentration of polymer is further increased, there exists non-adsorbed polymer as well as adsorbed polymer in the suspension. The adsorption amount of polymer increases as the concentration of polymer is increased, then the surface of particle is saturated by the adsorbed polymer. As the particles move closer to each other, the polymer located among the particles becomes excluded to the outside of the inter-particle space. The resulting difference in the concentration between in the bulk medium and in the overlap region among the particles promotes higher osmotic pressure in the bulk medium than in the overlap region, and induces flocculation of the particles. It is termed as a depletion flocculation [73-75].

Likewise, both the adsorbed and non-adsorbed polymer have significant effect on the microstructure formation in the particulate system including the control of particle flocculation and rheological properties.



### 2.2.3. Microstructure of Li-ion battery

As the Li-ion battery has been used in various industries, new technologies for the weight reduction, miniaturizing, high performance, safety, etc., are demanded recently. There are many factors that influence the electrochemical performance of the battery such as new active material [1-5] and improvement of manufacturing process [24,25]. To control of the microstructure for the slurry as well as the film is one of methods for enhancing the performance of the battery [30,76,77]. Novák's group investigated the effect of the microstructure of electrode on the electrochemical performance of the battery [76,77]. They showed that a surfactant affects the dispersion of  $\text{TiO}_2$  as well as carbon black particles, and the homogeneous particle distribution induces the enhanced electrochemical performance of the electrodes. Nguyen et al. [30] showed that the polymer had an effect both on the particle dispersion in the silicon based anode slurry and battery performance in the electrode. Poly (acrylic-co-maleic) acid (PAMA) which was used as a dispersant affected the dispersion of carbon black in the slurry as well as in the film. It also played a role to enhance the battery performance such as cyclability and coulombic efficiency. Wang's group studied the effect of binders on the particle dispersion of the battery slurry [22,27,78]. They studied that the effect of binders, such as CMC and SBR, on the dispersion and the physical and electrochemical performance of  $\text{LiCoO}_2$  electrodes [22]. As a results, the CMC played a prominent role to disperse the  $\text{LiCoO}_2$  particles when the concentration of SBR was decreased. However, when the concentration of SBR was decreased, the binder distribution in the dried film became less uniform, inducing decrease in the adhesion strength and increase in the surface resistance of the electrodes. Therefore, the blending ratio of CMC and SBR had

to be optimized for enhancing battery performances. In addition, they studied interactions between organic binders, such as CMC or SBR, and active powders, such as  $\text{LiFePO}_4$  or graphite or carbon black, in lithium iron phosphate slurry [78]. The interaction of binders with particles is influenced by a mixing protocol, and it affects the dispersion of slurry as well as the electrochemical properties of electrodes. As a result, a better dispersed slurry exhibits better electrochemical performances. Lee et al [24] also showed that the microstructure of the slurry depending on the mixing protocols, and well-dispersed slurry caused uniform distribution of particles in dried film, inducing good electrochemical performance of the battery.

In addition, there are studies that binder distribution in the film affects the battery performance. Li and Wang [37] investigated the effect of binder distribution in water-based and organic-based  $\text{LiCoO}_2$  electrodes on the electrochemical performances of the battery. The ingredients such as graphite, carbon black, and binders were non-uniformly distributed in dried film in the  $\text{LiCoO}_2$  slurry with an organic-based solvent due to their low viscosity and high fluidity. The non-uniform distribution of binders and particles caused poor adhesion strength, resistance and charge-discharge efficiency compared to the water-based electrode where the ingredients were distributed homogeneously in the film

Likewise, the microstructure of the slurry as well as the film have a profound effect on the physical and electrochemical performance of the battery. So, it is crucial to understand the mechanism of microstructure formation in the slurry and the film for enhancing the battery performances.

## **2.3. Drying process of particulate system**

### **2.3.1. Drying mechanism**

Drying is a solidification process in which coating solution solidifies as solvents are eliminated from the solution. If operating conditions of drying such as temperature, humidity, air flow, etc., are not optimized, an inhomogeneous internal gradient of ingredients or a phase separation occurs during drying and a drying stress is generated, inducing film defects such as curl, crack, and delamination. Therefore, in manufacturing industry, it is crucial to understand the drying mechanism and control the drying process for optimal product.

The process of solidification can be divided into six stages, 1) solvent removal, 2) solvent movement within coating, 3) energy delivery, 4) transformation to elastic solid, 5) drying stress development, and 6) coalescence. Let us figure out the characteristics of each stage in solidification process.

#### ***Elemental solidification process***

The solvents evaporate from the solvent-air interface in coatings to a surrounding gaseous environment. If the surrounding gas is stagnant, the diffusion of evaporated solvent will be a slow process. Therefore, the solvent evaporation from the coatings is accelerated through a forced convection of the air.

The rate of solvent evaporation is adjusted by two factors. One is a partial pressure difference between the surface of coatings and the surrounding gas. The partial pressure

difference is a major driving force of solvent evaporation. The driving force can be adjusted through the change in partial pressure of the solvent or the drying temperature. Generally, the partial pressure of the surrounding gas is balanced with the solvent concentration near the coating surface. If the partial pressure of the surrounding is larger than that of solvent at coating surface, the driving force is diverted from the solvent evaporation to condensation and the solvent condenses to form water drop, inducing 'blush' as the defect.

Another is a mass transfer coefficient which is a representative of convection and diffusion near the coating surfaces. It is controlled by a flow direction and the velocity of the forced convection of the gas. The mass transfer coefficient becomes the largest value when the gas flows in vertical direction to the coating surfaces. Then, the diffusion of the evaporated solvents is enhanced by the convection.

### ***Solvent movement within coating***

The solvent within the coating moves through a pressure gradient driven flow in porous coating, convection, and diffusion along with the diffusion induced convection. The solvent flows by the capillary pressure at the liquid/gas meniscus if the coating becomes porous. For instance, the solvent flows from the small curvature of meniscus in the large pores to the large one in the small pores. In addition, if the curvatures of the meniscus are the same but are at different temperatures, the solvent flows from a higher temperature to a lower one. The voids become smaller through the precipitation or flocculation of the particles, and they enhance the pressure gradient driven flow.

The solvent in the coating moves by the difference of a chemical potential for the ingredients. For example, the solvent moves from the high concentration regime to the low concentration regime. This flow behavior is always applied in a binary system but it is not always applied in a multi-component system. In the binary system, only one component flows independently by the concentration gradient, the local flow of another one occurs in proportion to the local concentration gradient. The proportional constant is the binary diffusion coefficient or diffusivity.

### ***Energy delivery***

The convection and the conduction from the surrounding gas induce an energy delivery for drying or solidification of the coating. Raising the temperature increases the driving force for the solvent removal by the partial pressure difference. In addition, it increases a solvent diffusivity and decreases the internal and diffusional resistance to mass transfer. Therefore, as the drying temperature increases, the rate of drying increases. However, if the drying temperature is too high, some defects, such as bubble at the coating surface, can occur. So, it is crucial to set up an appropriate temperature which induces the fast drying but does not induce the defects.

The rate of heat delivery to the coating per unit area of the surfaces by the convection and the conduction from the gas depends on the driving force and the heat transfer coefficient. The driving force is defined as the temperature difference between the surrounding gas and the coating surface, and the heat transfer coefficient is defined as the heat conductivity.

When the solidification of the coating occurs by curing, not the solvent evaporation, the reactions, such as polymerization by thermal or radiation, or crosslinking also require the energy delivery such as heat, ultraviolet, and electron beam.

### ***Transformations to elastic solids***

The coating, such as polymer solution or suspension, is spread on the web and transformed to the elastic solids by the evaporation of the solvents. The solidification is conducted by a nucleation, growth, and aggregation of the ingredients. In the case of polymer solution, the molecules are vitrified, producing a partially crystalline material which contains a crystallite in amorphous matrix. The polymer solution becomes thermodynamically unstable as the concentration of the polymer increases, and it may be separated into two phases of the solution. In addition, if the drying rate is too fast, inhomogeneous concentration gradient of the solvents can induce the 'skinning' [79]. Likewise, the microstructure and morphology of the film can be adjusted by the phase separation rate of the polymer and the diffusion rate of the solvent [80]. When the diffusion rate of the solvent is faster than the phase separation rate of the polymer, the morphology of the film becomes homogeneous. On the contrary, if the phase separation rate is faster than the diffusion rate, the polymer molecules have plenty of time to separate with each other, and the film becomes inhomogeneous.

In the case of the suspension, the particles are dispersed in the medium at initial drying stage, and the solvents are evaporated from the air/liquid interface. When the convection by evaporation is fast, the particles are gathered and packed at the coating surface. The particle packing layer is called a consolidation zone. The particles in the

medium are further packed in the consolidation front which is beneath the consolidation zone as the solvents are evaporated. In the consolidation zone, the repulsive force in the electric double layer of the particles becomes stronger than the attractive force. So, the particles which move toward the consolidation front tend to diffuse back to the bulk phase.

As the particles are packed, the consolidation layer becomes thicker and the menisci among the particles increases and the capillary pressure gradient increases. The menisci curve at the first layer in the consolidation zone increases until maximum curvature as drying proceeds, and pore-spaces are formed. As the unstable menisci invade into the second layer in the consolidation zone, the pore-spaces in the first layer are filled by the air. Even though the pore-spaces in the first layer are filled by the air, the outer of the pore-space (pendular ring) is surrounded by residue solvents. The capillary force is generated as the curve of menisci in the pendular ring becomes sharp, and the particles are packed more densely.

### ***Drying stress development***

As the solvent is evaporated from the polymer solution or the suspension, the polymers are vitrified or the particles are aggregated. Then the coating shrinks and the stress is generated. The drying stress can induce the film defects such as curling, cracking, peeling, or delamination. Therefore, it is important to understand the origin of the drying stress to generate the optimal film. The drying stress will be introduced in detail at section 2.2.2

## *Coalescence*

As the particles are packed together and the boundary of the particles disappear, the film is generated. When the drying temperature is lower than the glass transition temperature of the latex or hard sphere, the film is not formed due to large modulus of the particles. If the drying temperature increases or a plasticizer is added to the coating, the modulus of the particles decreases. Then, the mobility of the polymer chains increases and the rate of inter-diffusion becomes faster, so the smooth film can be generated.



## 2.3.2. Drying stress of particulate system

### 2.3.2.1. Origin of drying stress

A coating which is liquid state is converted into a film which has elastic or viscoelastic property through a drying process. The coating solution is coated onto the web. So, the film is formed in a non-equilibrium configuration due to a constrained shrinkage, inducing drying stress. The coating, the liquid state, is in a stress-free state itself. As solvent is evaporated from the coating, the volume of the coating shrinks because of a reaction of polymer, phase separation, or aggregation of particles. The coating shrinks during drying and tends to be a stress-free state by molecular relaxation and deformation of the polymer. Ideally, the final state of the dried film reached to the stress-free state if the rate of solvent evaporation is same with that of stress relaxation. However, in a real process, the coating is in direct contact with the web and the shrink of the coating is constrained due to the adhesion between the coating and the web. Figure 2.3 shows schematic about difference between ideal stress-free state and actual drying state. So, the volume of the film in the actual state is different with the ideal stress-free state, and the difference value is defined as a strain. The strain is proportional to the stress as Hooke's law,  $\tau = G \times \gamma$ , where  $\tau$  is stress,  $G$  is modulus, and  $\gamma$  is strain. In addition, the strain can be obtained by calculating the quantity of the solvent at a solidification point and that of in dried film. The glass transition temperature of the coating is increased during drying. Then the point where the glass transition temperature of the coating and the drying temperature are same is defined as the solidification point,

and the coating is changed from the liquid state to the solid state through the solidification point.

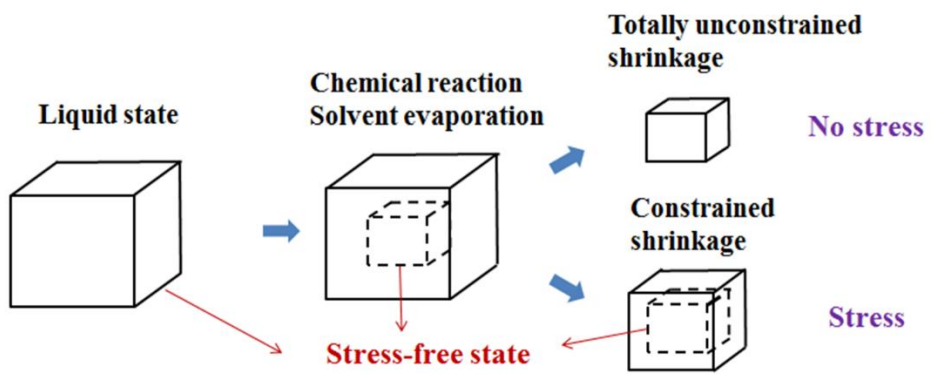


**Figure 2.3.** Schematic about difference between ideal stress-free state and actual drying state [81].

### **2.3.2.2. Stress development during drying process**

Stress is developed due to the shrinkage of coating liquid while it dries. The drying stress can induce film defects such as crack, curl, and delamination. In order to manufacture the film with good mechanical performance, it is important to understand the mechanism of stress development during drying. When the coatings are coated onto a substrate, in-plane tensile stress is developed due to the constrained shrinkage [38]. The cantilever deflection method can measure the in-plane stress during drying, and has been used to characterize the drying mechanism for polymer solutions [38-40] and suspensions [41-50]. Details of setup of the cantilever deflection will be introduced at section 3.3.

The drying process can be divided into three stages such as initial, constant rate, and falling rate period, according to a degree of solvent evaporation (Figure 2.4).

#### ***Initial period***

The coating is spread onto the web, and the temperature of the coating is reached to equilibrium state with drying temperature. This stage is called an initial period and the period is very short compared to other periods.

#### ***Constant rate period (CRP)***

After the temperature of the coating is in equilibrium with the drying temperature, the rate of solvent loss becomes a constant. This stage is called a constant rate period. One of the factors, which determine the rate of solvent removal to the coating per unit

area of the surface, is the partial pressure difference between the coating surface and the surrounding air, and the partial pressure difference is the driving force for the solvent evaporation. The driving force can be adjusted by changing the partial pressure of the surrounding air, or the coating surface by changing temperature. The partial pressure at the coating surface will be constant when the composition and temperature are constant, and the driving force for the solvent evaporation becomes constant if the partial pressure at the surrounding gas will be also constant. In addition, when the driving force of the solvent evaporation, the rate of weight loss for the solvent is constant.

In constant rate period, the solvent moves toward the coating surface by the capillary pressure, and it is evaporated from the air/liquid interface. Therefore, the coating surface is saturated by the solvents. The drying is controlled by external conditions such as the temperature and relative humidity of the surrounding air.

The coating is not solidify yet in the constant rate period, so the modulus of the coating is low and the stress relaxation is relatively fast. Therefore, the drying stress cannot be developed dramatically in the period. Figure 2.4 shows the development of the drying stress for the anode slurry containing 50wt% of graphite and 0.7wt% of CMC, and the drying temperature is 70 °C. Until approximately 5 min, the rate of the solvent loss is constant and the drying stress is smoothly developed compared to next period, falling rate period.

### ***Falling rate period (FRP)***

In the constant rate period, the rate of solvent evaporation is constant because the internal resistance to vapor diffusion is smaller than the external resistance. However,

the internal resistance to vapor diffusion is decreased as the partial pressure of the solvent in the coating is decreased during drying. And then, the rate of the solvent loss will be decreased. This stage is called a falling rate period.

In the falling rate period, the solvent which is saturated at the coating surface in the constant rate period invades into a porous body which is formed by concentrated solute. Then, the drying proceeds by solvent diffusion in the internal coating.

The coating is solidified in the period, then the modulus of the coating increases and the drying stress is developed dramatically. Although the rate of the solvent loss is decreased, the stress of the coating is accumulated continuously. This is because that, in spite of the small deformation due to less solvents which residue in the coating, the coating has large stress by the small deformation because the solidified coating has large modulus. As shown in Figure 2.4, it can be confirmed that the rate of solvent loss is decreased from the falling rate period, and the drying stress is developed dramatically followed by it is reached equilibrium state.

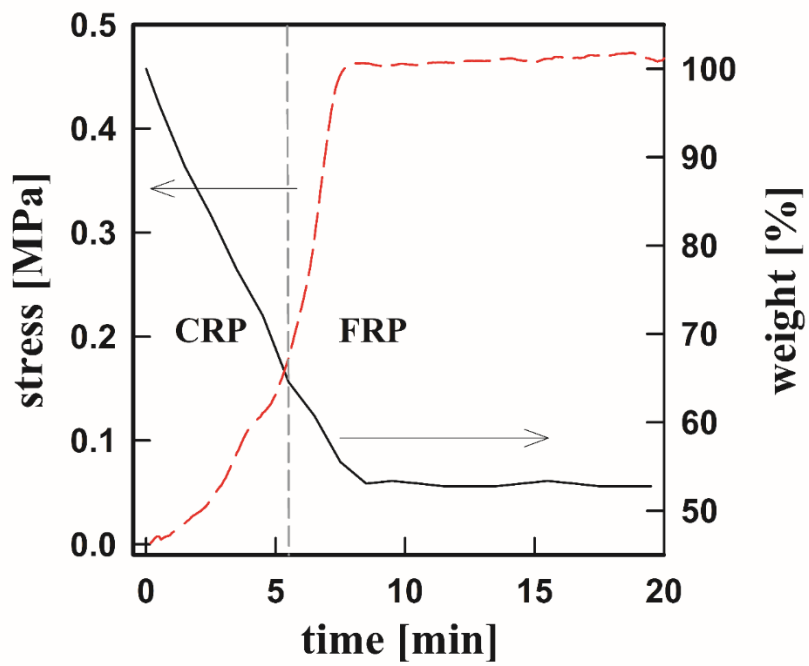


**Figure 2.4.** Drying stress development and weight loss of anode slurry during drying.

### **2.3.2.3. Effect of drying temperature on drying stress**

Figure 2.5 shows the drying stress development for the anode slurry containing 50wt% of graphite and 0.7wt% of CMC depending on the drying temperature. As the drying temperature is increased, the rate of drying increases and the stress is developed earlier. However, the final stress decreases as the drying temperature is increased. This is because the quantity of the solvent at the solidification point is different according to the drying temperature. That is, the solvent is evaporated faster at high drying temperature, so the quantity of the solvent when high drying temperature is less than at low drying temperature at solidification point where the coating starts to show solid-like behavior. Then, the elastic modulus of the coating decreases and the stress relaxation increases, the drying stress decreases as the drying temperature is increased. The effect of the drying temperature is predominant at 0% of relative humidity. As the relative humidity is increased, the degree of the drying stress decrease with drying temperature is reduced.

### **2.3.2.4. Effect of relative humidity on drying stress**

Figure 2.6 indicates the development of the drying stress depending on the relative humidity. When the relative humidity is changed and the drying temperature is constant, the origin of drying stress change is different compared with the dependence of the drying stress on the drying temperature. As shown in Figure 2.6, the final stress as well as the drying rate decreases as the relative humidity is increased. As the relative humidity is increased, the driving force which is by partial pressure difference between



the coating surface and the surrounding decreases. In addition, the coating surface is moisturized at high relative humidity, inducing less shrinkage of the coating and small modulus as well as drying stress.

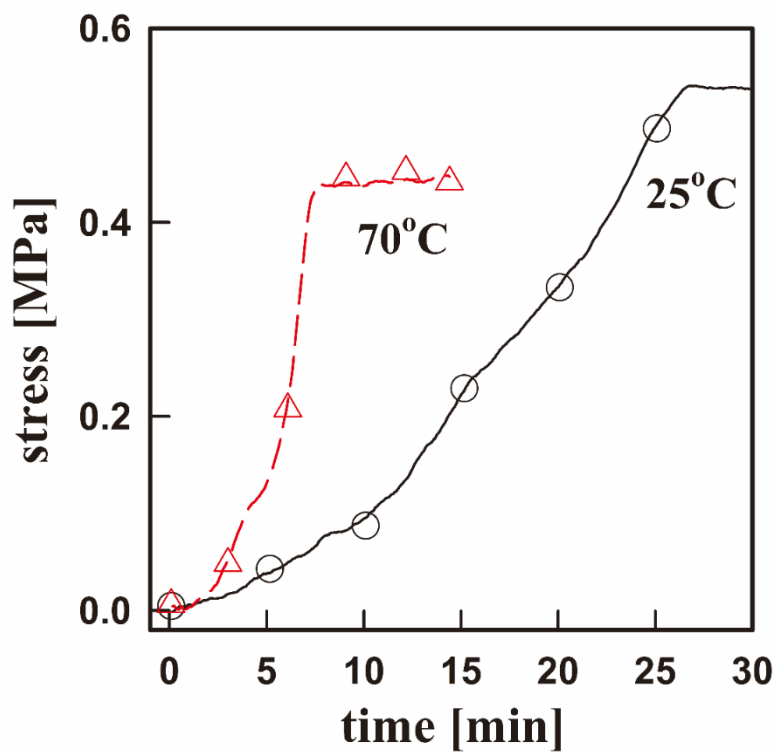


**Figure 2.5.** The development of the drying stress for the anode slurry containing 50wt% of graphite and 0.7wt% of CMC at different drying temperature, 25 and 70 °C. The relative humidity is 40%.

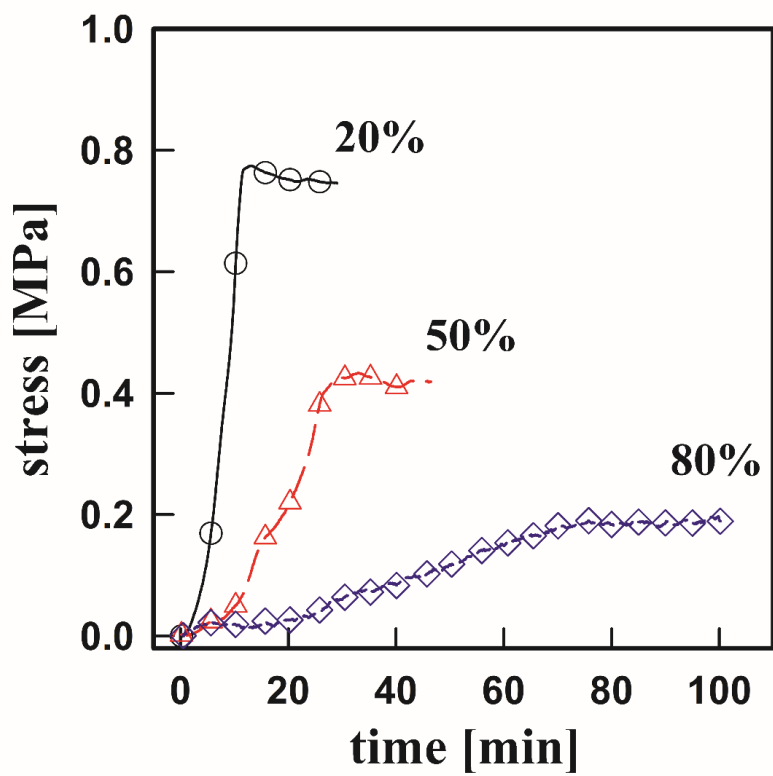


**Figure 2.6.** The development of the drying stress for the anode slurry containing 50wt% of graphite and 0.9wt% of CMC at different relative humidity from 20 to 80%. The drying temperature is 25 °C.

## **2.4. Particle migration during drying**

The particles as well as the polymer in a particulate system are migrated during drying by diffusion or convection. The particle migration during drying induces the non-uniform particle distribution in the dried film. Therefore, the particle migration during drying has an effect on the microstructure as well as the physical property of the film, therefore it is important to understand and to control the mechanism of the particle migration for optimized film. This chapter consists of two parts, lateral migration and vertical migration during drying.

### **2.4.1. Particle migration in a vertical direction of film**

Some possible underlying physics for particle migration, such as capillary flow-induced [34,82] and Brownian motion-induced [21] migrations, have previously been suggested. Luo et al. [34] explained that when small clusters of particles packed together by Brownian motion or lateral capillary attraction [83], a difference in pressure is generated over the curved menisci between the particles, which contacts with air at the top of the film. The resulting capillary-pressure-driven flow induces the migration of particles, and a “top-down” consolidation front [82] separates the particle consolidation layer and dispersed particles in the medium beneath the layer. On the contrary, Zang et al. [21] suggested that latex particles migrate toward the surface of coatings because of the significant amount of Brownian motion among small particles. The small particles are trapped because of interfacial tension associated with a receding air-water interface, leading to a heterogeneous concentration distribution and a high

concentration of particles at the surface of the film. Besides that, the differences in the particle diffusivity can also influence the distribution of particles during drying [84,85]. Although some hypotheses have previously been proposed for the mechanism of particle migration, the rigorous mechanism is still a subject of ongoing debate.

There have been numerous efforts to understand the mechanism of particle migration, and a variety of measurements have been made. Typical examples include electron spectroscopy for chemical analysis (ESCA) [21,86], ultraviolet analysis [87,88], cryogenic scanning electron microscopy (Cryo-SEM) [33,34,82,89] and numerical modeling [33,89,90]. Yamazaki et al. [86] used ESCA to determine the chemical compositions of the surfaces of dried starch/latex composite films and explained that the starch preferentially migrated and affected the print mottle more than the latex did. However, ESCA measurements are limited to the surfaces of dried films. Cryo-SEM, on the other hand, is a powerful tool used to visualize the particle distribution in a cross-section of drying film. This technique involves freezing the specimen in a liquid cryogen to arrest structural changes in the film after it has been dried for a specific amount of time, fracturing the specimen to reveal the coating cross-section, and sputter-coating the fractured specimen to prevent charging before imaging. Cardinal et al. [89] and Buss et al. [33] demonstrated a transient particle distribution in coatings depending on the drying conditions of the films and showed consistency between Cryo-SEM observations and predictions made using a 1D model. The distribution of the particle in the film is determined by dimensionless Peclet number,  $Pe$ , which is defined as the ratio of evaporation and diffusion of the particle [90]. That is, the diffusion of the particle is dominant when  $Pe < 1$ , so the particles are distributed uniformly in the dried film. On

the other hand, when  $Pe > 1$ , the evaporation of the particle is dominant and the non-uniform particle distribution is formed because the particles accumulated at the coating surface. However, the sampling rate of the images was relatively limited because of the careful preparation of the samples [91].

At section 4.3 in the thesis, we used fluorescence microscopy (FM) to develop a method for measuring latex particle migration in drying films. Fluorescent latex particles in liquids emit fluorescent light when an excitation laser beam is irradiated through the whole coating. The intensity of the fluorescent light is detected using a microscope, and it provides information on the vertical particle distribution of the coating because the intensity of the fluorescent light increases as the particle consolidation layer develops in the vicinity of the free surface. FM can be used for measurements at high sampling rates and can even be applied to opaque and/or thick coatings without any particular preparation necessary for the samples; hence, FM has a great advantage over other measurement techniques.

### **2.4.2. Particle migration in a lateral direction of film**

The solute, particles or polymers, can migrate in lateral direction as well as vertical direction in the film during drying. Deegan et al. [92,93] reported the lateral migration of the particles during drying in a droplet. The solvents is evaporated faster at the edge than at the center in the droplet. When the edge of the droplet is pinned at the substrate, the solvents flows from the center to the edge in order to supply the solvent to the edge. Then, the capillary flow brings the suspended particles to the edge, and the particles are accumulated and formed a ring-like pattern. This is called a “coffee stain phenomenon”.

There are many researched about the suppression of the coffee stain phenomenon. A Marangoni flow induced uniform distribution of the particle is the one of the method for the suppression of the coffee stain phenomenon. The non-uniform evaporation at the surface of the droplet induces temperature gradient and surface tension gradient, inducing the Marangoni flow. The recirculatory flow in a droplet can suppress the accumulation of the particle at the edge in the droplet [94,95]. In addition, the direction of the Marangoni flow can be adjusted by control the relative thermal conductivities of the substrate and liquid and the contact angle [96]. Yunker et al. [97] reported that the ellipsoid particles can suppress the coffee stain structure. The ellipsoid particles form a loosely packed structure by strong long-ranged attraction with surrounding particles. Then, the outward flow is suppressed by the open structure and the mobility of the particles decreases, inducing the uniform particle distribution in the film. On the other hand, the spherical particles migrate to the edge in the droplet by outward flow, but the particles are accumulated and packed at the edge because it cannot form specific structure which can suppress the outward flow. Weon and Je [98] investigated that the suppression of the coffee stain phenomenon by capillary force. When the inward force which is by net capillary force between the liquid surface and the particles is stronger than outward flow, the particles move back to the center in the droplet. The capillary flow of the particles occurs when the contact line of the droplet has to be pinned and the particles have to be not protruded by wetting property of the particle at the edge.

I recognize that the particles are distributed in dried film depending on various conditions such as kind of particle, drying temperature, and so on. In order to obtain the

uniform distribution of the particle, I have to understand the mechanism of particle distribution formation during drying.





## **Chapter 3.**

# **Experimental methods**

### **3.1. Sample preparation**

#### **For Chapter 4.1, 4.2**

##### **Raw materials**

Graphite (SG-BH8, Ito Graphite Co., Ltd.) was used as an active material. The diameter, density, and specific surface area of graphite were 8.11  $\mu\text{m}$ , 2.23  $\text{g}/\text{cm}^3$ , and 12.12  $\text{m}^2/\text{g}$ , respectively (provided by manufacturer). Sodium carboxymethyl cellulose (CMC) and styrene butadiene rubber (SBR) were provided by SK innovation. The average molecular weight ( $M_w$ ) and the degree of substitution of CMC were 330,000  $\text{g}/\text{mol}$  and 0.7, respectively. SBR suspension contained a mass fraction of 40wt%, and the size and glass transition temperature were 140 nm and 11  $^{\circ}\text{C}$ , respectively.

##### **Preparation method**

The CMC powder was dissolved in deionized water using a magnetic stirrer for 12h. The graphite was added to the CMC solution and was dispersed using a homogenizer (Ultra-Turrax<sup>®</sup> T18 basic, IKA<sup>®</sup> Works, Inc.), followed by mixing with a magnetic stirrer for 12h. Then 40wt% SBR suspension was added to the graphite slurry and was mixed using a planetary centrifugal mixer (ARM-310, Thinky Corporation) at 2000 rpm for 5min, and the slurry was finally mixed on a magnetic stirrer for 12h.

## **For Chapter 4.3**

### **Raw materials**

Graphite (SG-BH8, Ito Graphite Co., Ltd., Japan) was used as an active material. The diameter, density, and specific surface area of the graphite particles were 8.1  $\mu\text{m}$ , 2.23  $\text{g}/\text{cm}^3$ , and 12.12  $\text{m}^2/\text{g}$ , respectively (provided by manufacturer). Sodium carboxymethyl cellulose (CMC; BSH-6, Dai-ichi Kogyo Seiyaku Co., Ltd., Japan) was used as a thickening agent to prevent sedimentation of the graphite particles [29]. The average molecular weight ( $M_w$ ) and the degree of substitution of CMC were 290,000–340,000  $\text{g}/\text{mol}$  and 0.65–0.75, respectively (provided by manufacturer). Fluorescent polystyrene (PS) particles (micromer® -redF, micromod Partikeltechnologie GmbH, Germany; diameter = 100 nm; density = 1.03  $\text{g}/\text{cm}^3$ ; zeta potential in water =  $-40 \pm 5$  mV) were used in this study. The maximum excitation and emission wavelengths of the fluorescent PS particles were 552 and 580 nm, respectively. The fluorescent PS particles were dispersed in water.

### **Preparation method**

The CMC was dissolved in deionized water and was stirred using a magnetic stirrer for 12 h. The latex suspension was added to the CMC solution and the resulting mixture was mixed for another 12 h. The graphite was added to the latex-CMC suspension and was dispersed using a homogenizer (HG-200, Hsiangtai Machinery Ind. Co., Ltd., Taiwan) with an impeller (K-12S, Hsiangtai Machinery Ind. Co., Ltd., Taiwan) at

10,000 rpm for 3 min. The graphite slurry was mixed for another 12 h. All the samples were prepared just before the experiments. The graphite slurry was prepared for sedimentation and adsorption isotherm measurements in the same manner except that fluorescent latex particles were added to it. The CMC concentrations were chosen to be above 0.4 wt% in order to prevent both lateral heterogeneous particle distribution and sedimentation of graphite particles.

## **3.2. Characterization of microstructure of battery slurry**

### **3.2.1. Measurement of rheological property**

Rheological properties of battery slurry was measured using two types of rheometer. A strain-controlled rheometer (ARES, TA Instruments) was used for a rate sweep test and dynamic tests. The geometries of parallel plates of 25 mm and 40 mm in diameter for battery slurry and cone plates of 25 mm and 50 mm in diameter with 0.0396 rad and 0.0398 rad, respectively, for CMC solution were used. In addition, a stress sweep test was conducted using a stress-controlled rheometer (AR-G2, TA Instruments) with 40 mm in diameter. The measurements were performed at 25 °C. The battery slurry was allowed to take a rest time for 120 s without pre-shear before conducting rheological measurements, in order to remove shear history which could be invoked when the battery slurry was loaded in the rheometer.

### **3.2.2. Measurement of adsorption amount of CMC**

Isotherms for the amount of CMC adsorbed onto graphite were measured as functions of CMC concentration. Graphite slurries containing 5 wt% graphite and various concentrations of CMC were prepared, and the supernatant was extracted after the slurries were centrifuged at 50,000 rpm until graphite particles had completely separated from the supernatant. The amount of CMC adsorbed onto the graphite was calculated by determining the concentration of non-adsorbing CMC in the supernatant.

### **3.2.3. Cryo-SEM**

The scanning electron micrographs for the anode slurry were obtained using the FE-SEM (Mira3 LMU FEG, Tescan) with sample preparation system for cryo-SEM (PP3000T, Quorum Technologies). Figure 3.1 shows the schematic of specimen preparation for cryo-SEM. The slurries were loaded in the holes of cryo-stubs. At that time, the slurries should be filled as well as be protruded. Then, the slurries were fast frozen by plunging them into liquid nitrogen. The frozen slurries were transferred to the cryo-preparation system, and they were fractured cross-sectionally. The fractured samples were sublimated at -100 °C for 10 min, and then it was coated with platinum at -140 °C for 120 s. All images were captured at -140 °C.

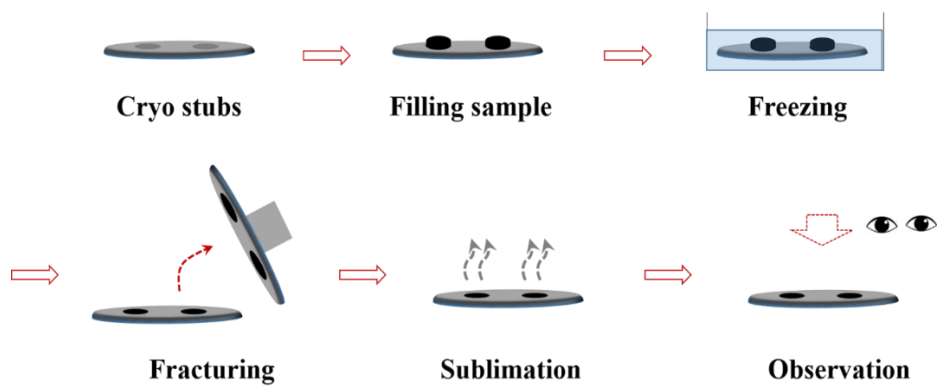


**Figure 3.1.** Schematic of specimen preparation for cryo-SEM.



### 3.3. Measurement of drying stress development

The drying stress was measured using a cantilever deflection method. The equipment is composed of a cantilever, laser, position sensing detector, and data acquisition system (Figure 3.2). The slurry was coated on the cantilever, then the cantilever was deflected during drying because the in-plane tensile stress appeared in the coating. Then, the degree of deflection of the cantilever is detected by the laser and the position sensing detector. A cover glass of 60mm × 6mm with approximately 150 μm of thickness was used as the cantilever. The cover glass was coated with 20nm-thick titanium and 100nm-thick gold by sputtering to enhance laser deflection. A laser (LM-6505MD, Lanics Co., Ltd.; wavelength = 655±5 nm) whose beam intensity obeyed a single Gaussian distribution was used as a light source. The laser beam was irradiated to the bottom of the cantilever, and the degree of cantilever deflection which occurred due to the shrinkage of coatings could be obtained through the position shift of the beam detected by the position sensing detector (PDP 90A, Thorlabs, Inc.). The detected laser beam was translated into the electric signal, and was transferred to the data acquisition system.

The anode slurry was coated on the cover glass by using the doctor blade (Ref. 1117/200, Sheen Instruments). The thickness of the film after drying was about 100 ± 5 μm. The anode slurry was dried in a closed chamber, and the circumstance in the chamber was maintained at 25 ± 1°C and 20% of relative humidity. The degree of cantilever deflection was transformed to the drying stress using the Cocoran equation (Eq. 1):

$$\sigma = \frac{dE_s t_s^3}{3t_c l^2 (t_s + t_c)(1-\nu_s)} + \frac{dE_c (t_s + t_c)}{l^2 (1-\nu_c)} \quad (3.1)$$

where  $d$ ,  $E$ ,  $t$ ,  $l$ , and  $\nu$  are the deflection, elastic modulus, thickness, substrate length, and Poisson ratio, respectively. Subscripts  $s$  and  $c$  represent the substrate and film after drying, respectively. If the modulus of the substrate,  $E_s$ , is much larger than that of the film,  $E_c$ , as in our case, the second term in equation (1) can be ignored [99]. Therefore, the drying stress can be obtained using only the first term in equation (1). Some assumption which was suggested by Corcoran [99] was adopted for measuring drying stress. For example, the cantilever is deflected spherically within the limitation of elastic region of the coating and substrate. In addition, the coating was assumed to show isotropic mechanical properties and good adhesion with the cantilever.

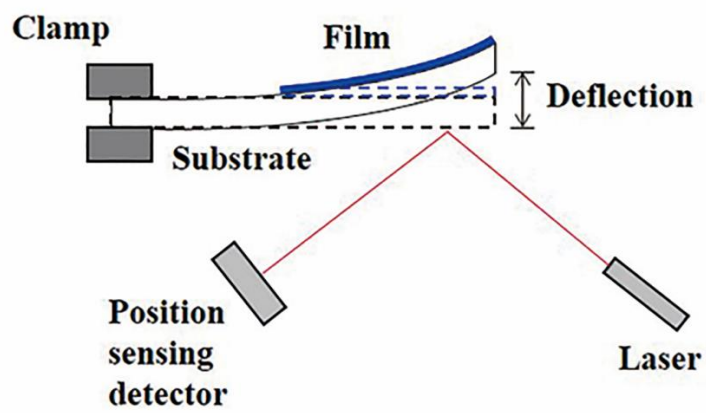


**Figure 3.2.** Schematic of cantilever deflection measurement.

### 3.4. Fluorescence microscopy during drying

A schematic of the drying apparatus is shown in Figure 3.3(a). The intensity of the fluorescent light, the size of the scattered beam, and the solvent mass loss during drying were simultaneously measured. A micropipette was used to coat the specified volume of battery slurry onto the glass substrate with a stainless steel guide. The diameter and the height of the coating were 56 mm and 500  $\mu\text{m}$ , respectively. A TEM00-mode laser (Lasiris<sup>TM</sup> Green, Coherent, Inc., USA; wavelength =  $532 \pm 1$  nm) whose beam intensity obeyed a single Gaussian distribution was held in position at a  $45^\circ$  incidence to the coating. The laser intensity was adjusted using a neutral density (ND) filter to avoid a saturation of fluorescence images. Lasers whose intensities were 110  $\mu\text{W}$ , 1.17 mW, and 7.12 mW were used to irradiate the coatings for graphite-free, 1 wt%, and 5 wt% graphite slurries, respectively. A charge-coupled device (CCD) color camera system (VB-7010, Keyence Co., Ltd., Japan) with a band-pass filter ( $580 \pm 5$  nm) was used to capture the emission signals from the fluorescent PS particles. The maximum intensity of the Gaussian distribution with respect to the background value was analyzed using software (VH analyzer, Keyence Co., Ltd., Japan) and was used as the characteristic intensity of the fluorescent light used in this study (Figure 3.3b). A CCD beam profiler (Beam On, Duma Optronics, Ltd., Israel) was located on the opposite side of the laser at a  $45^\circ$  reflection, and it was used to capture the size and shape of the laser beam reflected from the coating. The image captured by the CCD beam profiler was analyzed using software (Beam On USB 2.0 measurement system, Duma Optronics, Ltd., Israel), as shown in Figure 3.3(c). The drying temperature of the film was adjusted

using a micro warm plate (MD-10DMFH, Kitazato Co., Ltd., Japan) located beneath the coating at interspaces of 250  $\mu\text{m}$  to uniformly heat the bottom of the coating. Solvent loss was simultaneously measured using an electronic balance (Cubis® MSE-3203S-0-00-DE, Sartorius Mechatronics Japan, K.K., Japan) during drying. All equipment was set up on a vibration isolator (TDI-129-100LM, Sigma Koki Co., Ltd., Japan) and was covered with a black curtain to prevent outside light from interfering with the measurements.

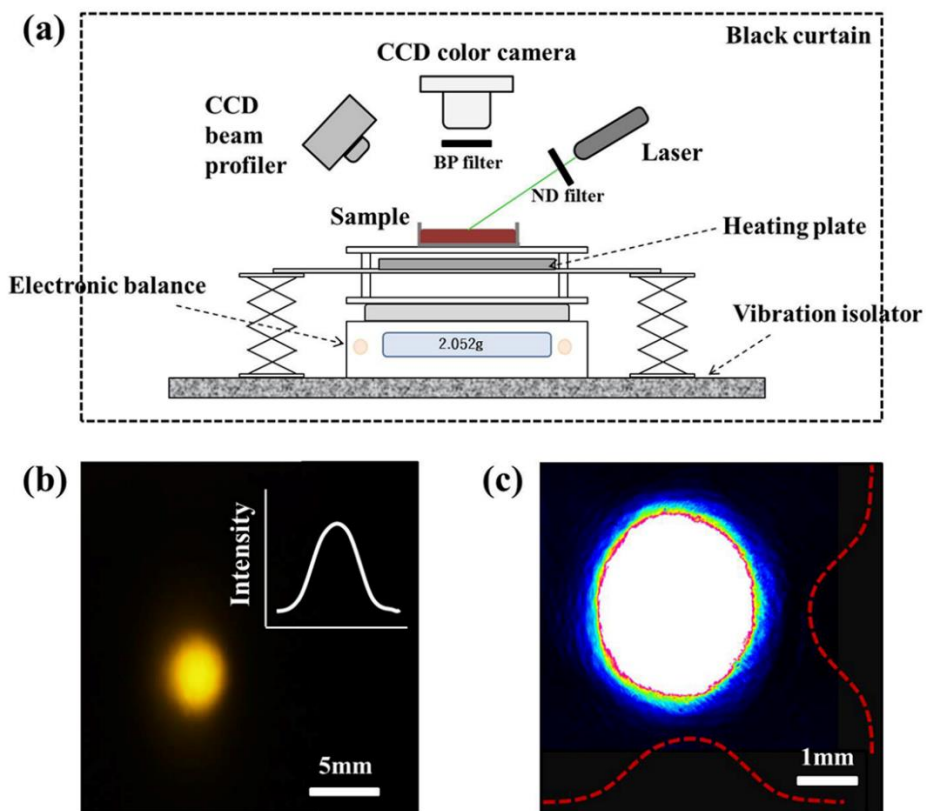


**Figure 3.3.** (a) Schematic of drying apparatus, (b) image captured by CCD camera, (c) image captured by CCD beam profiler.

## 3.5. Characterization of microstructure of film

### 3.5.1. Pore size distribution in dried film

Optical method, such as microscopy, is not suitable to analyze the microstructure of opaque film. However, the mercury intrusion porosimetry (MIP) can measure the pore size distribution in the film even in the case of opaque film, and the microstructure of the film can be analyzed indirectly. In this work, the pore size distribution in anode film was measured using the mercury intrusion porosimeter (Autopore IV 9500, Micromeritics Instruments Corporation). Mercury is intruded into the pore of the film by external pressure, and the size of pore, pore size distribution, and porosity can be measured by using the amount of mercury that was intruded. A relationship between pore diameter and pressure is defined by the Washburn equation (eq. 3.2):

$$P = \frac{-4\gamma\cos\theta}{d} \quad (3.2)$$

where  $P$ ,  $\gamma$ ,  $\theta$ , and  $d$  are the pressure, surface tension of mercury, contact angle of mercury, and diameter of the capillary, respectively. In this study, the surface tension and the contact angle of mercury were 0.485 N/m and 130 degrees, respectively. In addition, the range of external pressure was from 0.1 to 33,000 psia. The pore diameter was assumed to be the diameter of the cylinder.

### **3.5.2 Images of dried film**

Images of the surface of the dried film were captured using an optical microscope (x500; VH-Z100R, Keyence Co., Ltd., Japan) and an atomic force microscope (Nanopics 2100, SII Nano Technology, Inc., Japan) in noncontact mode.

A surface in Chapter 4.3 and a cross-section in Chapter 4.4 of the dried film was taken using field-emission scanning electron microscopy (FE-SEM, JSM-6700F and JSM-6320F, JEOL, Japan, respectively). The specimen for cross-section image was fractured after it was immersed into liquid nitrogen to cleanly cut the specimen.





## **Chapter 4.**

### **Results and discussion**

## 4.1. Microstructure of anode slurry

### 4.1.1. Graphite/SBR slurry

Figure 4.1.1 shows the viscosity and the storage and loss moduli of the anode slurries which contain 50wt% of graphite and SBR concentration ranging from 0 to 30wt%. The rheological behavior of the slurry was dependent on the concentration of SBR. In the slurry with only graphite particles without SBR, the yielding behavior was observed. The behavior could be confirmed clearly by analyzing the viscosity as a function of shear stress (inset in Figure 4.1.1a). The viscosity remained constant at low shear stress indicating the slurry showed a solid-like behavior. The viscosity dropped steeply after a critical point, which is defined as the yield stress [54]. In addition, the storage modulus,  $G'$ , was larger than the loss modulus,  $G''$ , and the moduli remained constant regardless of frequency. This behavior was often observed in a particulate system which forms the gel structure in particular. The graphite particles have a tendency to form aggregated structures in an aqueous solution due to their hydrophobicity [100]. Therefore, I figured out that the graphite particles formed the gel structure with percolated network in an anode slurry without SBR. The gel structure in the slurry was not changed even though the SBR was added to the slurry. Both viscosity and moduli were slightly decreased, indicating the gel strength was decreased as the SBR was added to the slurry. However, when the SBR concentration was increased to 15wt%, the yielding behavior disappeared and the shear thinning behavior occurred. In addition, the  $G''$  was larger than the  $G'$  and the moduli depended on the frequency, indicating the gel structure in

the slurry does not exist anymore. It means that the gel structure from the aggregation of graphite particles was changed to the liquid-like structure due to dispersion of graphite particles at the high SBR concentration.

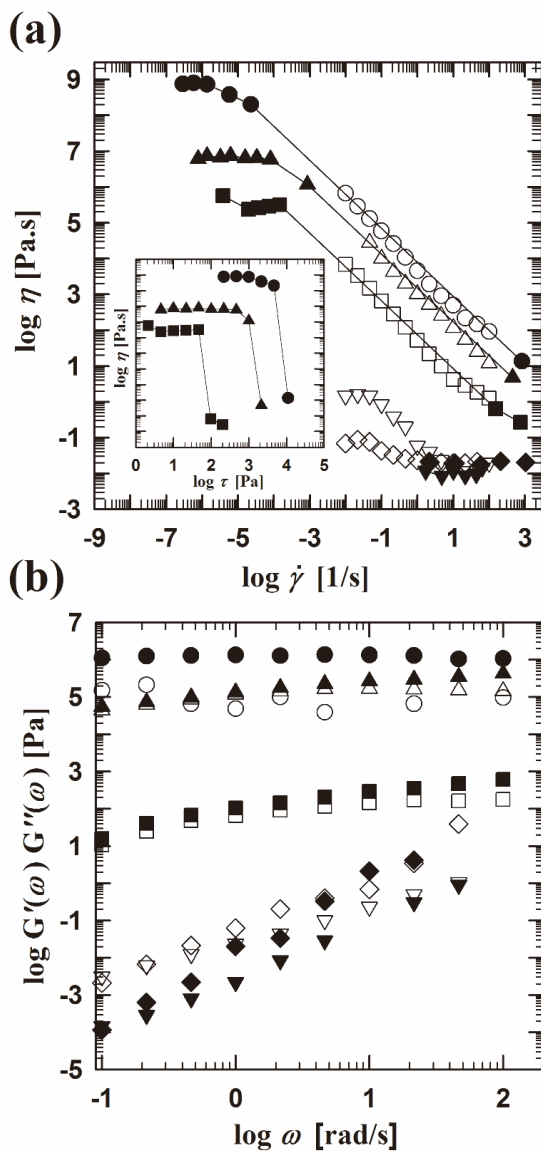


**Figure. 4.1.1.** Rheological properties of anode slurries containing 50 wt% of graphite and various concentration of SBR. (a) Viscosity as a function of shear rate and as a function of shear stress (inset in (a)); obtained from stress controlled (closed symbol) and rate controlled (open symbol) rheometer, (b) Storage (closed symbol) and loss (open symbol) moduli as a function of frequency; SBR concentration in (a) and (b): (●○) 0 wt%, (▲△) 3 wt%, (■□) 8 wt%, (▼▽) 15 wt%, (◆◇) 30 wt%.

The microstructural change of the graphite/SBR slurry could be confirmed by cryo-SEM images (Figure 4.1.2). Figure 4.1.2(a) and (b) show the microstructure of the slurry containing 50wt% of graphite and 3wt% of SBR. In the low magnified image, the network structure by the aggregated graphite particles could be verified (Figure 4.1.2a). In addition, the SBR adsorbed on the surface of graphite particles could be observed in the high magnified image (Figure 4.1.2b). There was a study about the adsorption of SBR on the graphite surface. Li and Lin [78] investigated the interaction of SBR and CMC with graphite particles by measuring the zeta potential of the slurry and the sedimentation test. They figured out that the SBR as well as CMC could be adsorbed on the graphite particles although the interaction of the binders with the graphite particles was different with each other. Figure 4.1.2(c) and (d) show the microstructure of the slurry consisting of 50wt% of graphite and 30wt% of SBR. In the image with low magnification, it could be confirmed that the graphite particles were well dispersed in the medium (Figure 4.1.2c). The SBR existed on the surface of graphite particles as well as in the medium as shown in the image with high magnification (Figure 4.1.2d). Through the rheological properties and the cryo-SEM images for the graphite/SBR slurry, I figured out that the slurry structure depended on the SBR concentration. That is, the graphite particles form the gel structure by hydrophobic attraction. The SBR was adsorbed on the graphite surface when the low concentration of SBR was added to the slurry, and the gel strength was decreased but the gel structure was still maintained in the slurry. However, as the SBR was further added to the slurry, the graphite particles were dispersed by electrostatic repulsion due

to anionically charged surfactant which existed on the SBR. As a result, the slurry showed liquid-like behavior at high SBR concentration.

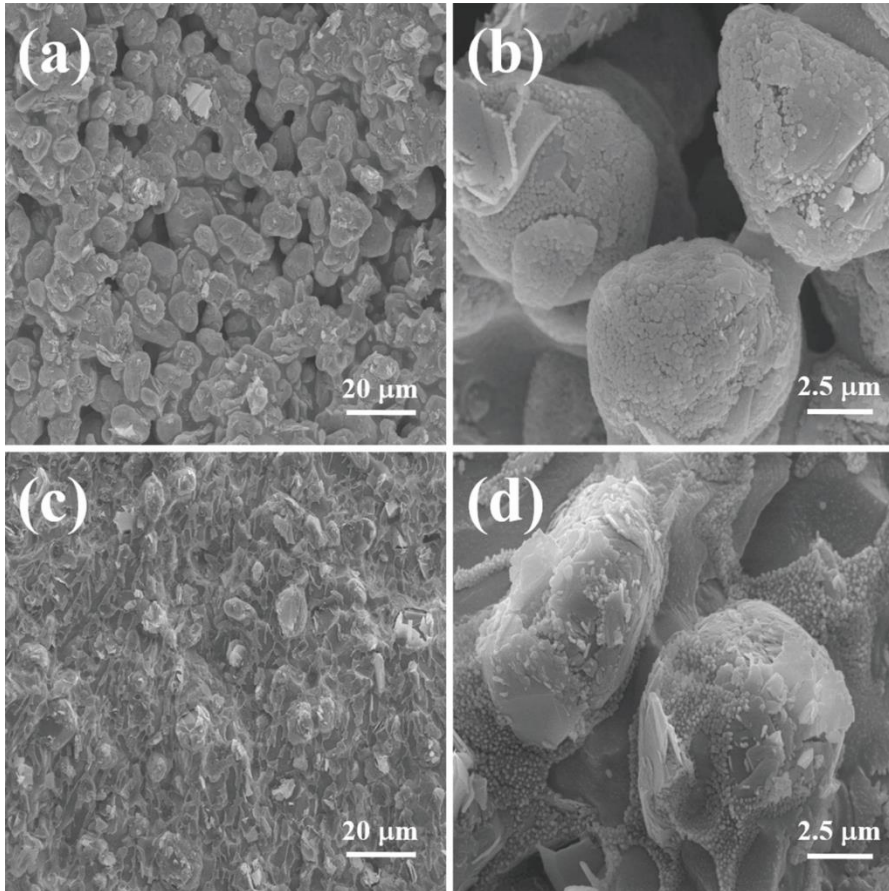


**Figure 4.1.2.** Cryo-SEM images of anode slurries containing 50 wt% of graphite and different concentrations of SBR; (a)&(b) graphite 50wt% + SBR 3wt%, (c)&(d) graphite 50wt% + 30wt%.



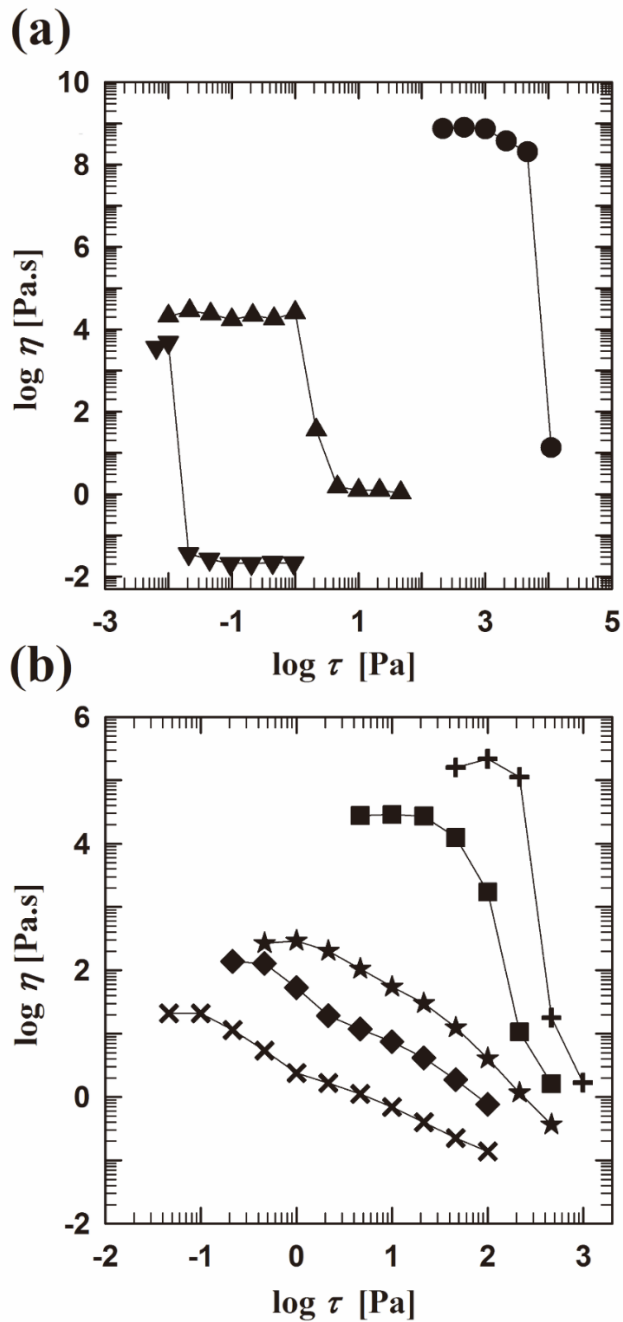
### 4.1.2. Graphite/CMC slurry

Figure 4.1.3 shows the viscosity for the slurries containing 50wt% of graphite and various concentration of CMC. The graphite slurry without CMC showed a yielding behavior, as mentioned in the section of graphite/SBR slurry. As the concentration of CMC was increased to 0.1wt%, both the viscosity and the yield stress decreased but the yielding behavior was still observed (Figure 4.1.3a). When the CMC concentration was increased above 0.4wt%, the behavior was totally changed. The yielding behavior disappeared and the shear thinning behavior appeared. In addition, the viscosity increased as the concentration of CMC was increased unlike at low CMC concentration (Figure 4.1.3b). As the CMC concentration was further increased to 1.4wt%, the yielding behavior in the slurry appeared again.

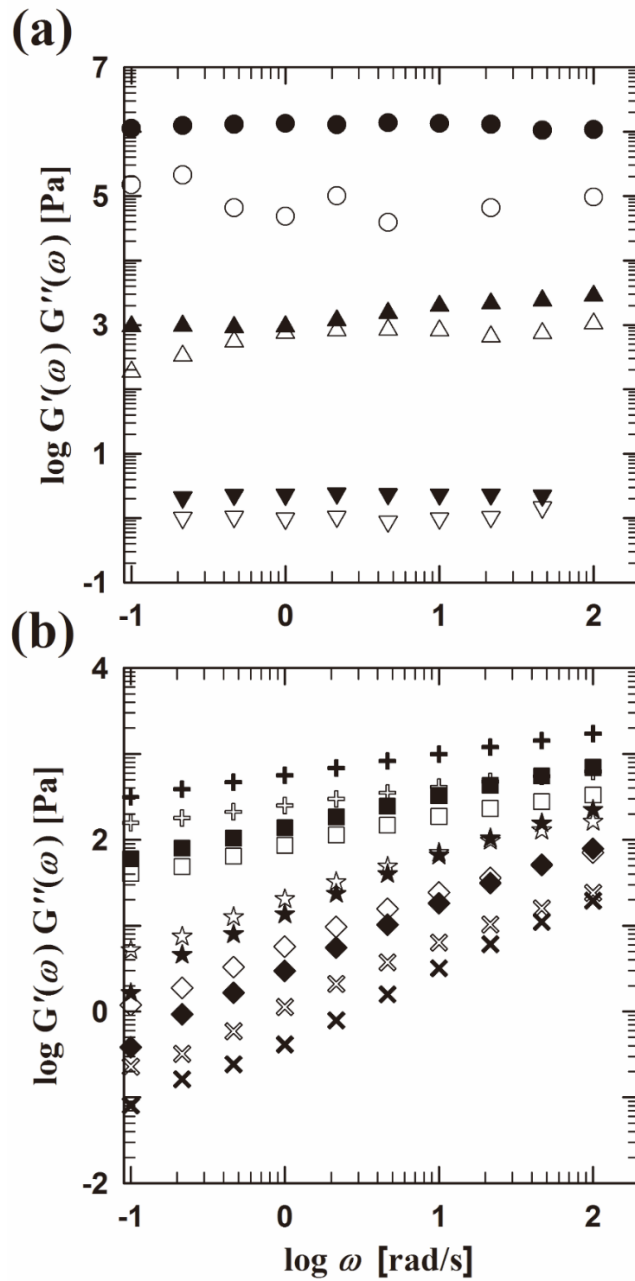
Figure 4.1.4 shows the viscoelastic behavior of the graphite slurries depending on the concentration of CMC. The  $G'$  was larger than  $G''$  and the moduli remained constant independent of frequency in the graphite slurry without CMC. As the concentration of CMC was increased to 0.1wt%, the moduli decreased, similar to the viscosity decrease at low CMC concentration as shown in Figure 4.1.3. The trend of frequency-independent modulus was maintained even when the CMC was added to the slurry, indicating the gel structure still existed in the slurry although the gel strength decreased.

The viscoelastic behavior was changed after 0.4wt% of CMC. The moduli increased with CMC concentration like the viscosity. In addition, the  $G''$  was larger than  $G'$  and the moduli increased with frequency. It means that the gel structure which was formed at low CMC concentration was changed to dispersion state as the CMC was further

added to the slurry. The moduli increased as the concentration of CMC was increased. However, when the CMC concentration was increased to 1.4wt%, the trend was changed again. The  $G'$  was larger than  $G''$  and the moduli showed power-law behavior with frequency. It means that the dispersed graphite particles was aggregated and formed the gel structure again at high CMC concentration. Therefore, it is clear that the microstructure of the slurry depended on the CMC concentration, and there exist transitions from gel to liquid and from liquid to gel structures.

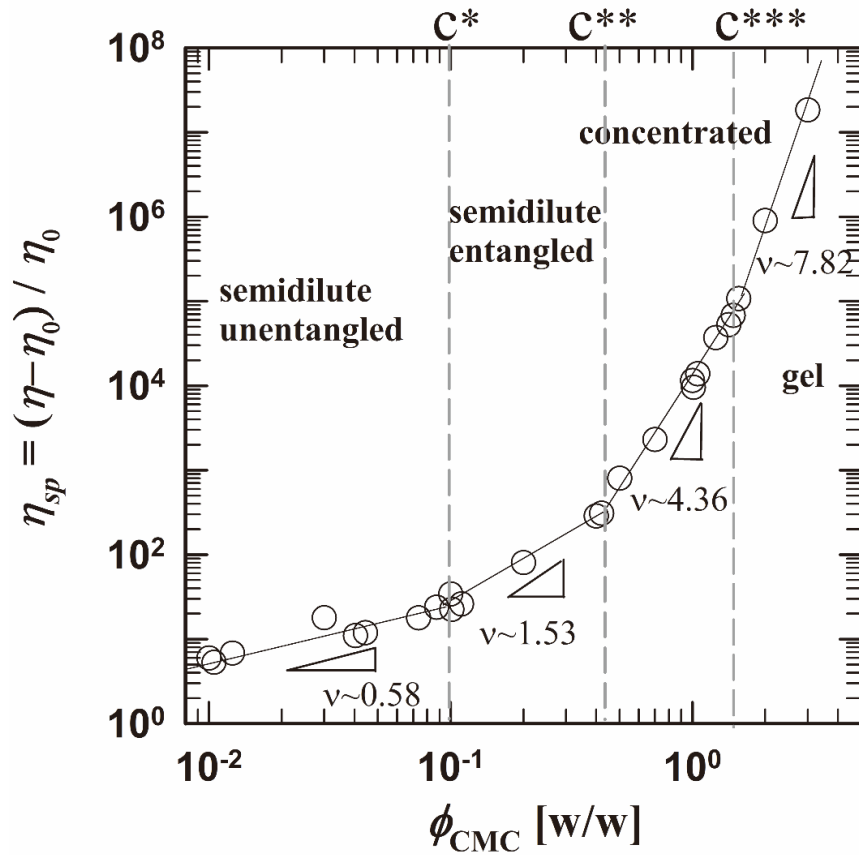


**Figure 4.1.3.** Viscosity as a function of shear stress for anode slurries containing 50wt% of graphite and various concentration of CMC; (●) 0wt%, (▲) 0.07wt%, (▼) 0.1wt%, (×) 0.4wt%, (◆) 0.7wt%, (★) 1.0wt%, (■) 1.4wt%, (+) 1.7wt%.

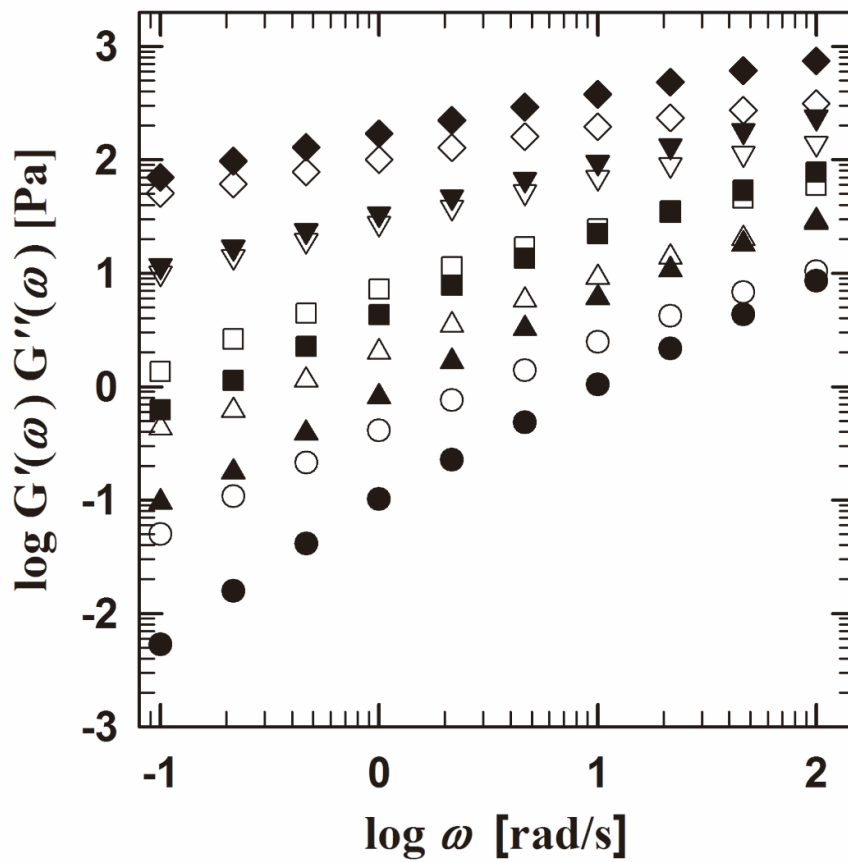


**Figure 4.1.4.** Storage (closed symbol) and loss (open symbol) moduli as a function of frequency for anode slurries containing 50 wt% of graphite and various concentration of CMC; (●) 0wt%, (▲) 0.07wt%, (▼) 0.1wt%, (×) 0.4wt%, (◆) 0.7wt%, (★) 1.0wt%, (■) 1.4wt%, (+) 1.7wt%.

The microstructure of CMC solution was investigated to study the microstructure transition of the anode slurries depending on the CMC concentration. The CMC is a polyelectrolyte which separates into a sodium cation and a polymer anion in an aqueous solution. These ions in a medium interact with each other by electrostatic forces and affect the polymer conformation [101]. Figure 4.1.5 shows the specific viscosity of CMC solution depending on the CMC concentration. The specific viscosity is defined as  $\eta_{sp} = (\eta - \eta_0) / \eta_0$ , where  $\eta$  is the zero viscosity of CMC solution and  $\eta_0$  is the viscosity of the medium. The specific viscosity increased as the concentration of CMC increased. The specific viscosity showed a power law behavior with the concentration of CMC,  $\eta_{sp} \sim c^\nu$ , and three transition concentration thresholds of CMC could be defined. (1) For  $c < c^*$ , the polymer chains dispersed in a dilute regime starts to overlap, and it is defined as the semidilute unentangled regime. In this regime, the specific viscosity follows the Fuoss law,  $\eta_{sp} \sim c^{1/2}$  [14-17]. (2) For  $c^* < c < c^{**}$ , the polymer chains form the entanglement, and it is defined as the semidilute entangled regime. In the regime, the specific viscosity follows  $\eta_{sp} \sim c^{3/2}$  [14-17]. (3) For  $c^{**} < c < c^{***}$ , it is defined as the concentrated regime and the specific viscosity in the regime follows  $\eta_{sp} \sim c^{3.75-5.5}$  [15-17]. (4) For  $c > c^{***}$ , the polymer solution shows a gel-like behavior, and the  $c^{***}$  is defined as the sol-gel transition concentration [17]. As shown in Figure 4.1.5, the slope of specific viscosity for CMC solution was obtained as  $\nu \sim 0.58, 1.53, 4.36,$  and  $7.82$  at each regime, respectively. These values were similar to the predictions obtained by the scaling theory in previous researches. In addition, the transition concentration thresholds were obtained as  $c^* \sim 0.1\text{wt}\%$ ,  $c^{**} \sim 0.4\text{wt}\%$ , and  $c^{***} \sim 1.6\text{wt}\%$  of CMC.



**Figure 4.1.5.** The specific viscosity as a function of polymer concentration for the CMC solution.



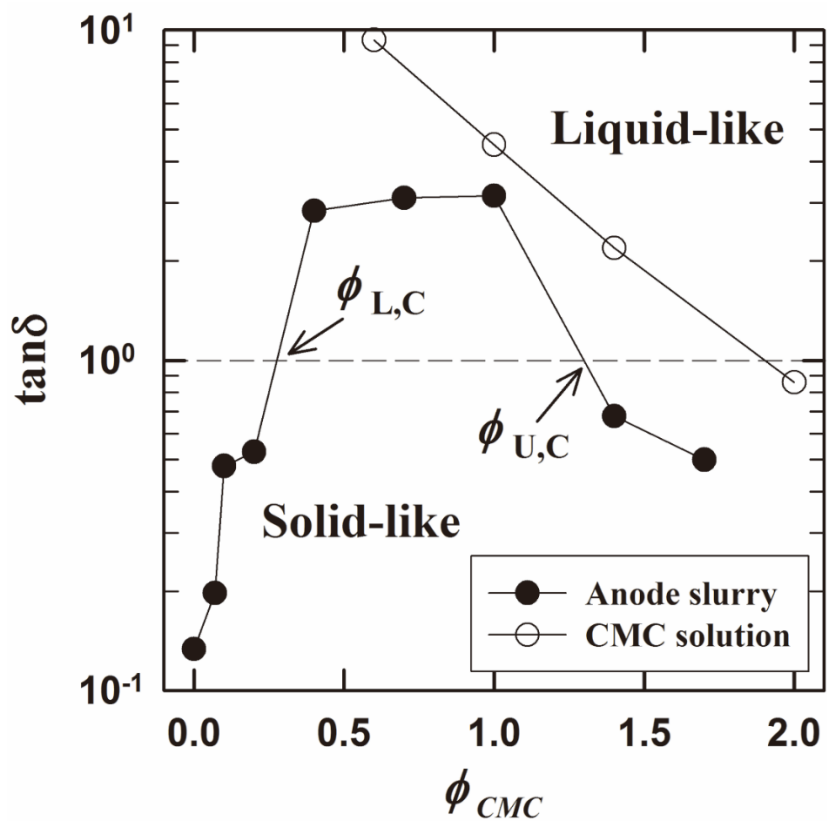
**Figure 4.1.6.** Storage (closed symbol) and loss (open symbol) moduli as a function of frequency for CMC solutions containing various concentration of CMC; (●): 0.6wt%, (▲): 1.0wt%, (■): 1.4wt%, (▼): 2.0wt%, (◆): 3.0wt%

Figure 4.1.6 shows the viscoelastic behavior of the CMC solution according to the CMC concentration. When the concentration of CMC was below 1.4wt%, the  $G''$  was larger than  $G'$  and the typical viscoelastic behavior of polymer solution was observed. However, when the concentration of CMC was above 2.0wt%, the  $G'$  is larger than  $G''$  and the moduli exhibited power-law behavior, indicating that the CMC formed the polymeric networks, the gel structure [102]. The gel behavior was observed above the sol-gel transition concentration,  $c^{***}$ , as mention in Figure 4.1.5.

Figure 4.1.7 shows the  $\tan\delta$  for the anode slurry and the CMC solution as a function of the concentration of CMC. The  $\tan\delta$  was defined as the ratio of  $G''$  and  $G'$ , and was obtained at  $\omega=0.1\text{rad/s}$ . The  $\tan\delta$  of the anode slurry at low concentration of CMC was below unity, and it increased above unity after critical concentration of CMC,  $\phi_{LC} \sim 0.28\text{wt\%}$ . When the CMC concentration was below 0.28wt% in the anode slurry, the moduli were independent on the frequency (Figure 4.1.4). It means that the gel structure was formed by graphite particles when the low concentration of CMC was added to the slurry. As mentioned in the section of graphite/SBR slurry, the gel structure was formed by hydrophobic attraction of graphite particles, and the graphite particles were dispersed by adsorbed SBR on the surface of graphite. Like SBR, the CMC molecules tended to adsorb on the graphite surface, and the adsorption amount of CMC increased as the CMC concentration was increased [11,35]. Therefore, the viscosity and the moduli decreased as the CMC whose concentration was below 0.28wt% was added to the slurry, meaning that the gel strength decreased due to adsorbed CMC on the surface of graphite. However, the frequency-independent behavior of the moduli was shown, indicating that



the gel structure by graphite particles still existed in the slurry. The gel structure by graphite could be confirmed by the cryo-SEM images (Figure 4.1.8a & b).



**Figure 4.1.7.**  $\tan \delta$  as a function of CMC concentration for anode slurries containing 50 wt% of graphite (●) and CMC solution (○).

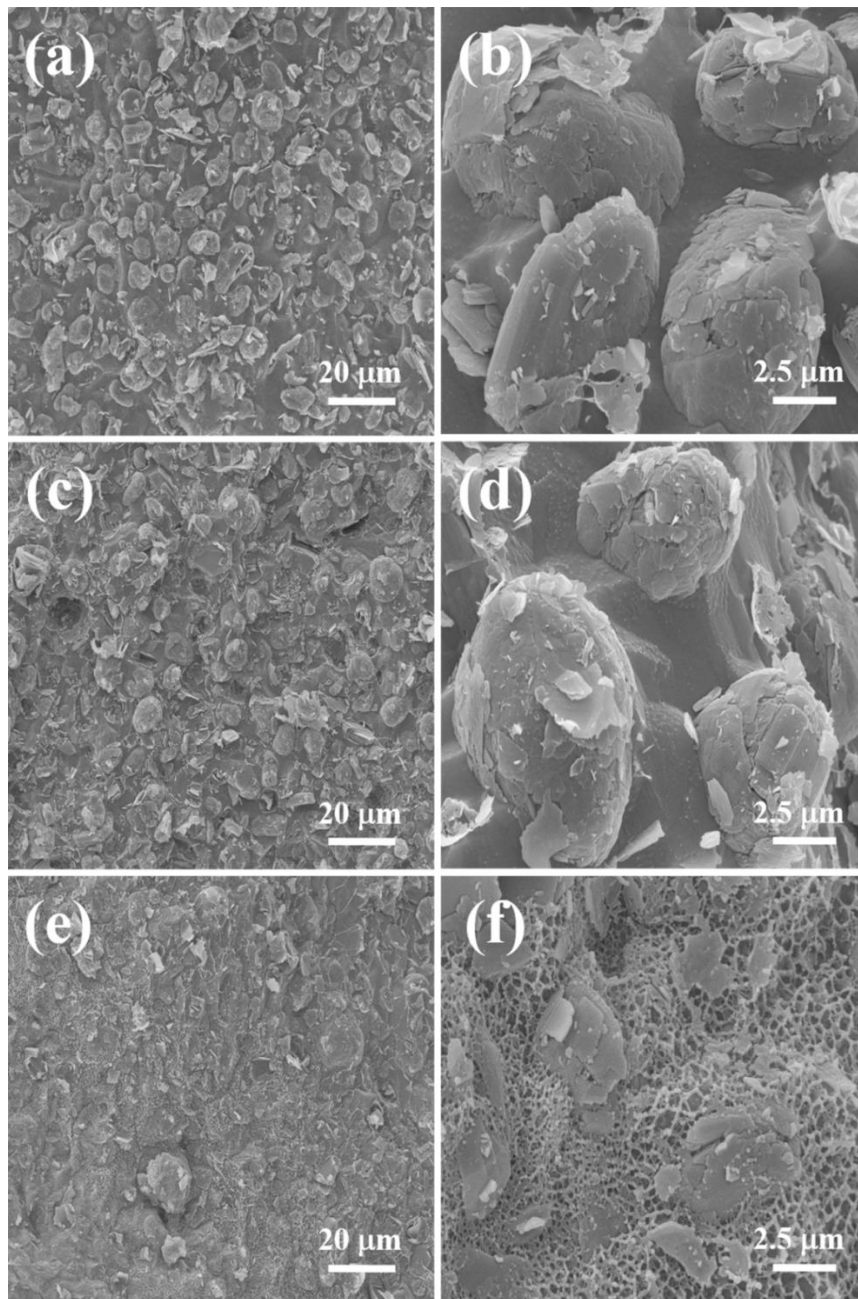


**Figure 4.1.8.** Cryo-SEM images of anode slurries containing 50 wt% of graphite and different concentrations of CMC; (a)&(b) graphite 50wt% + CMC 0.07wt%, (c)&(d) graphite 50wt% + CMC 0.7wt%, (e)&(f) graphite 50wt% + CMC 1.7wt%.

The  $\tan\delta$  increased with CMC concentration, and it was larger than unity after  $\phi_{L,C}$ . It means that the gel structure at the low CMC concentration disappeared and the slurry showed a liquid-like behavior. The dependence of microstructure on the CMC concentration could be explained by the characteristic of CMC which could adsorb on the graphite surface. The carboxymethyl unit in the CMC molecule was dissociated to  $\text{COO}^-$  unit in the aqueous solution. So, the adsorption amount of CMC on the graphite surface increased as the CMC concentration was increased, and the graphite particles were dispersed by electrosteric repulsion from the adsorbed CMC molecules. The well-dispersed graphite particles by CMC could be confirmed by cryo-SEM images (Figure 4.1.8c & d).

As the concentration of CMC was further increased, the  $\tan\delta$  remained above unity until a critical concentration where it starts to decrease to a value below unity. The critical concentration was defined as the upper critical concentration,  $\phi_{U,C}$ , and it was approximately 1.3wt%. That is, the liquid-like behavior in the slurry was changed to the solid-like behavior from 1.3wt% of CMC. The microstructure change could be explained by the characteristic of CMC which formed the gel structure at high CMC concentration. The  $\tan\delta$  of CMC solution was above unity, and it decreased as the CMC concentration was increased. The  $\tan\delta$  of CMC solution decreased under unity through the 1.9wt% of CMC (Figure 4.1.7). In addition, it was already confirmed that the CMC molecules formed the gel structure above 1.9wt% of CMC concentration, as shown in Figure 4.1.5. Therefore, the gel structure of CMC when the CMC concentration was above  $\phi_{U,C}$  had an effect on the solid-like behavior of the anode slurry. The microstructure of the slurry containing high CMC concentration was also observed by

cryo-SEM (Figure 4.1.8e & f). The microstructure of the slurry containing high CMC concentration was different from that of the slurry containing low CMC concentration as shown in Figure 4.1.8(d) & (f). That is, for the slurry with high CMC concentration, network structure is formed, in which the graphite particles are embedded (Figure 4.1.8f). The network was the gel structure formed by the polymeric network of CMC molecules and the size of hexagon lattice was less than 500nm in the anode slurry. The cryo-SEM images for the 2wt% of CMC solution were taken in order to confirm whether the network structure is formed by CMC or not (Figure 4.1.9). The honeycomb-like structure was observed in Figure 4.1.9(a), but the structure is the artifacts which results from free water crystallization when the aqueous solution is frozen in a liquid nitrogen [103]. In addition, the size of hexagon lattice for frozen water was about micron scale, it disagreed with the size of network structure appearing in the anode slurry in Figure 4.1.8(f). However, when the cryo-SEM image was enlarged with high magnification, the network structure could be observed which was exposed from freezing water (Figure 4.1.9b). The size of the structure is about a few hundred nanometer scales, and the network size was the same as in the anode slurry. In addition, there is a report that the CMC molecules form the network structure by Müller et al. [104]. So, it could be argued that the network structure in anode slurry at high concentration of CMC was originated from CMC molecules.

Therefore, the CMC molecules formed the network structure as the concentration was increased, and the graphite particles, which were well dispersed at intermediate concentration,  $\phi_{L,C} < c < \phi_{U,C}$ , were trapped in the network structure of CMC. So, the anode slurry behaved solid-like above  $\phi_{U,C}$ .

At both concentrations below the  $\phi_{L,C}$  and above the  $\phi_{U,C}$  of the CMC, the gel behavior in the slurry was observed, but the gel structures were different from each other. In other words, the gel structure was formed by the aggregation of graphite particles due to hydrophobic attraction below the  $\phi_{L,C}$  of the CMC, while the polymeric network induced the gel structure in the slurry above the  $\phi_{U,C}$  of the CMC.

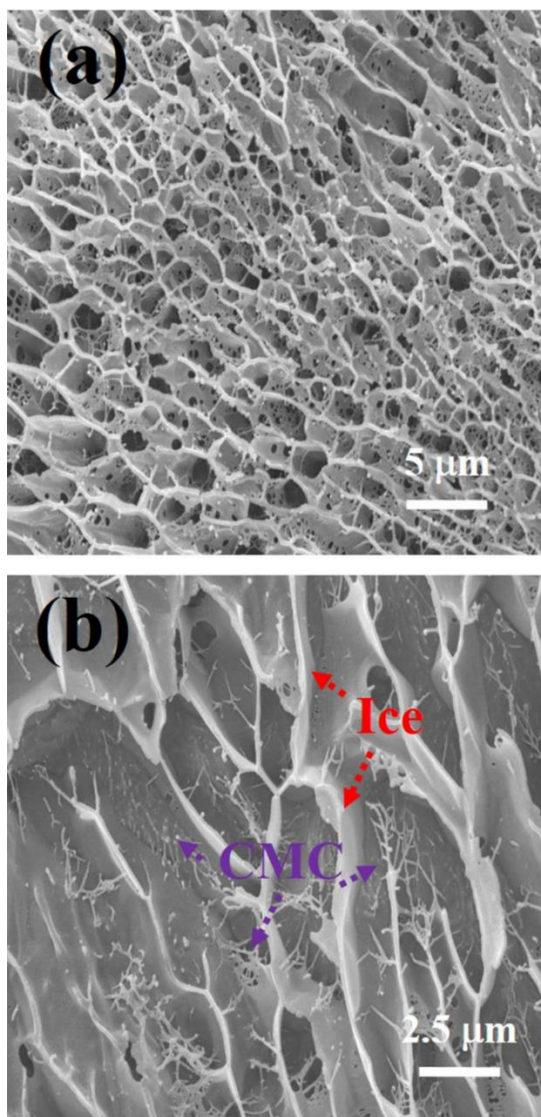


**Figure 4.1.9.** Cryo-SEM images of 2wt% CMC solution with magnification of 15,000 (a) and 30,000 (b).

### 4.1.3. Graphite/CMC/SBR slurry

Figure 4.1.10~4.1.12 show the rheological properties for the slurries containing various concentration of CMC and SBR, from 0.07 to 1.7wt% and 2 to 5wt%, respectively. As mentioned in the previous section, the CMC as well as the SBR adsorbed on the graphite surface affect the dispersion of the graphite particles. As shown in Figure 4.1.10, when the slurry contained the low concentration, 0.07wt%, of CMC without SBR, the graphite particles formed the gel structure inducing yielding and frequency-independent modulus. As 2 or 5wt% of SBR was added to the slurry, both the viscosity and the modulus decreased. The rheological properties decreased as the SBR was added to the slurry because the graphite particles were dispersed due to the adsorbed SBR on the graphite surface. The microstructure of the slurry could be confirmed by cryo-SEM images (Figure 4.1.13a & b). While the graphite particles formed the gel structure in the slurry containing only 0.07wt% of CMC without SBR (Figure 4.1.8b), the graphite particles were dispersed by adsorbed SBR on the graphite surface in the slurry containing 0.07wt% of CMC and 5wt% of SBR (Figure 4.1.13b). That is, in the slurry with low concentration of CMC, the SBR could adsorb on the graphite surface because the adsorption amount of CMC on the graphite was very small. So, the SBR adsorbed on the graphite surface forced the graphite particles to disperse, causing the decrease of both viscosity and modulus.

In the slurry containing 0.7wt% of CMC, the yielding behavior disappeared and the viscoelastic behavior in which the  $G''$  was larger than  $G'$  and the moduli increases with frequency (Figure 4.1.11). However, the rheological properties of the slurry did not



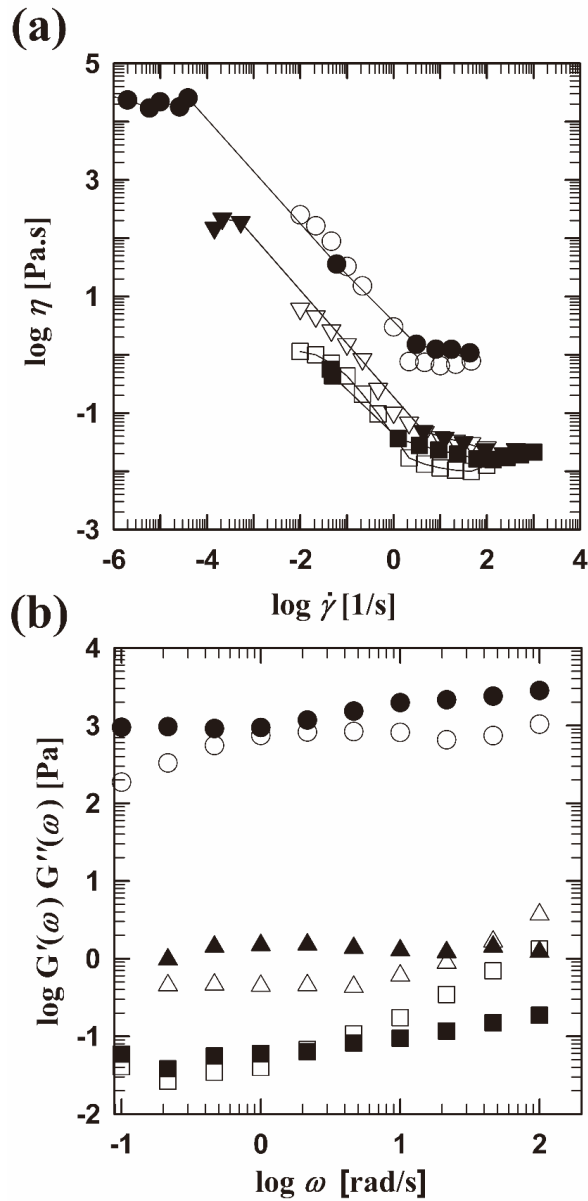


**Figure 4.1.10.** Rheological properties of anode slurries containing 50wt% of graphite, 0.07wt% of CMC, and various concentration of SBR. (a) Viscosity as a function of shear rate; obtained from the stress controlled (closed symbol) and rate controlled (open symbol) rheometer, (b) Storage (closed symbol) and loss (open symbol) moduli as a function of frequency; ( $\bullet$  $\circ$ ) 0 wt%, ( $\blacktriangle$  $\triangle$ ) 2 wt%, ( $\blacksquare$  $\square$ ) 5 wt% of SBR concentration.

change although the SBR was added unlike the slurry with low concentration of CMC. Li and Lin [78] investigated the characteristic of adsorption for the binder on the graphite according to mixing protocol. One of the mixing protocols is that both CMC and SBR were added and mixed to the slurry simultaneously. Another is that the CMC was added to the slurry first and the SBR was added followed by mixing with the slurry. In the case of split addition of binders to the slurry, the graphite particles were dispersed by the adsorbed CMC on the graphite surface as the CMC was added to the slurry first. Then, when the SBR was added to the slurry, the SBR could not adsorb on the graphite and could not affect the dispersion of the graphite particles. In the case of adding binders to the slurry simultaneously, the SBR could not adsorb on the graphite surface too because the CMC has already been adsorbed on the graphite surface. That is, when both CMC and SBR existed in the slurry simultaneously, the CMC adsorbed on the graphite surface more preferably than the SBR, and it played a dominant role in dispersing the graphite particles. As shown in Figure 4.1.11, the viscosity as well as the modulus remained constant although the concentration of SBR was increased, meaning that the SBR could not affect the dispersion of the graphite particles any more. Figure 4.1.13(c) & (d) illustrate cryo-SEM images of microstructure for the slurry containing 0.7wt% of CMC and 5wt% of SBR. While the SBR adsorb on the graphite surface in the slurry containing low concentration of CMC (Figure 4.1.13b), the SBR existed only in the medium, not on the graphite surface (Figure 4.1.13d). In other words, the adsorption amount of CMC on the graphite surface increased as the concentration of CMC was increased. The SBR could not adsorb on the graphite due to the adsorbed CMC in advance, and stayed in the medium. Therefore, the dispersion of graphite particles was

influenced mostly by the adsorbed CMC and the SBR which existed in the medium could not affect the dispersion of the graphite particles. Thus, the rheological properties of the slurry was constant although the concentration of SBR was increased.

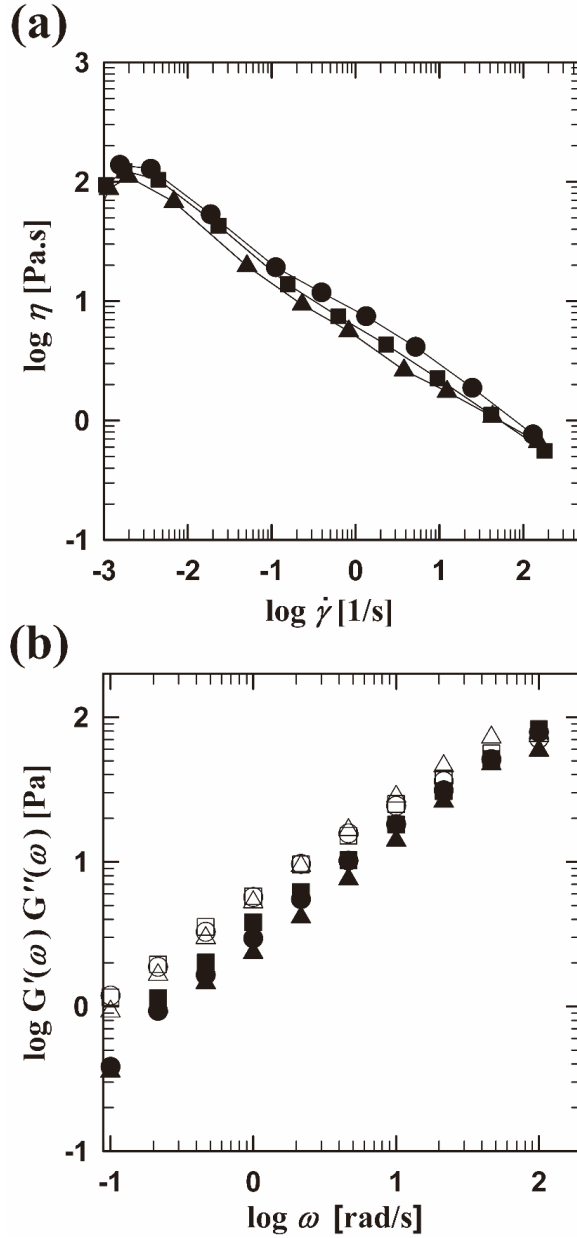


**Figure 4.1.11.** Rheological properties of anode slurries containing 50wt% of graphite, 0.7wt% of CMC, and various concentration of SBR. (a) Viscosity as a function of shear rate, (b) Storage (closed symbol) and loss (open symbol) moduli as a function of frequency; ( $\bullet$  $\circ$ ) 0 wt%, ( $\blacktriangle$  $\Delta$ ) 2 wt%, ( $\blacksquare$  $\square$ ) 5 wt% of SBR concentration.

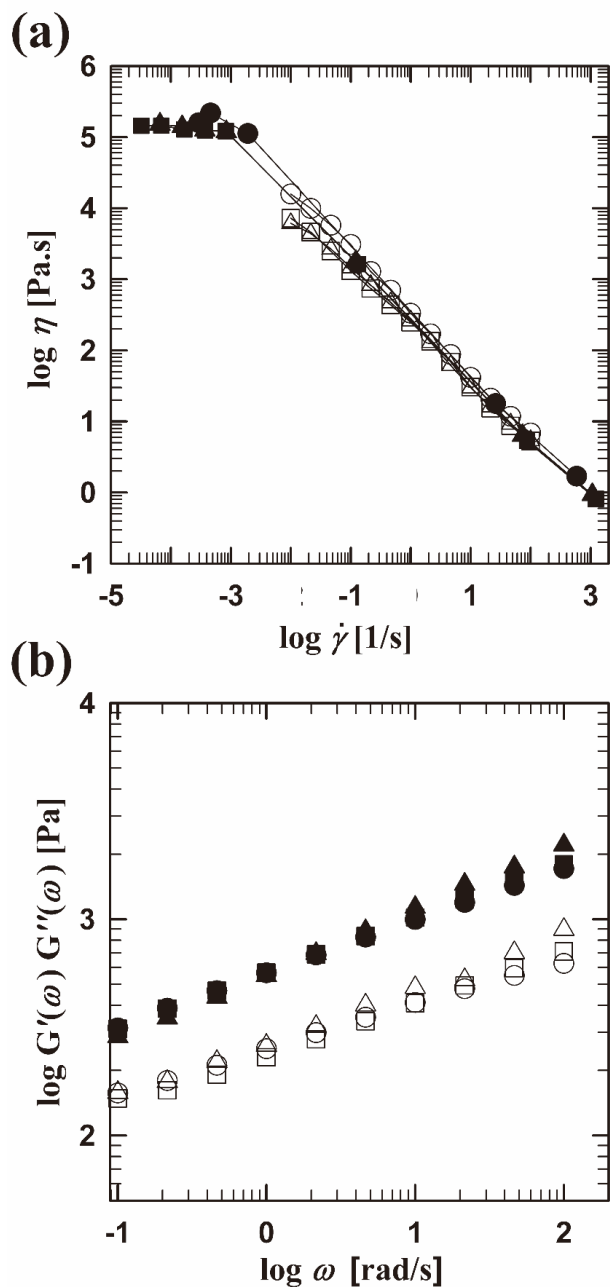


**Figure 4.1.12.** Rheological properties of anode slurries containing 50wt% of graphite, 1.7wt% of CMC, and various concentration of SBR. (a) Viscosity as a function of shear rate, (b) Storage (closed symbol) and loss (open symbol) moduli as a function of frequency; ( $\bullet$  $\circ$ ) 0 wt%, ( $\blacktriangle$  $\triangle$ ) 2 wt%, ( $\blacksquare$  $\square$ ) 5 wt% of SBR concentration.

The trend, in which the rheological properties of the slurry stayed constant although the concentration of SBR was increased, was also shown in the slurry containing 1.7wt% of CMC (Figure 4.1.12). It was confirmed that the graphite/CMC slurry with 1.7wt% of CMC showed the gel behavior due to the polymeric network by CMC molecules (Figure 4.1.8f). When the SBR was added to the slurry containing 1.7wt% of CMC, the polymeric network could also be found in the slurry (Figure 4.1.13f). In addition, the SBR did not exist on the graphite surface in the slurry with 1.7wt% of CMC as in the slurry with 0.7wt% of CMC. Figure 4.1.14 shows the enlarged image of the CMC network structure in the slurry with 1.7wt% of CMC. It could be found that the SBR which could not adsorb on the graphite particles existed at the polymeric network structure. Therefore, in the slurry with high concentration of CMC, the SBR could not affect the dispersion of the graphite particles and only CMC played a leading role in forming the microstructure in the slurry.

To summarize, when the anode slurry containing low concentration of CMC, SBR could adsorb on the graphite surface and affect the dispersion of the graphite. On the other hand, as the concentration of CMC was increased, the adsorption amount of CMC was also increased. Then, the SBR could not adsorb on the graphite surface and could not have an influence on the dispersion of the graphite particles. The CMC played a primary role in forming the microstructure of the slurry.

Until now, the effect of binders, both CMC and SBR, on the microstructure formation in the anode slurry was investigated by analyzing the rheological properties and cryo-SEM images. I figured out that the microstructural change of the slurry, such as from gel to dispersion, and vice versa, depended on the concentration of binders. Especially,

in the slurry containing both CMC and SBR, the effect of SBR on the microstructure was different depending on the CMC concentration. It is expected that understanding the effect of the binders on the microstructure formation of the slurry can help the design of slurry in the manufacturing process of the battery.

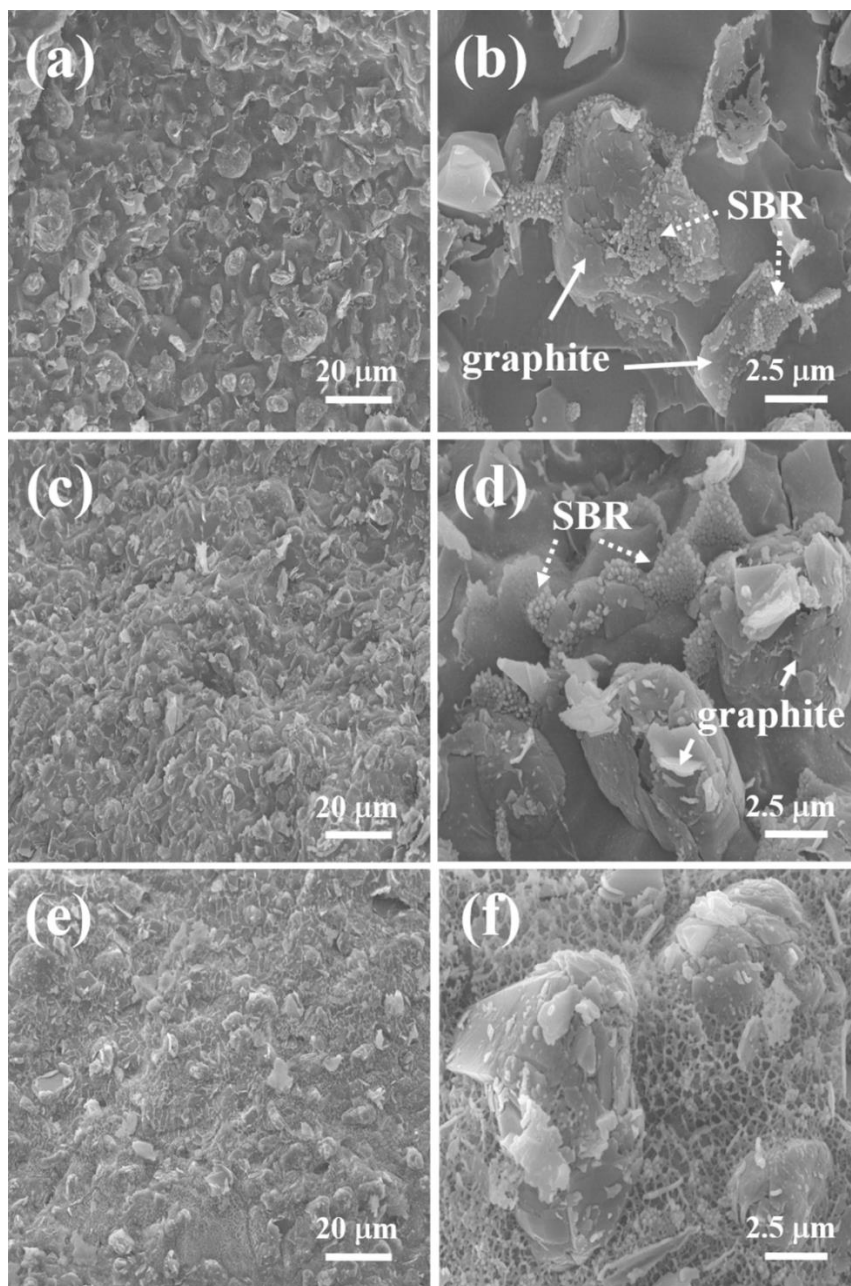


**Figure 4.1.13.** Cryo-SEM images of anode slurries containing 50 wt% of graphite and different concentrations of CMC and SBR; (a)&(b) graphite 50wt% + CMC 0.07wt% + SBR 5wt%, (c)&(d) graphite 50wt% + CMC 0.7wt% + SBR 5wt%, (e)&(f) graphite 50wt% + CMC 1.7wt% + SBR 5wt%.



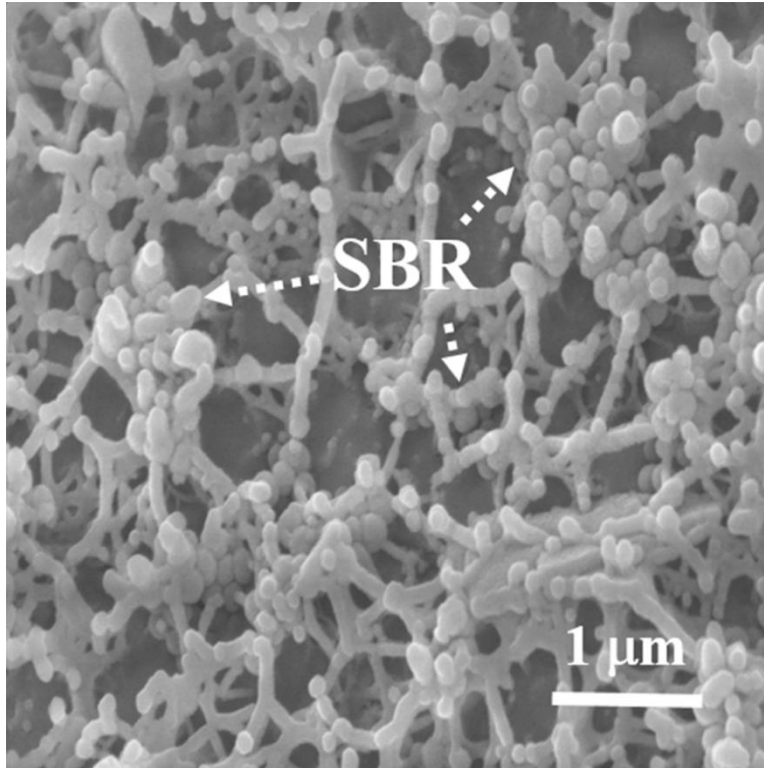


**Figure 4.1.14.** Enlarged image by Cryo-SEM for slurry containing 50wt% of graphite, 1.7wt% of CMC and 5wt% of SBR.

## **4.2. Drying behavior of anode slurry**

### **4.2.1. Graphite/SBR slurry**

#### **4.2.1.1. Drying stress of graphite/SBR slurry**

Figure 4.2.1 shows the development of drying stress for anode slurries containing 50wt% of graphite particles and various concentrations of SBR. For graphite slurries without SBR and with 3wt% of SBR, the drying stress first increased to maximum, followed by a decay to the stress-free state. A similar tendency appears in the suspension with inorganic particle or hard sphere or high  $T_g$  latex [44-47]. The stress is generated in the film due to the constrained shrinkage during drying. However, if there is no binder or not enough binder in the film, the drying stress decays to the stress-free state because the film cannot endure the stress generated by drying.

As the concentration of SBR increased to 8wt%, the drying stress developed to the 1<sup>st</sup> peak followed by a weak relaxation of the stress, and additional increment to the 2<sup>nd</sup> peak followed by a relaxation towards a plateau. The development of drying stress with double peak was previously observed [44,45,48]. Wedin et al. [44,45] reported the development of drying stress for  $\text{CaCO}_3$  suspension with polymer, plasticizer, and surfactant. The double peak appeared in  $\text{CaCO}_3$  suspension with CMC or deformable latex. The 1<sup>st</sup> peak occurred due to the capillary pressure which was generated at the pore between the calcium carbonate particles, where the 2<sup>nd</sup> maximum was generated due to the CMC or coalescence of deformable latex.

The capillary pressure which is generated at the meniscus between the particles can be obtained by Young-Laplace equation [105].

$$P_{cap} = \frac{2\gamma \times \cos\theta}{r_p}, \quad (4.2.1)$$

where  $P_{cap}$ ,  $\gamma$ ,  $\theta$ , and  $r_p$  are the capillary pressure, liquid/vapor surface tension, liquid/solid contact angle and the pore radius, respectively.

The equivalent pore radius in film can be estimated through the hydraulic radius because the tortuous capillary pores among the particles are not similar with cylindrical tubes [45].

$$r_h \sim r_p = \frac{2(1-\phi)}{\phi \rho_s S}, \quad (4.2.2)$$

where  $\phi$ ,  $\rho_s$ , and  $S$  are the particle volume fraction, the density of solid phase and surface area of particles, respectively. The solid volume fraction,  $\phi$ , at maximum stress was about 0.43 according to the weight loss measurement. So, the capillary pressure,  $P_{cap}$ , could be obtained as approximately 0.07 MPa for the slurry without SBR. This pressure was similar to the stress level of the graphite slurries with 3 and 8wt% of SBR. Thus, it could be confirmed that the 1<sup>st</sup> peak was generated due to the capillary pressure by graphite particles, followed by the SBR-induced 2<sup>nd</sup> peak and the residual stress.

The tendency of drying stress development was changed as the SBR concentration was increased to 15 and 30wt%. The stress increased steeply at the initial stage of drying, and reached to the maximum stress followed by a relaxation to the residual stress. On the other hand, in the case of SBR suspension without graphite particles, the stress increased slowly compared with anode slurry. Then, it reached the maximum stress followed by a relaxation to the residual stress. The development behavior of drying stress according to the latex concentration has been reported for an inorganic particle/latex system [48]. Kiennemann et al. [48] investigated the drying behavior of  $\text{Al}_2\text{O}_3$ /acrylic latex suspension depending on the latex concentration. The double peak was also observed at low concentration of latex. However, it disappeared and only a single peak appeared at higher latex concentration. After that, the drying stress developed smoothly to the final stress without a peak as the latex concentration was further increased. This behavior was similar to the anode slurry depending on the SBR concentration. In other words, the double peak which appeared in graphite slurry with 8wt% of SBR turned to the single peak as the SBR concentration was increased.

With the increase of SBR concentration, both the residual stress and maximum stress as well as the form of stress peak were changed. Figure 4.2.2 shows both the residual and the maximum stress as a function of SBR concentration for graphite/SBR slurry. The residual stress and maximum stress increased linearly from 5wt% and 7wt% of SBR, respectively. Both final stress and maximum stress maintained the stress level at first, approximately 0.02 and 0.07 MPa, respectively, and increased almost linearly from the critical concentration of SBR. Thus, SEM images and pore size distribution in

dried film were investigated to figure out the effect of SBR on the development of drying stress.

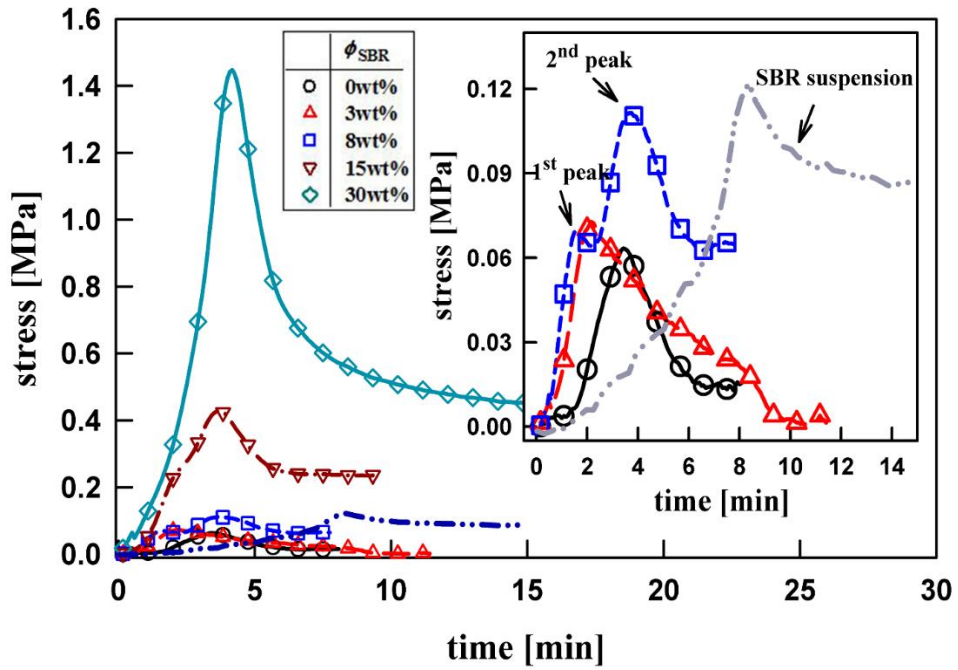


**Figure 4.2.1.** Drying stress of graphite slurries containing 50wt% of graphite and various concentration of SBR. Drying temperature is 25°C and relative humidity is 20%.

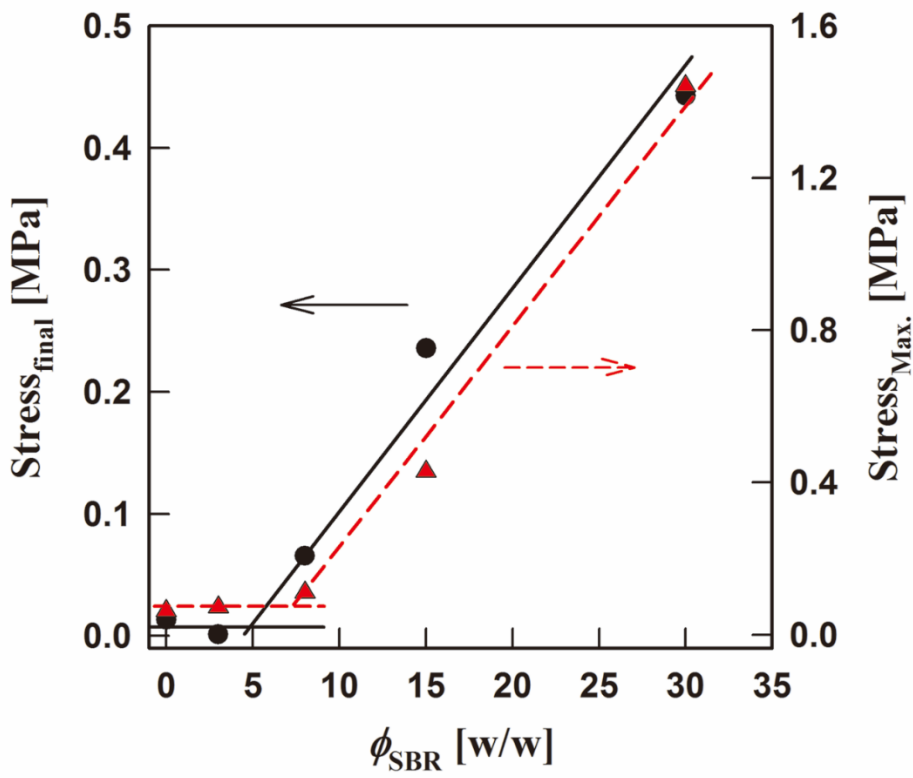


**Figure 4.2.2.** Residual and maximum stress as a function of SBR concentration.

#### **4.2.1.2. Microstructure of film for graphite/SBR slurry**

Figure 4.2.3 shows the SEM images for the slurries containing 50wt% of graphite particles and various concentration of SBR. In the slurry with 3wt% of SBR, there were only graphite particles in the film when observed at low magnification (Figure 4.2.3(a)). However, observation at high magnification confirmed the presence of SBR, which formed bridges among the graphite particles (indicated by the arrow in the inset of Figure 4.2.3(a)). The graphite particles were connected with more SBR when the SBR concentration was 8wt%, but the film was still structured mostly by the graphite particles (Figure 4.2.3b). However, the film formation was changed as the SBR concentration increased over 15wt%. The SBR which existed among graphite particles as a bridge at low SBR concentration filled the pores among the graphite particles when 15wt% of SBR was contained in the graphite slurry (Figure 4.2.3c). In addition, as the SBR concentration was increased to 30wt%, the SBR not only filled the pores, but also covered the graphite particles (Figure 4.2.3d). The dependence on the SBR concentration could also be confirmed by the pore size distribution of the dried film.



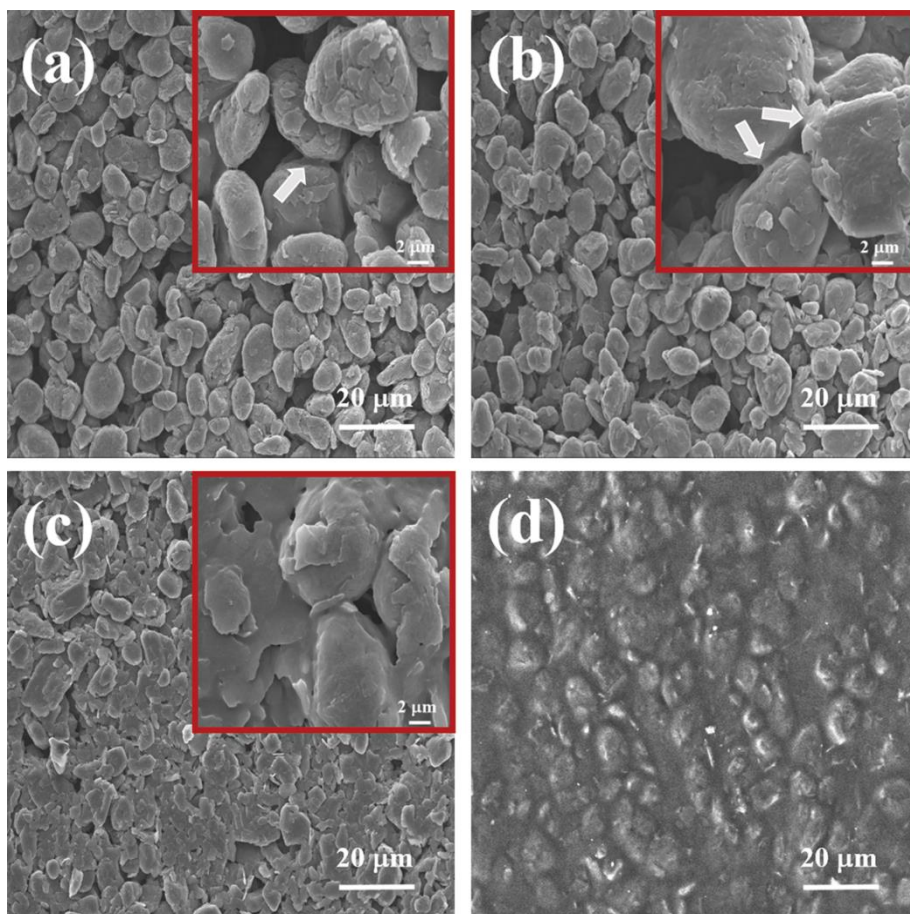


**Figure 4.2.3.** SEM images of dried film for anode slurries containing 50wt% of graphite and various concentration of SBR: (a) graphite 50wt% + SBR 3wt%, (b) graphite 50wt% + SBR 8wt%, (c) graphite 50wt% + SBR 15wt%, and (d) graphite 50wt% + SBR 30wt%. Insets in (a) ~ (c) are enlarged images of surfaces, respectively.

Figure 4.2.4 shows the pore size distribution in the dried film of graphite/SBR slurry depending on the SBR concentration. There were many pores with 1.6 ~ 5 $\mu$ m of diameter in the film containing 3wt% of SBR. As the SBR concentration increased to 8wt%, the pore with 600nm of diameter appeared. In addition, when the SBR concentration was further increased, the number of pores was decreased. As shown in table 4.2.1, the average pore size as well as the porosity decreased as the SBR concentration was increased. The trend of pore size distribution depending on SBR concentration was similar to the film formation in SEM images. That is, the number of pores was diminished in the film as the SBR filled the pores between the graphite particles.

Therefore, the cause of the increase in both final and maximum stress in Figure 4.2.2 could be explained by SBR-induced microstructure of the film. In other words, SBR, when added to the film, participated in bridging the graphite particles in the film at first. As the SBR concentration was further increased, the SBR filled the pores among the graphite particles and a film was formed by a coalescence between SBRs, inducing an increase of drying stress.

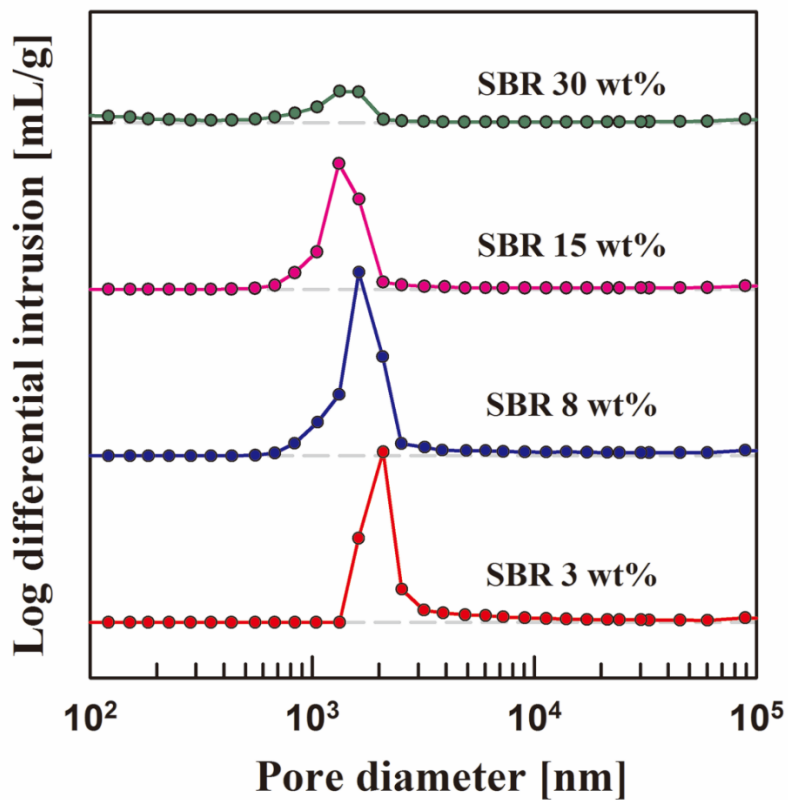


**Figure 4.2.4.** Pore size distribution in dried film containing 50wt% of graphite and various concentration of SBR. The interval in y-axis (horizontal grey dashed line) represents 1.5 mL/g..

**Table 4.2.1.** Average pore diameter and porosity for dried film containing 50wt% of graphite and various concentration of SBR.

Sample ( $\phi_{\text{graphite}}/\phi_{\text{SBR}}$ )	Average pore diameter [nm] <sup>a</sup>	Porosity [%] <sup>b</sup>
50wt% / 3wt%	2694.3	48.48
50wt% / 8wt%	2062.2	40.21
50wt% / 15wt%	1685.8	31.64
50wt% / 30wt%	64.9	25.87

<sup>a</sup> average pore diameter =  $4 \times (V_{\text{tot}}/S_{\text{tot}})$  where  $V_{\text{tot}}$  and  $S_{\text{tot}}$  are the total volume of intruded mercury and the total area of pore surface, respectively [106].

<sup>b</sup> porosity =  $(V_{\text{pore}}/V_{\text{bulk}}) \times 100$

## **4.2.2. Graphite/CMC slurry**

### **4.2.2.1. Drying stress of graphite/CMC slurry**

Figure 4.2.5 shows the development of drying stress for anode slurries containing 50wt% of graphite and various concentration of CMC. The drying stress, in the case of graphite slurry without CMC, increased to the maximum at the initial stage followed by a decay to the stress-free state. Such drying behavior was maintained even with a small increase in the CMC concentration. The behavior of drying stress for the graphite slurry with 0.07wt% of CMC was similar to that for the graphite slurry without CMC. When the CMC concentration was increased to 0.3wt%, the drying stress developed to a maximum followed by relaxation, but the film exhibited residual stress of approximately 0.06MPa. The value of maximum peak was approximately 0.08MPa in the slurries without CMC and with low CMC concentration, thus it was confirmed that the maximum peak was induced by the capillary pressure generated by the graphite particles. When the CMC concentration was increased to more than 0.5wt%, the drying stress reached at maximum and was maintained near the maximum value. After that, the final stress was increased with the CMC concentration. The final stress was plotted as a function of CMC concentration to figure out the effect of CMC on the development of drying stress (Figure 4.2.6).

As mentioned previously, the drying stress relaxed to the stress-free state through the maximum stress peak for the graphite slurries with low CMC concentration. After the CMC concentration reached 0.27wt%, the residual stress began to develop (Figure

4.2.6). There were some studies in which the polymer had an influence on the development of drying stress in particle/polymer suspension [44,45,49]. Wedin et al. [44,45] investigated the drying stress with and without CMC in CaCO<sub>3</sub> suspension. The drying stress relaxed to the stress-free state after maximum in CaCO<sub>3</sub> suspension without polymer, while there was no stress relaxation and the stress stayed at the maximum in CaCO<sub>3</sub> suspension with the polymer. Lewis et al. [49] studied the drying stress depending on the presence of plasticizer in Al<sub>2</sub>O<sub>3</sub>/PVB suspension. The drying stress relaxed slightly after maximum in the plasticizer-free suspension, while it relaxed steeply after maximum in the suspension with plasticizer. In addition, the suspension with a polymeric latex instead of the polymer showed a similar trend of drying stress [46,48,50]. Kiennemann et al. [48] investigated the drying stress according to the glass transition temperature, T<sub>g</sub>, of latex in Al<sub>2</sub>O<sub>3</sub>/acrylic latex suspension. If the T<sub>g</sub> of latex was higher than the drying temperature, the drying stress sharply decayed to the stress-free state after reaching maximum. On the other hand, if the T<sub>g</sub> of latex was lower than the drying temperature, the drying stress slightly decayed after the maximum but the residual stress still remained. Price et al. [50] reported the drying behavior according to the shell ratio in suspensions containing soft-core/hard-shell particles. The drying stress in the suspension with thin hard-shell developed and reached to the maximum stress, while it, in the suspension with thick hard-shell, steeply decayed after maximum and a crack was generated in the film. They all confirmed that the film exhibited insufficient mechanical strength when there was no residual stress. On the other hand, if the residual stress was present, the film was generated with good mechanical strength. Based on the previous researches, the graphite/CMC slurry with below 0.27wt% of CMC could not

form the film with sufficient mechanical strength, while the slurry with above 0.27wt% of CMC could form the film with sufficient mechanical strength.

The increasing trend of drying stress with the increase in CMC concentration could be explained by the adsorption characteristic of CMC on the surface of graphite particles [11,35]. Kim et al. [43] investigated a relationship between the adsorption amount of PVA and the drying stress in silica/PVA suspensions. The adsorption amount of PVA was changed according to pH and mixing time. The drying stress increased as the adsorption amount of PVA increased. In addition, the adsorption amount according to mixing time and the drying stress were superposed onto a single master curve, indicating there was one-to-one correlation between two physical parameters. . Lestriez et al. [107] explained the binding mechanism of CMC in anode electrodes, in which the adsorbed CMC on the carbon particle forms the bridge between the particles, increasing the adhesive strength of the particles. Likewise, in the anode slurry, the adsorption amount of CMC increased with the CMC concentration, and the adsorbed CMC played a role in the adhesion of the graphite particles, inducing an increase in drying stress.

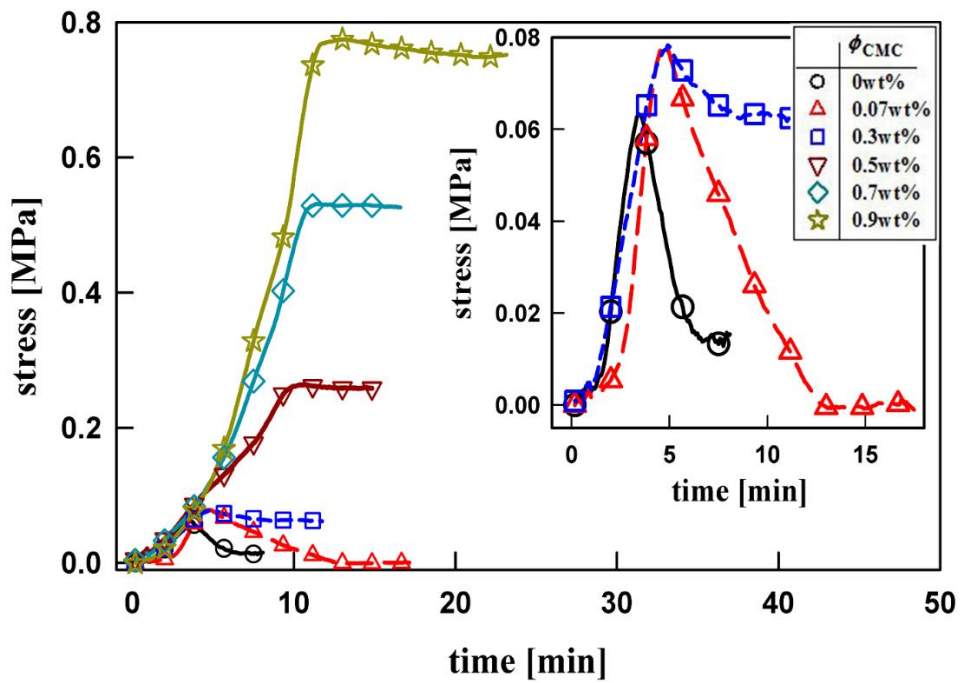


**Figure 4.2.5.** Stress development of graphite slurries containing 50wt% of graphite and various concentration of CMC during drying. Drying temperature is 25 °C and relative humidity is 20 %.



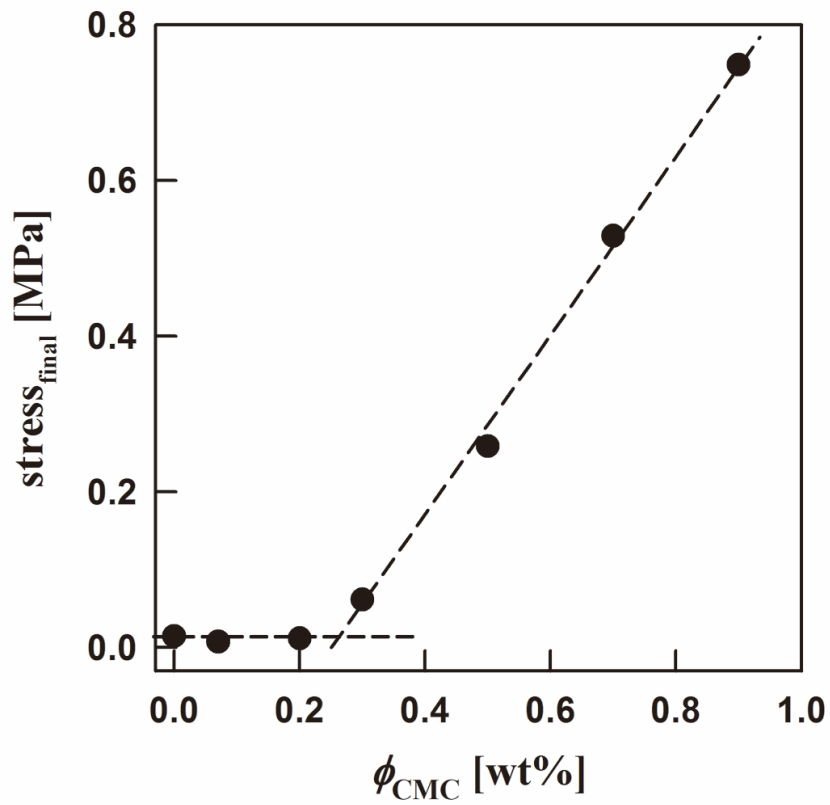


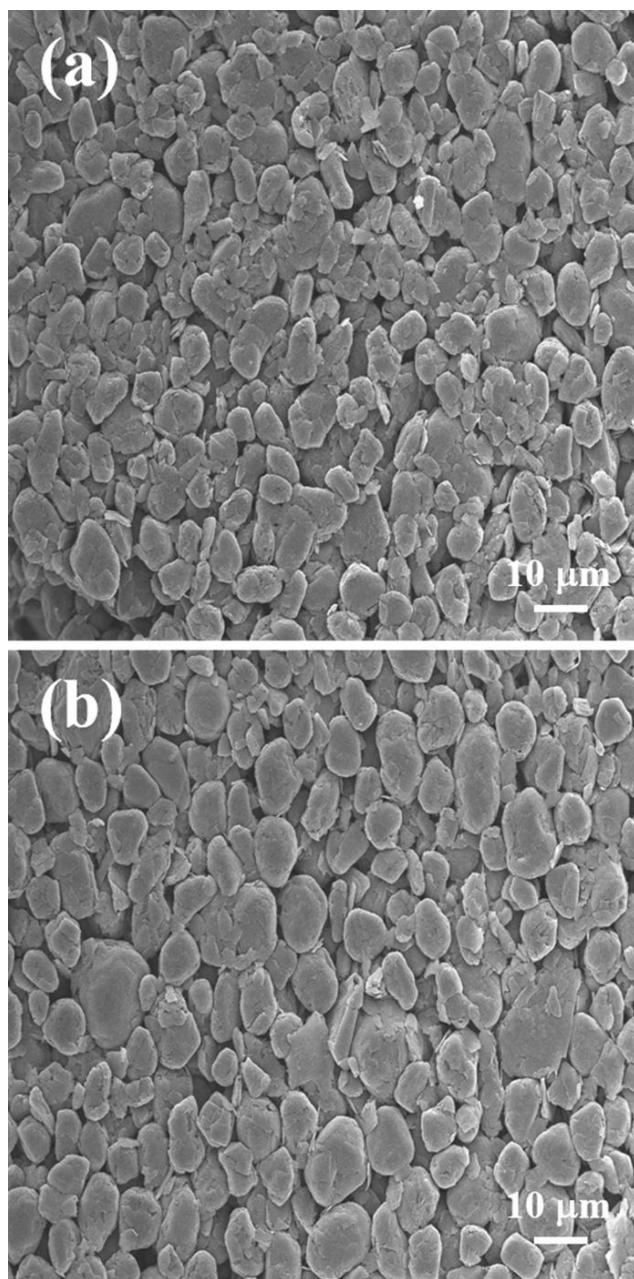
**Figure 4.2.6.** Final stress of battery slurries containing 50wt% of graphite as a function of CMC concentration.

#### 4.2.2.2. Microstructure of film for graphite/CMC slurry

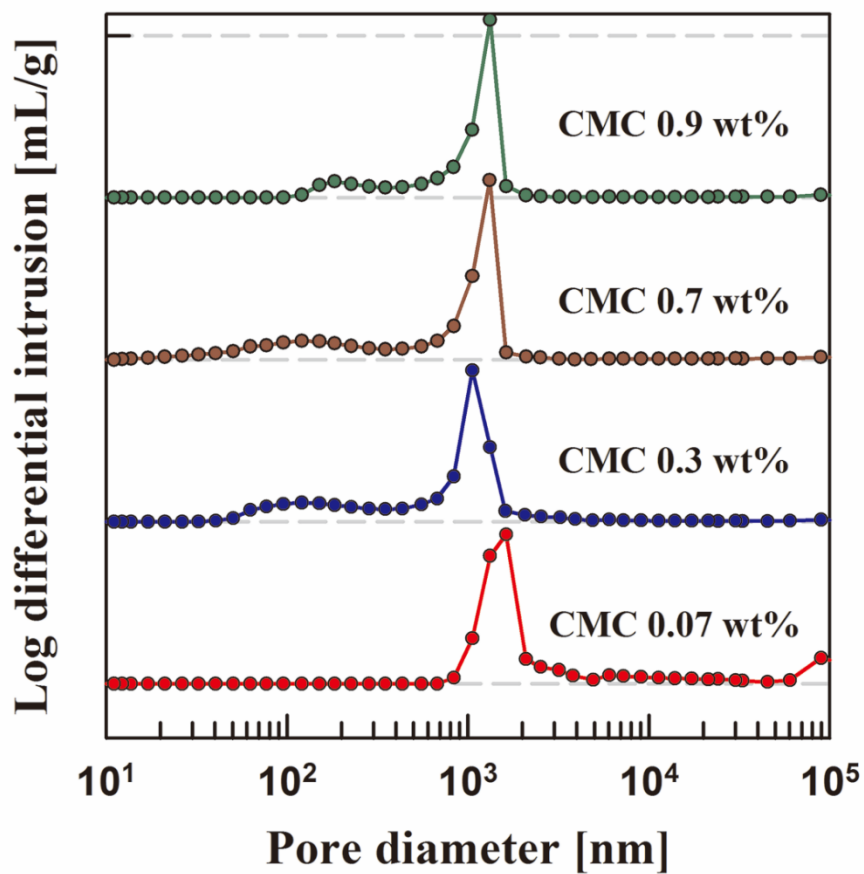
Figure 4.2.7 shows the SEM images of the dried film for graphite slurries containing low and high concentration of CMC. Although the CMC concentration was changed, the change of microstructure according to the CMC concentration was unclear. So, the microstructure of the dried film according to the CMC concentration needs to be analyzed by the pore size distribution.

Figure 4.2.8 shows the pore size distribution in dried film for graphite/CMC slurries according to the CMC concentration. The effect of CMC on the microstructure of the film could be analyzed by both pore size distribution and drying stress. There were large pores with above 1  $\mu\text{m}$  of diameter in the film with 0.07wt% of CMC. On the other hand, when the CMC concentration was increased to above 0.3wt%, the pore size distribution was changed. The pores with 50nm ~ 1 $\mu\text{m}$  of diameter appeared and large pores above 1 $\mu\text{m}$  disappeared when the CMC concentration was increased to above 0.3wt%. Moreover, when the CMC concentration was increased to 0.7wt%, the pore size became smaller even to 10nm of diameter and the pores with 50nm ~ 1 $\mu\text{m}$  diminished simultaneously. When the CMC concentration was further increased to 0.9wt%, the pores of tens of nanometer scale disappeared and there existed pores of hundreds of nanometers in the film. As the concentration of CMC increased, the average pore diameter decreased while the porosity remained unchanged (see Table 4.2.2). The trend of pore size distribution in the film was also similar to the development of drying stress. That is, in the case of the slurry with below 0.27wt% of CMC concentration, there was no residual stress with large pores above a few  $\mu\text{m}$  of diameter.

In the case of the slurry with above 0.27wt% of CMC concentration, on the contrary, the residual stress remained and there were pores with nanometer scales of diameter. The reason why the adhesion strength was changed according to the CMC concentration was considered as the change of pore size and the role of CMC's.



**Figure 4.2.7.** SEM images of the dried film for anode slurries containing 50wt% of graphite and different concentration of CMC: (a) graphite 50wt% + CMC 0.3wt%, (b) graphite 50wt% + CMC 1.7wt%.



**Figure 4.2.8.** Pore size distribution of the dried film containing 50wt% of graphite and various concentration of CMC. The interval in y-axis (horizontal grey dashed line) represents 1.5 mL/g..

**Table 4.2.2.** Average pore diameter and porosity for dried film containing 50wt% of graphite and various concentration of CMC.

Sample ( $\phi_{\text{graphite}}/\phi_{\text{CMC}}$ )	Average pore diameter [nm] <sup>a</sup>	Porosity [%] <sup>b</sup>
50wt% / 0.07wt%	2535.4	44.72
50wt% / 0.3wt%	626.6	43.83
50wt% / 0.7wt%	254.4	49.41
50wt% / 0.9wt%	335.4	48.81

<sup>a</sup> average pore diameter =  $4 \times (V_{\text{tot}}/S_{\text{tot}})$  where  $V_{\text{tot}}$  and  $S_{\text{tot}}$  are the total volume of intruded mercury and the total area of pore surface, respectively [106].

<sup>b</sup> porosity =  $(V_{\text{pore}}/V_{\text{bulk}}) \times 100$

### **4.2.3. Graphite/CMC/SBR slurry**

#### **4.2.3.1. Drying stress of graphite/CMC/SBR slurry**

Figure 4.2.9 shows the development of drying stress according to both CMC and SBR in the slurries containing graphite, CMC, and SBR. Figure 4.2.9(a) shows the drying stress according to the SBR concentration in the graphite slurry with 0.07wt% of CMC. As mentioned before in graphite/CMC slurry section, in the slurry with 0.07wt% of CMC and without SBR, the drying stress steeply decayed to the stress-free state after reaching the maximum peak. This indicates that 0.07wt% of CMC was not enough to form the film with good mechanical strength. The behavior was not changed even when 1wt% of SBR was added to the slurry. In the graphite slurry with 2wt% of SBR, the drying stress decayed after maximum peak but the residual stress slightly increased to approximately 0.02MPa, implying that the 2wt% increase in SBR led to a slight increase in the mechanical strength of the film. The maximum peaks were similar at approximately 0.08MPa, while the residual stress increased as the SBR concentration increased. Therefore, it can be argued that the maximum stress peak was induced by the graphite particles and the residual stress was induced by SBR. The slurry with low concentration of CMC requires a large amount of SBR to form the film with good mechanical strength.

Figure 4.2.9(b) shows the development of drying stress depending on the SBR concentration in the graphite slurry with 0.3wt% of CMC. The drying stress containing 0.3wt% of CMC decayed slightly after maximum and showed a residual stress of

approximately 0.06MPa although there was no SBR in the slurry. In addition, as the SBR concentration increased up to 2wt%, the trend of stress development was similar, but both maximum peak and residual stress were increased. In other words, in the slurry containing 0.3wt% of CMC, the maximum stress as well as the residual stress increased with the SBR concentration unlike the slurry with 0.07wt% of CMC.

Figure 4.2.9(c) shows the development of drying stress according to the SBR concentration in the slurry with 0.5wt% of CMC. The drying stress developed to a maximum, and maintained the level even though there was no SBR. In addition, the residual stress increased as the SBR concentration increased, similar to what was observed in the case of the slurry containing 0.3wt% of CMC.

The drying stress in the slurry containing 0.9wt% of CMC maintained the maximum stress without relaxation like the slurry containing 0.5wt% of CMC (Figure 4.2.9d). However, the residual stress in the slurry containing 0.9wt% of CMC was the same regardless of the SBR concentration. In the case of the slurry with 0.5wt% of CMC, the SBR helped CMC to enhance the mechanical strength in dried film and the drying stress was increased as the SBR concentration increased. However, in the case of the slurry with 0.9wt% of CMC, there was enough CMC to form the film with good mechanical strength, and the drying stress did not change although the SBR concentration was increased.



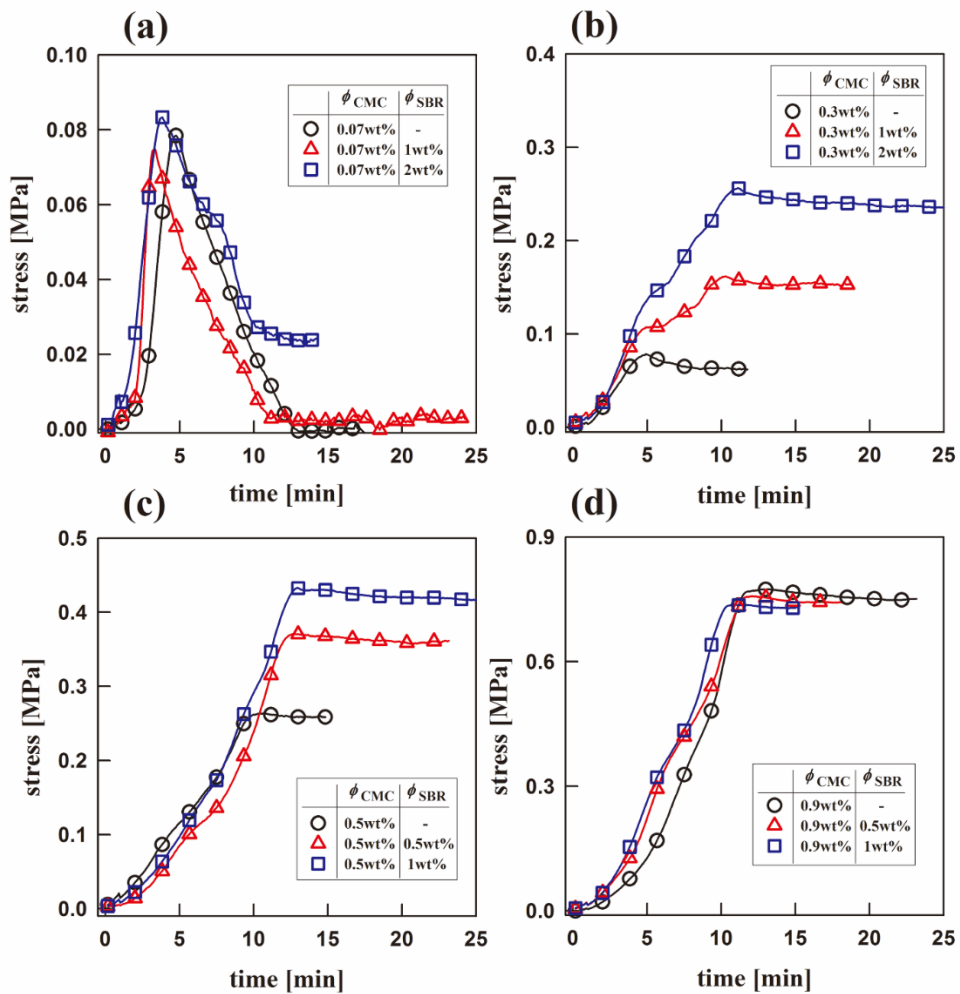


**Figure 4.2.9.** Stress development of graphite slurries containing 50wt% of graphite and various concentration of CMC and SBR during drying. Drying temperature is 25 °C and relative humidity is 20 %.

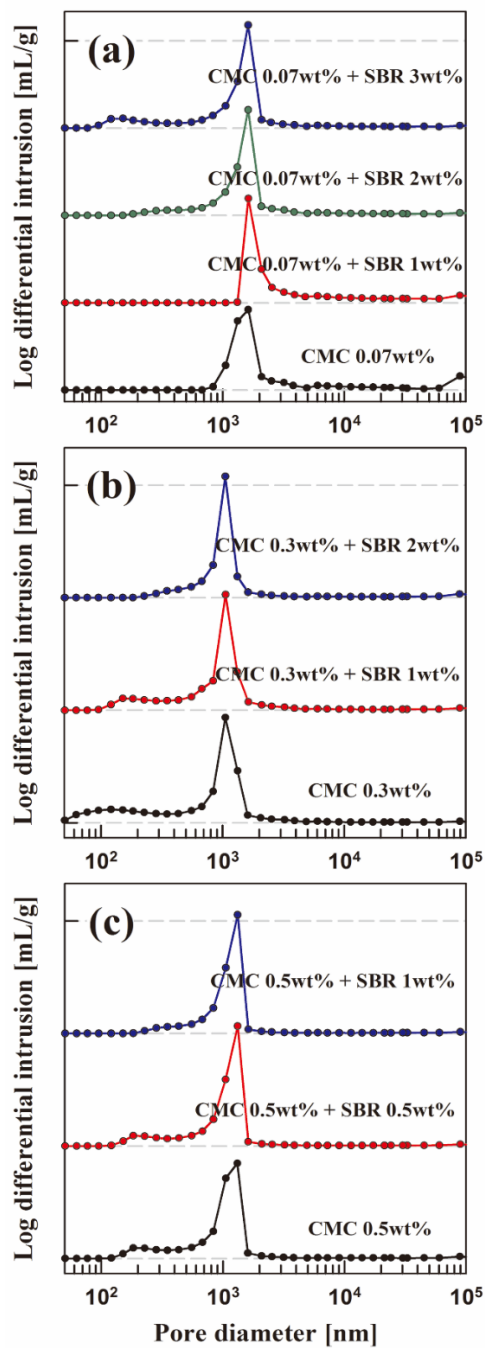
### 4.2.3.2. Microstructure of film for graphite/CMC/SBR slurry

Figure 4.2.10 shows the pore size distribution according to both CMC and SBR concentration. Figure 4.2.10(a) shows the microstructure of the film according to the SBR concentration in the slurry containing 0.07wt% of CMC. The large pores whose diameter was above 1 $\mu$ m existed in the film for the slurry with 0.07wt% of CMC without SBR. The pore size distribution was not changed although 1wt% of SBR was added. As the SBR concentration increased up to 2wt%, the large pores whose size was above 5 $\mu$ m disappeared and the pores with the size above 500nm appeared in the film. As the SBR concentration was further increased to 3wt%, the number of pores with the size of 100nm increased. The trend of pore size distribution was similar to the development of drying stress. In the slurry without SBR and with 1wt% of SBR, the drying stress reached a maximum followed by a relaxation to the stress-free state. As the SBR concentration was increased to 2wt%, the residual stress was also increased. In other words, as the SBR concentration was increased, the SBR filled the pores among the graphite particles. Therefore, the submicron-sized pores disappeared and the pores whose size was in nanometer scale appeared simultaneously. In addition, the filled SBR induced the increase of drying stress.

The microstructure in the film containing 0.3wt% of CMC and various concentration of SBR was different from the slurry containing 0.07wt% of CMC (Figure 4.2.10b). In the case of the slurry with only 0.3wt% of CMC without SBR, there was no submicron-sized pore and there were small pores whose size was above 50nm. As the SBR concentration was increased to 1wt%, a few pores with a few nanometers disappeared

and there were the pores whose size was above 100nm. In addition, as the SBR concentration was further increased to 2wt%, the number of pores with sub-nanometers in diameter was diminished.

In the film with 0.5wt% of CMC, the pores of sub-nanometer scale were diminished as the SBR concentration increased, similar to the film containing 0.3wt% of CMC (Figure 4.2.10c). The trend of pore size distribution was not changed although the CMC concentration increased to 0.9wt% (data not shown here). However, in the case of film containing more than 0.5wt% of CMC, a small amount of SBR was enough to fill the pores among the graphite particles compared to the film containing low concentration of CMC. For example, in the case of the film containing 0.3wt% of CMC, the pores with a few nanometer scale almost disappeared when 2wt% of SBR was present. However, when the CMC concentration increased to 0.5wt%, the similar microstructure was formed by adding only 1wt% of SBR.



**Figure 4.2.10.** Pore size distribution in dried film containing 50wt% of graphite and various concentration of CMC and SBR. Each interval in y-axis (horizontal grey dashed line) represents 1.5 mL/g.

#### 4.2.4. Processing window map for anode slurry

The processing window map was made based on the drying stress, indicating the effect of both CMC and SBR on the mechanical strength of the film. As shown in the right hand side of Figure 4.2.11, in region I, the drying stress developed at the initial stage and the stress relaxed to the stress-free state after the maximum peak. In this region, the film with sufficient mechanical strength could not be generated. Region II belongs to the concentration range of CMC and SBR in which the drying stress relaxed after maximum, but the residual stress was present. For instance, in the case of film with 0.07wt% of CMC, there was no residual stress when the SBR concentration was less than 1wt%, while the residual stress was generated when the SBR concentration increased above 2wt%. However, both CMC and SBR were still not enough to produce the film with good mechanical strength. As the concentration of CMC or SBR increased, the drying stress maintained the maximum stress without relaxation, and this concentration region was defined as region III. In the case of film containing 0.3wt% of CMC, there was residual stress although the SBR did not exist in the film, and the behavior of drying stress was not changed if the SBR concentration was increased to 1wt%. However, when the SBR concentration was increased to 2wt%, the stress maintained the maximum value. In addition, the film containing more than 0.5wt% of CMC did not show any stress relaxation and the stress maintained the maximum value regardless of the SBR concentration, which means the film containing the CMC and SBR in region III had sufficient mechanical strength. Therefore, I confirmed that a large amount of SBR was needed to form the film with sufficient mechanical strength in the

slurry containing low concentration of CMC. On the other hand, in the case of slurry containing above 0.5wt% of CMC, the SBR could not affect the mechanical strength of the film to a significant degree.

In battery industry, the organic materials like CMC and SBR have a negative influence on the battery performance such as a decrease in conductivity. On the other hand, the insufficient organic materials can reduce the electrode performance such as a decrease of film stability and adhesion force. Therefore, the processing window map is expected to be useful in enhancing the slurry performance with a minimal amount of binders.

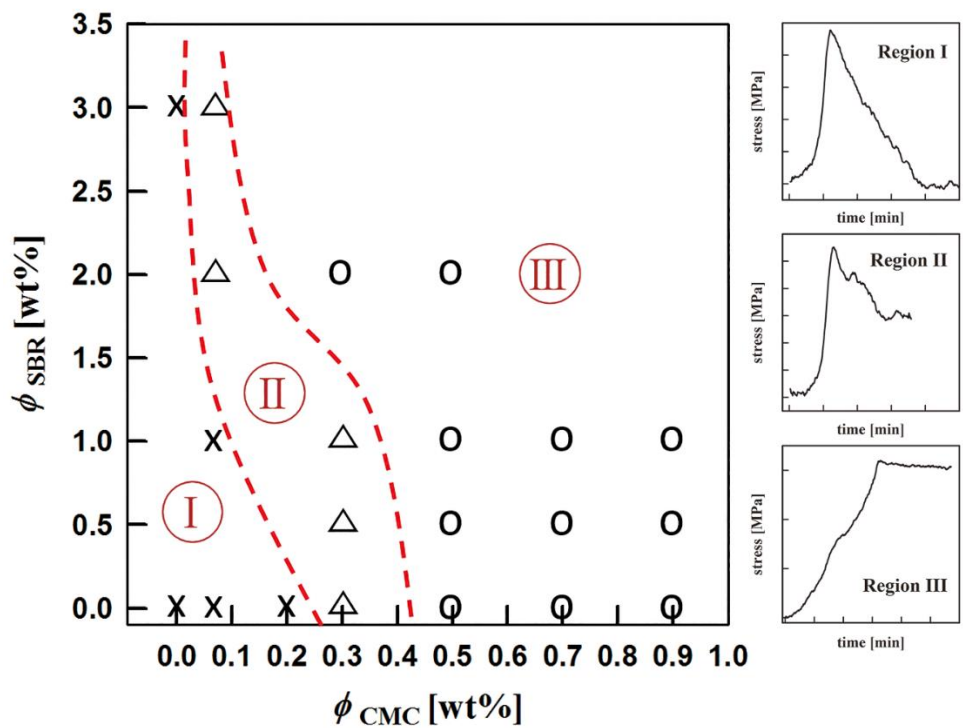


**Figure 4.2.11.** Processing window map for dried film of anode slurry. Symbol X indicates poor mechanical strength,  $\Delta$  indicates less mechanical strength and  $\circ$  indicates good mechanical strength of the film.

## **4.3. Latex migration during drying in anode slurry**

### **4.3.1. Validation of intensity of fluorescent light**

Validation tests were performed to investigate the relation between the intensity of the fluorescent light emitted from the samples and the mass fractions of fluorescent particles in the samples [108]. The tests were performed in a darkroom at room temperature and 29% relative humidity. Figure 4.3.1a indicates the relation between the initial intensity of the fluorescent light and the coating height for various concentrations of latex particles. The intensity of the fluorescent light monotonically increased with coating height at the initial drying stage and also increased more rapidly with increasing latex concentration. The intensity of the fluorescent light emitted for each coating height was normalized using the intensity of fluorescent light emitted from the same height of a coating containing 0.1 wt% latex particles (Figure 4.3.1b). The normalized intensity of fluorescent light showed a power law relation with latex concentration (power law exponent of 0.86), indicating that the present measurements of the intensity of fluorescent light enable us to determine the local concentrations of latex particles in drying films.



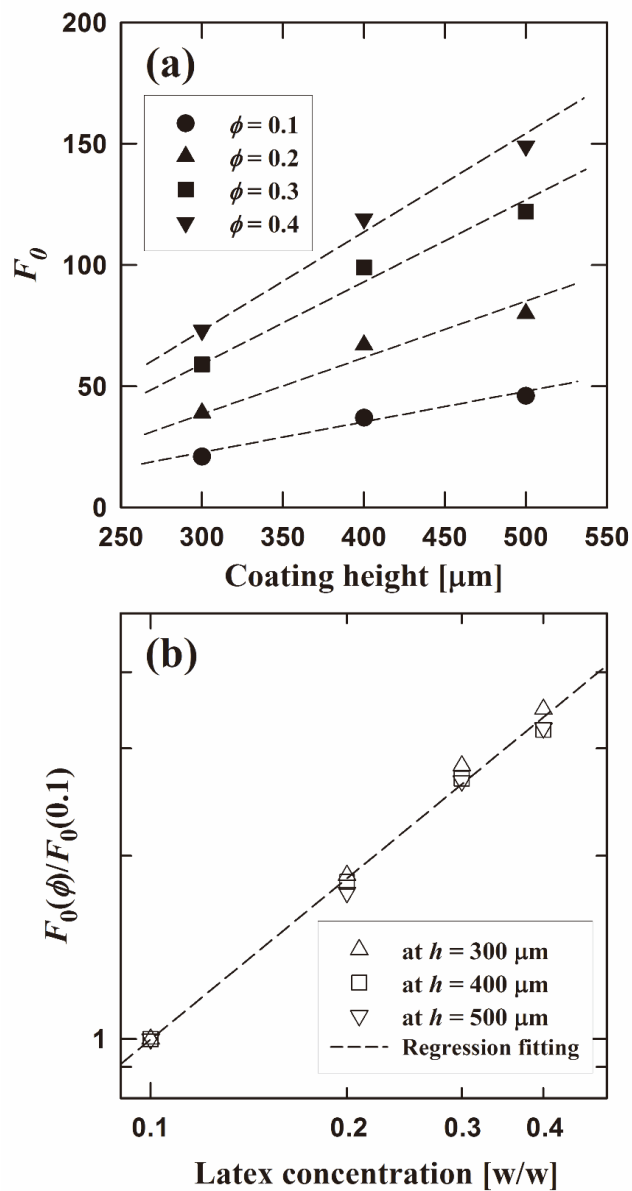


**Figure 4.3.1.** Dependence of intensity of fluorescent light on coating height and concentration of fluorescent particles: (a) intensity of fluorescent light plotted as a function of coating height for various concentrations of latex particles and (b) normalized intensity of fluorescent light plotted as a function of latex concentration for various coating heights.

### 4.3.2. Latex migration in CMC solution

Before I investigated the mechanism of latex migration in graphite slurries, I studied latex migration in a polymer solution containing 0.4 wt% latex particles dried at various drying temperatures. The intensity of the fluorescent light emitted is shown as functions of drying time for CMC concentrations of 0.5 (Figure 4.3.2a) and 1.0 wt% (Figure 4.3.2b). The intensity of the fluorescent light emitted during drying was normalized using the initial fluorescence intensity,  $F_0$ . The drying time was described as dimensionless time,  $t_D = (t_r \cdot E)/H_0$ , where  $t_r$ ,  $E$ , and  $H_0$  denote the drying time, initial film shrinkage rate, and initial coating height, respectively.

The development of the intensity of the fluorescent light showed complex behavior depending on CMC concentration and drying temperature. The intensity of the fluorescent light emitted from the 0.5 wt% CMC solution first decreased toward the minimum value during the initial drying stage (regime I), increased to a maximum (regime II), and eventually decreased dramatically toward the final value during the late drying stage (regime III), as shown in Figure 4.3.2(c). The minimum intensity of fluorescent light decreased with increasing drying temperature, whereas the maximum and final intensities of fluorescent light increased. The transition from regime II to III was found to shift to a longer drying time as the drying temperature increased.

For the 1.0 wt% CMC solution, on the other hand, the intensity of the fluorescent light emitted from the solution dried at 30°C remained constant until it finally decreased below unity. In addition, the maximum and final intensities of fluorescent light were independent of drying temperature at 50 and 70°C.

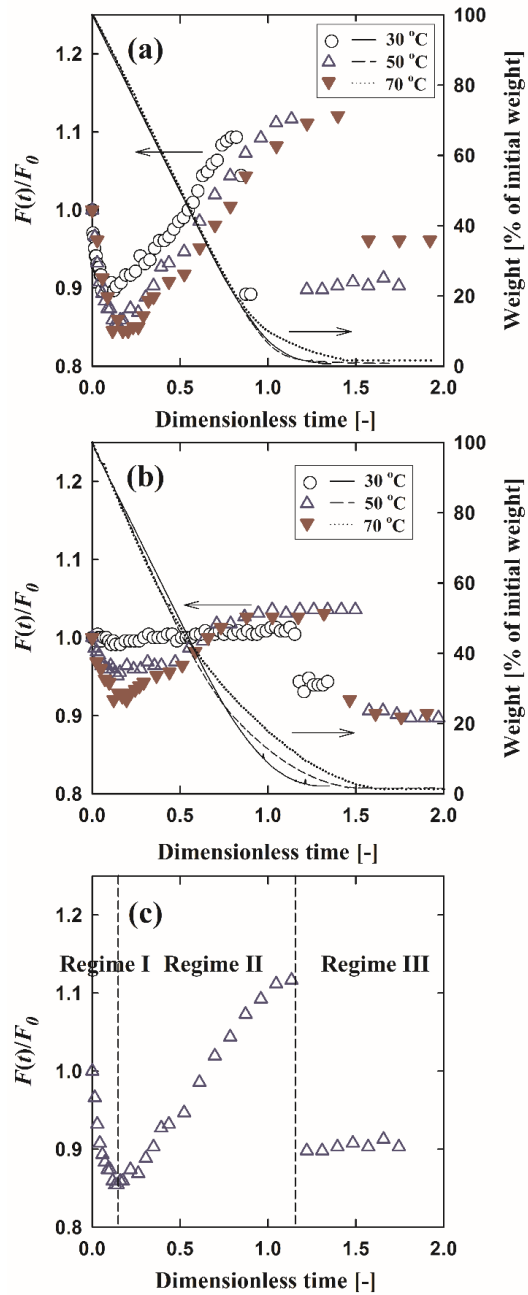


**Figure 4.3.2.** Intensity of fluorescent light developed for latex-CMC suspension dried at various temperatures: (a) 0.5, (b) 1.0 wt% CMC solution and (c) divided regimes depending on the development of intensity of fluorescent light.

The interfacial structure on the suspension surface may affect the concentration-dependent evolutions of fluorescence. To check this, I measured the developments of the beam spot reflected from the air-liquid interface at 30 °C for coatings of 0.5 (Figure 4.3.3) and 1.0 wt% CMC (Figure 4.3.4). The profile of the beam spot was elliptical during initial drying but became more scattered during drying. I monitored the vertical and horizontal widths of the beam spot, corresponding to the parallel and perpendicular directions of laser reflection, respectively. Both the vertical and horizontal widths of the beam spot decreased during initial drying (a→b in Figure 4.3.3). The horizontal width of the beam spot then increased (b→c in Figure 4.3.3), whereas the vertical width of the beam spot slightly increased during drying, indicating an anisotropic beam profile. As drying progressed further, both the vertical and horizontal widths of the scattered beam drastically increased at  $t_D \approx 0.9$  (c→d in Figure 4.3.3) and eventually reached a constant. Interestingly,  $t_D$  is consistent with the time at which I observed the transition between regimes II and III in FM. In contrast, the beam spots obtained for the 1.0 wt% CMC solution maintained their shape and size (a→b in Figure 4.3.4) and then gradually increased (b→c→d in Figure 4.3.4), showing a different development in the size of the beam spot depending on the concentration of CMC.

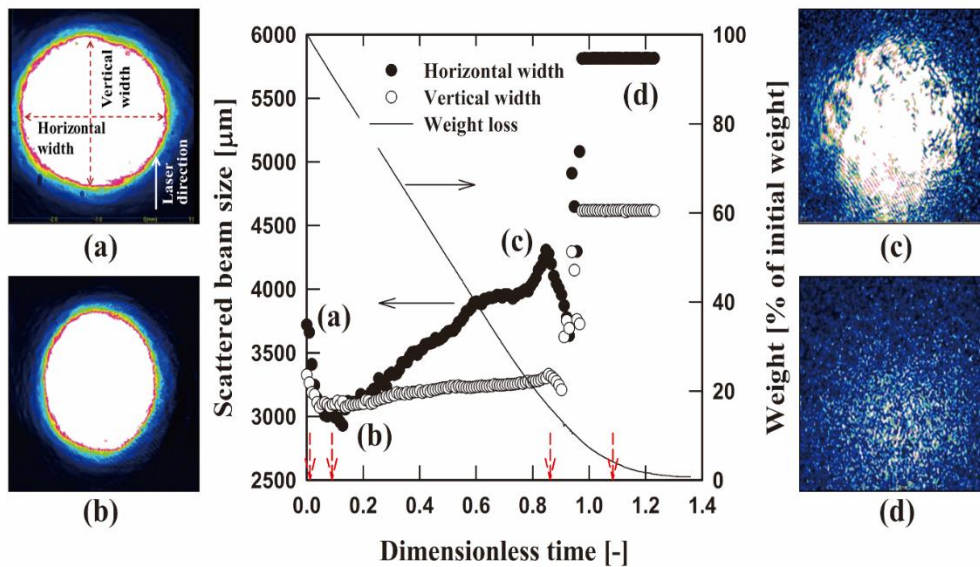


**Figure 4.3.3.** Development of beam spot during drying of 0.5 wt% CMC solution: (a) at initial drying, (b) at minimum size of beam spot, (c) at end of constant rate period, and (d) during final drying.

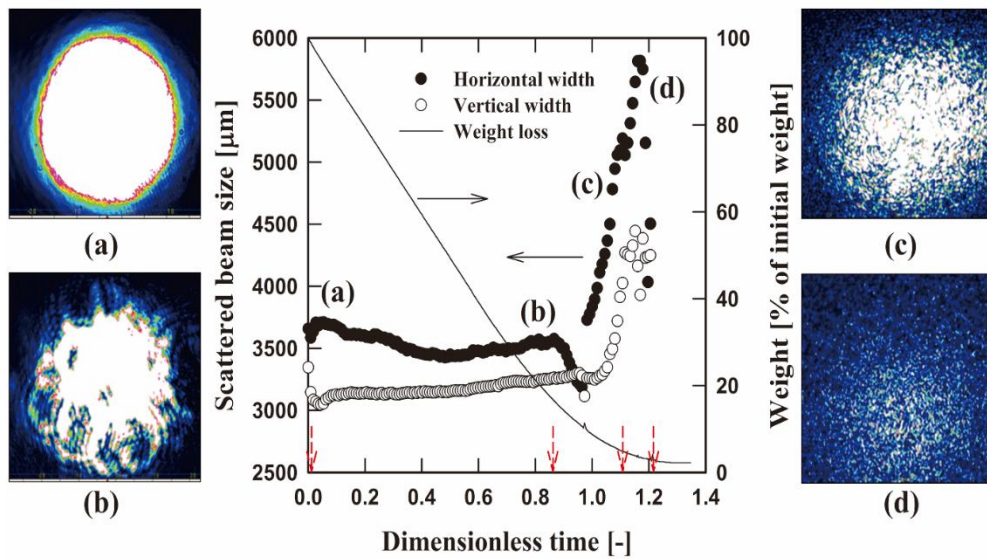


**Figure 4.3.4.** Development of beam spot during drying of 1.0 wt% CMC solution: (a) at initial drying, (b) at end of constant rate period, (c) during falling rate period, and (d) during final drying.

### 4.3.2.1. Evolution in particle consolidation layer

As mentioned in previous chapter, the drying stages could be subdivided into three regimes on the basis of the development of the intensity of the fluorescent light emitted from the sample and from the size of the beam spot. In this section, the time evolution of the intensity of the fluorescent light is discussed in the light of the migration and packing of latex particles in the vicinity of the air-liquid interface.

First, let us consider the variation in the refractive indices of the suspensions. The refractive indices of air ( $n_{\text{air}}$ ), water ( $n_{\text{water}}$ ), and polystyrene ( $n_{\text{PS}}$ ) are 1.00026 [109], 1.33585 [110], and 1.59861 [111], respectively. The latex particles were well dispersed throughout the medium during initial drying. As water evaporated during drying, the latex particles are diffused toward the top surface of the coating and became closer to each other, leading to an increase in the refractive index of suspension. According to Snell's law, this leads to a decrease in the refraction angle at the free surface. These facts are consistent with our simultaneous fluorescence/beam-size measurements in drying regime I in which the size of the reflected beam spot decreased to a minimum, indicating that initial particle packing proceeds in this regime.

In regime II, the latex particles subsequently formed a consolidation layer at the top surface of the coating. The lower liquid pressure beneath the curved meniscus in the consolidation layer initiated capillary pressure-induced flow, which, in turn, accumulated the particles beneath the layer. As the consolidation layer thickened, the consolidating particles emitted more fluorescent light, thereby overcoming the decrease in the intensity of the fluorescent light owing to the variation in the refractive index.

This finding is consistent with the increase in the intensity of the fluorescent light emitted from the suspension containing higher concentrations of latex particles, as shown in Figure 4.3.1.

The formation of a consolidation layer on top of the coating can be explained in terms of the dimensionless Peclet number ( $Pe$ ) and the sedimentation number ( $N_s$ ), which represent the balance among the evaporation, diffusion, and sedimentation of particles [33,89]. The dimensionless Peclet number is defined as

$$Pe = (E \cdot H_0) / D_0, \quad (4.3.1)$$

where  $E$  is the evaporation rate of the solvent,  $H_0$  is the initial coating height, and  $D_0$  is the Stokes-Einstein diffusion coefficient, which is defined as

$$D_0 = kT / 6\pi\mu R, \quad (4.3.2)$$

where  $k$  is the Boltzmann constant,  $T$  is the drying temperature,  $\mu$  is the viscosity of the medium, and  $R$  is the radius of the particle. The Peclet number represents a balance between the evaporation and diffusion of particles in the medium.

The sedimentation number can be defined to describe the balance between sedimentation and evaporation as

$$N_s = U_0 / E, \quad (4.3.3)$$

where  $U_0$  is the Stokes' settling velocity, which is given as

$$U_0 = 2R^2g(\rho_P - \rho_L)/9\mu, \quad (4.3.4)$$



where  $g$  is the gravitational acceleration,  $\rho_P - \rho_L$  is the difference between the particle density ( $\rho_P$ ) and the density of the dilute solution ( $\rho_L$ ), and  $\mu$  is the viscosity of the polymer solution.

Evaporation is dominant, and a discontinuous particle distribution forms in films for which  $Pe \gg 1$  [33,89,90]. In contrast, a homogeneous particle distribution evolves under a diffusion dominant condition of  $Pe \ll 1$ . In addition, when  $N_s \ll 1$ , the sedimentation does not occur. The particle distributions in water [89] and in the polymer solution [33] during drying have previously been predicted based on dimensionless numbers such as  $Pe$  and  $N_s$ . When the latex suspension composed of 0.5wt% CMC was dried at 30°C, the estimated Peclet and sedimentation numbers were  $4.05 \times 10^3$  and  $5.88 \times 10^{-6}$ , respectively (Table 4.3.1). The results modeled by Buss et al. [33] revealed that the critical Peclet number, at which the evaporation- and diffusion-dominant regions can be separated, is approximately  $Pe_c = 0.63$  for a suspension containing 10vol% of particles and 1 vol% of polymer, suggesting that a consolidation layer forms early during drying under the present conditions of  $Pe \gg Pe_c$  and  $N_s \ll 1$ . In addition, our preliminary numerical simulation based on the previous model by Cardinal et al. [89] demonstrated that a consolidation layer formed during initial drying (not shown here), although I simply ignored the polymer effect that occurred during drying because of the lack of information on the diffusion coefficient of CMC.

Further evidence as to the formation of a consolidation layer is also supplied by our beam spot measurements. When a laser beam was irradiated into a consolidation layer, the beam was diffracted or even scattered by closely packed particles and showed a broader spot as the layer thickened during evaporation. This finding is consistent with

our observation that the beam reflected from the coating surface exhibited an increase in its spot size as the drying proceeded in regime II (b→c in Figure 4.3.3). It is worth noting that the consolidation layer in this regime was saturated with water so that the mass-loss curves exhibited a constant slope (Figure 4.3.2a).

As water further evaporated, the air-water interface began to recede toward the bottom of the surface, and the consolidation layer protruded above the air-water interface [48]. This stage, defined as regime III in this study, is usually referred to as a falling rate period, in which the rate of solvent loss begins to decrease beyond the end of the constant rate period. The protruded consolidation layer gives rise to an increase in the amount of emitted lights scattered due to invaded air into the voids among particles. Indeed, our beam profile measurements revealed that the elliptic reflected beam began to collapse because of strong beam scattering and showed a drastic increase in beam spot size at the onset of the falling rate period (c→d in Figure 4.3.3). As a result, the intensity of the fluorescent light emitted from the suspension suddenly decreased to the final intensity (Figure 4.3.2a). These findings strongly suggest that the consolidation layer on the top surface protruded into the air as the air-water interface receded and that the air invaded into the pores among the particles, replacing water during the falling rate period.

**Table 4.3.1.** Constants and dimensionless numbers for latex particles in 0.5 wt% CMC solution.

<b>Drying Temperature</b>	$\mu$ (Pa·s)	$E$ (m/s)	$D_0$ (m <sup>2</sup> /s)	$U_0$ (m/s)	$Pe$	$N_s$
<b>30°C</b>	0.31	$1.14 \times 10^{-7}$	$1.41 \times 10^{-14}$	$6.69 \times 10^{-13}$	$4.05 \times 10^3$	$5.88 \times 10^{-6}$
<b>70°C</b>	0.09	$7.28 \times 10^{-7}$	$5.24 \times 10^{-14}$	$2.20 \times 10^{-12}$	$6.94 \times 10^3$	$3.02 \times 10^{-6}$

### 4.3.2.2. Suppressed migration in dense CMC solution

To address the suppressed latex migration, I next focused on entanglements of CMC chains. CMC molecules form a polymeric network and show a gel-like behavior when they are above a critical concentration [112]. Furthermore, CMC tends to form different molecular conformations such as extended chains, coiled chains, and gels, depending on CMC concentration [17]. In the dilute regime, CMC is freely dispersed throughout the medium below  $c^*$ . As the concentration of CMC increases above the overlap concentration,  $c^*$ , the polymer chains begin to overlap. The  $c^*$  was determined from the inverse of the intrinsic viscosity, *i.e.*,  $c^* \approx 1/[\eta]$ . I estimated the intrinsic viscosity of CMC solution not only experimentally using the Huggins (Eq. 4.3.5) [113] and Kraemer equations (Eq. 4.3.6) [114] but also theoretically using the Mark-Houwink equation:

$$\eta_{sp} / c = [\eta] + k_H[\eta]^2c, \quad (4.3.5)$$

$$(\ln \eta_{rel}) / c = [\eta] - k_K[\eta]^2c, \quad (4.3.6)$$

where  $\eta_{sp}$  is the specific viscosity ( $= \eta/\eta_0 - 1$ ),  $\eta_{rel}$  is the relative viscosity ( $= \eta/\eta_0$ ),  $c$  is the concentration of polymer, and  $k_H$  and  $k_K$  are the Huggins and Kraemer constants, respectively.

Fitting the viscosity measurements gave  $[\eta] = 74.94$  dl/g, determined as the  $y$ -intercept of both the Huggins (open circle) and Kraemer (closed circle) relation, where  $k_H$  and  $k_K$  are  $1.317 \times 10^{-1}$  and  $4.004 \times 10^{-2}$ , respectively (Figure 4.3.5a).

In addition, the intrinsic viscosity of CMC was determined as 49.84 dl/g from the Mark-Houwink equation:

$$[\eta] = KM^a, \quad (4.3.7)$$

where  $K$  was the Mark-Houwink constant ( $0.1 \times 10^{-5}$  dl/g) and the exponent,  $a$ , was 1.4 (for an aqueous 0.001 M NaCl) [115].

The intrinsic viscosity (49.84 dl/g) obtained using the Mark-Houwink equation was slightly different from the experimentally obtained one (74.94 dl/g) because it was difficult to accurately measure the viscosity of low concentrations of CMC with a rotational rheometer. From the values of intrinsic viscosity,  $c^*$  was estimated in the range 0.013–0.02 g/dl.

As the concentration of CMC increased, the configuration of CMC is changed. Figure 4.3.5b shows the specific viscosity of CMC solution depending on the CMC concentration. The specific viscosity is defined as  $\eta_{sp} = (\eta - \eta_s) / \eta_s$ , where  $\eta$  is the zero shear viscosity of CMC solution and  $\eta_s$  is the viscosity of the solvent. The specific viscosity increased as the concentration of CMC increased. It showed a power law behavior with the concentration of CMC,  $\eta_{sp} \sim c^v$ , and three transition concentration thresholds of CMC could be defined. (1) For  $c^* < c < c_e$ , the CMC molecules which exist freely in dilute regime begin to overlap, and it is defined as the semidilute unentangled regime. In this regime, the specific viscosity follows the Fuoss law,  $\eta_{sp} \sim c^{1/2}$  [14-17]. In addition, the overlap concentration,  $c^*$ , is approximately 0.02wt% which is similar with the value obtained from the intrinsic viscosity. (2) For  $c_e < c < c_D$ , the CMC molecules form entanglements, and it is defined as the semidilute entangled

regime. In this regime, the specific viscosity follows  $\eta_{sp} \sim c^{3/2}$  [14-17]. (3) For  $c_D < c$ , it is defined as the concentrated regime and the specific viscosity follows  $\eta_{sp} \sim c^{3.75-5.5}$  [15-17]. In the concentrated regime, the molecules are more densely entangled and interpenetrated [116]. As shown in Figure 4.3.5b, the power index of the specific viscosity was obtained as  $v \sim 1.8, 0.6, 1.6,$  and  $4.27$  at each regime, respectively. These values were similar to the predictions obtained by the scaling theory in previous researches. In addition, the transition concentration thresholds were obtained as  $c^* \sim 0.02\text{wt}\%$ ,  $c_e \sim 0.1\text{wt}\%$ , and  $c_D \sim 0.56\text{wt}\%$  of CMC. Therefore, the migration of latex particles in the  $1.0\text{wt}\%$  CMC solution was significantly suppressed because the CMC molecules were densely entangled in the concentrated regime.

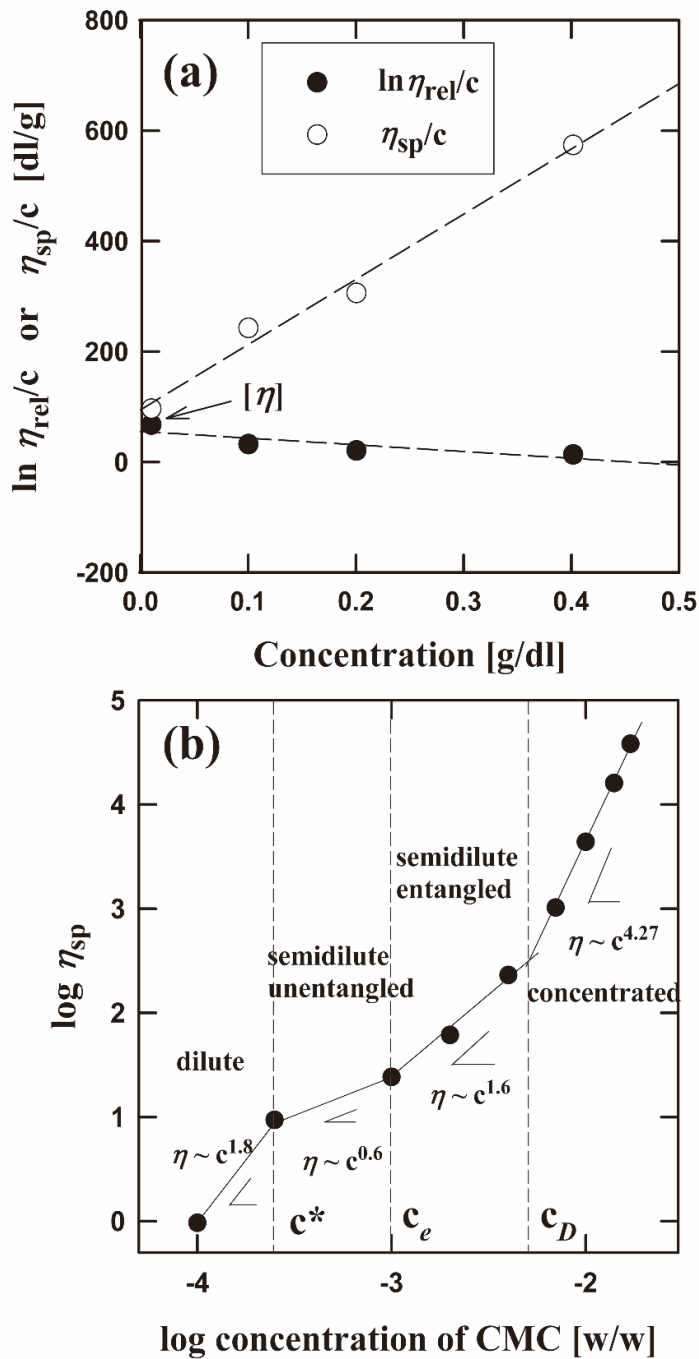


**Figure 4.3.5.** (a)  $\ln \eta_{rel}/c$  and  $\eta_{sp}/c$  plotted as functions of CMC concentration. (b) log-log plot of specific viscosity plotted as function of CMC concentration.

This finding is consistent with our observation that the intensity of the fluorescent light (Figure 4.3.2b) and the size of beam spot (Figure 4.3.4) for suspension containing the high concentration (1.0wt%) of CMC were independent of dimensionless time at drying temperature of 30°C. Indeed, there have been some previous reports that migration of latex particles was suppressed by water-soluble polymers such as CMC [21,117] and starch [118]. According to the reports, the migration of latex particles was inhibited either by the bridging structure between the latex and pigment particles or by the network structure of the polymers. In addition, it became more difficult for water molecules to penetrate into the three dimensional network of CMC because of the high density of CMC chains [119]. Therefore, the latex particles were trapped, retaining their distribution in the entanglements as water evaporated and the coating shrank, and the well-packed distribution of the latex particles was finally formed in the coating.

As a result, the microstructure of the latex in the coating for two different CMC concentrations can be inferred by the development of the intensity of the fluorescent light emitted from the suspension and from the sizes of the beam spots. The latex particles were well dispersed throughout the CMC solution during initial drying regardless of the CMC concentration (Regime I). However, the “top-down” consolidation appeared in the solution containing a low concentration of CMC, in which the consolidated layer of latex particles at the top coexisted with the dispersed particles beneath the layer in the coating (Regime II) followed by the invasion of the air-liquid interface into the coating (Regime III). The motion of the latex particles in the solution containing a high concentration of CMC, on the other hand, was hindered by the entanglement of the CMC. Therefore, non-uniform distribution of latex particles in the



film would be expected to form for low concentrations of CMC, while uniform distribution of latex particles would be expected to form for high concentrations of CMC.

Not only the CMC concentration but also the drying temperature affected the migration of latex particles during drying. The Stokes-Einstein diffusion coefficient,  $D_0$ , increased with increasing drying temperature because of the decrease in the viscosity of the polymer solution. Although  $D_0$  increased with increasing drying temperature,  $Pe$  increased because the extent of the increase in the evaporation rate was larger than that of the increase in the diffusion coefficient. In addition, the sedimentation number,  $N_s$ , decreased with increasing drying temperature (Table 4.3.1). Therefore, the migration of latex particles was enhanced by high  $Pe$  and low  $N_s$  at high drying temperatures, which is consistent with the increase in the maximum and final intensities of fluorescent light emitted from the suspension containing a low concentration of CMC as increasing drying temperature (Figure 4.3.2a).

### 4.3.3. Latex migration in anode slurry

To elucidate how fluorescence changes by adding graphite particles to the latex-CMC suspension, I conducted drying experiments for graphite slurries containing various concentrations of graphite and CMC and at various drying temperatures. Figure 4.3.6 indicates the fluorescence developments for 1 and 5wt% graphite slurries containing 0.4wt% latex particles and 0.7wt% CMC, compared with the graphite-free system at 70 °C. When 1wt% graphite was added to the suspension, intensity of the fluorescent light first decreased during initial drying similar to graphite-free systems and then increased to a great extent at approximately 0.25 of dimensionless time followed by a second similar increase in intensity up to  $F/F_0 \approx 3.5$  when the normalized time is 1.5. However, the intensity of the fluorescent light emitted from the 5wt% graphite slurry decreased and followed the behavior of graphite-free solutions until the dimensionless drying time of  $t_D = 1.4$ , where the fluorescence showed a weak peak. And then, the intensity of the fluorescent light emitted from the 5wt% graphite slurry then gradually decreased. To understand the different trends in the intensity of the fluorescent light depending on the concentration of graphite, I directly visualized segregation of latex particles on the surface of the dried coating. Figures 4.3.7a–c and 4.3.7d–f indicate the images for 1 and 5wt% graphite slurries, respectively, under the same drying conditions as the slurries shown in Figure 4.3.6. Because latex particles emit a weak fluorescence under the light for optical microscopy, the bright domains in Figure 4.3.7a represent the segregated latex particles distinguishable from optically dark graphite layers. As shown in the optical microscope and atomic force microscope

images, the segregated latex particles appeared on the surface of 1wt% graphite slurry (Figures 4.3.7a & b), while there was no distinct segregation of latex particles on the surface of 5wt% graphite slurry (Figures 4.3.7d & e). In addition, cross-sectional imaging revealed that the latex particles had segregated above the graphite consolidation layer for the 1wt% graphite slurry (Figure 4.3.7c), while they seemed to be well-dispersed among the graphite particles for the 5wt% graphite slurry (Figure 4.3.7f). Although the optical and atomic force microscopy images were not taken at the same position of the samples, different regions of each surface were imaged to ensure that a representative image was obtained.

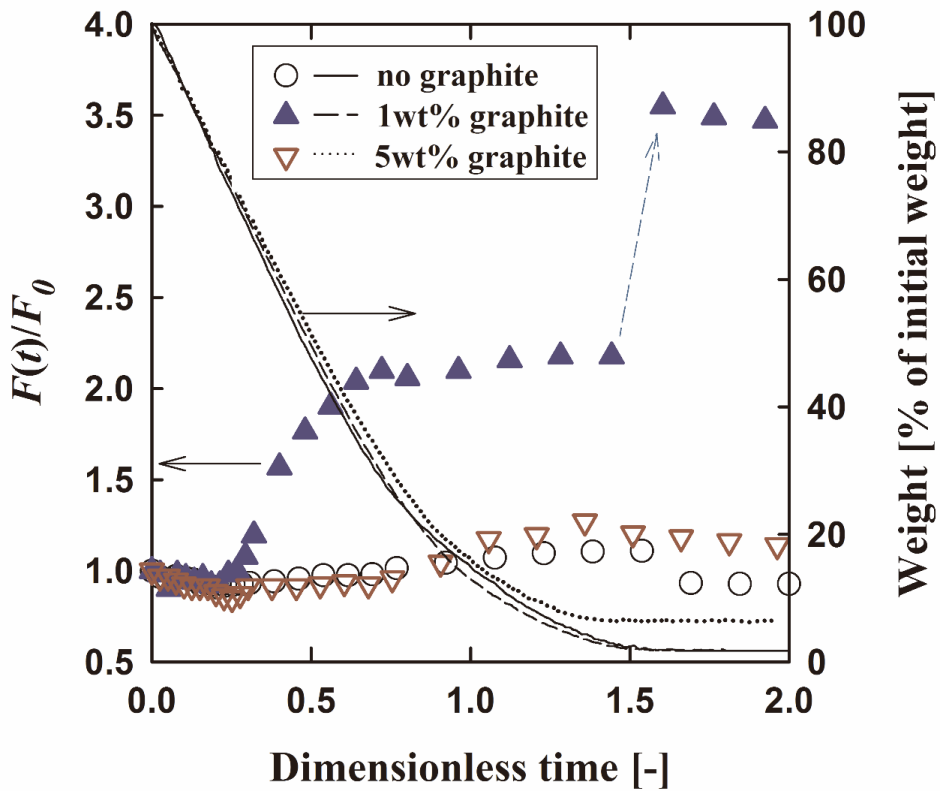


**Figure 4.3.6.** Development of intensity of fluorescent light emitted from graphite slurries at 70°C.

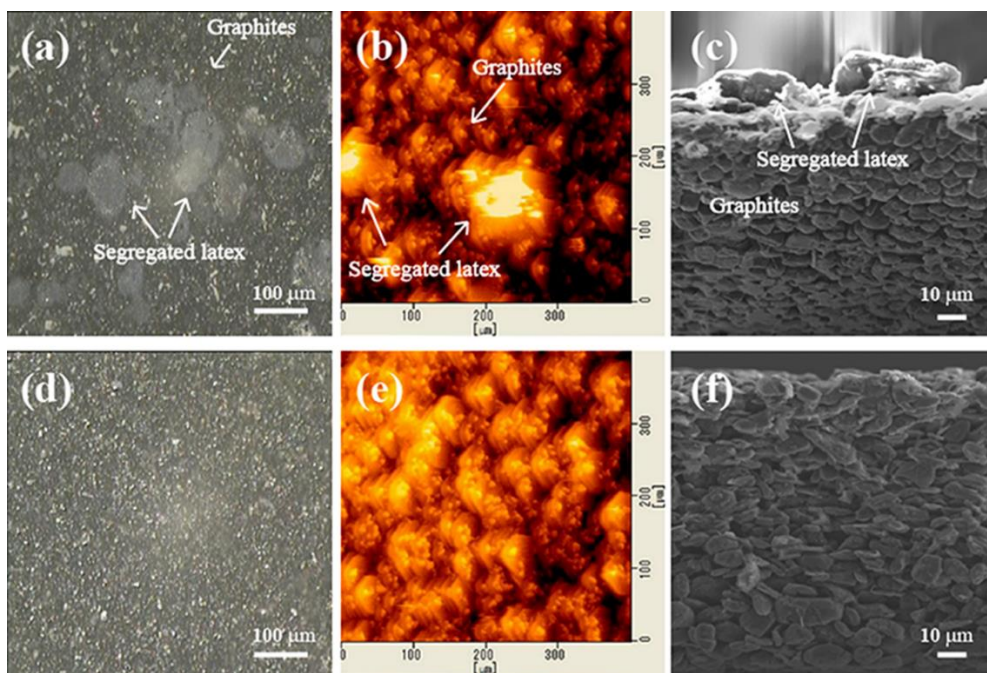


**Figure 4.3.7.** Images for 1 (a)–(c), and 5 wt% (d)–(f) graphite slurries: (a) and (d) are coating surfaces observed using optical microscope, (b) and (e) are coating surfaces observed using atomic force microscope, and (c) and (f) are cross-sections observed using SEM.

In the second series of experiments, the CMC concentration and drying temperature were varied, while the graphite concentration was maintained at 5wt% (Figure 4.3.8). The intensity of the fluorescent light emitted from the slurry dried at a low drying temperature of 30°C remained constant at approximately unity during initial drying (Figure 4.3.8a), whereas it slightly increased with time at higher CMC concentrations (Figure 4.3.8b). On the contrary, the intensity of the fluorescent light emitted from the slurry dried at 70°C decreased with time during initial drying at both CMC concentrations, as observed for the graphite-free system. The maximum and final intensities of the fluorescent light emitted from the 0.5wt% CMC slurry increased with increasing drying temperature (Figure 4.3.8a), while those of fluorescent light emitted from the 1.0wt% CMC slurry were independent of drying temperature, showing a similar intensity development as that of the graphite-free system. It is worth noting that the graphite slurries containing 1.0wt% CMC exhibited much smaller variations in the intensity of the fluorescent light emitted than those containing 0.5wt% CMC.

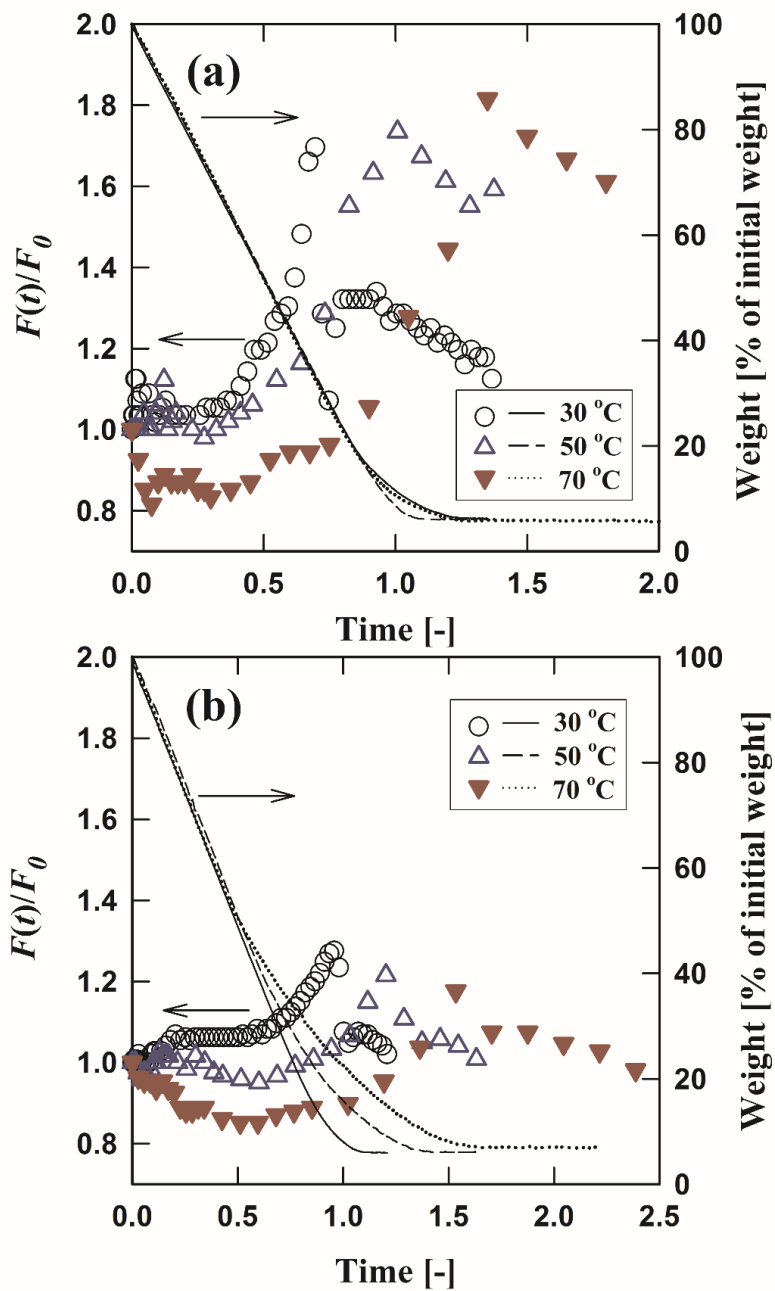


**Figure 4.3.8.** Development of intensity of fluorescent light emitted from 5wt% graphite suspension depending on CMC concentration at various drying temperatures: (a) 0.5 and (b) 1.0wt% CMC.

### 4.3.3.1. Accelerated migration in anode slurry

The bimodal graphite slurries showed different evolutions in the migration of latex particles, *i.e.*, the migration of latex particles was accelerated by the addition of graphite particles (see Figure 4.3.6). Let us consider a particular case in which the graphite and latex particles co-consolidate at the top surface. The smaller latex particles fill in the space among the graphite particles, and capillary-driven convective flow transports latex particles through the pore throat to the evaporating menisci [34]. As drying progresses, the capillary pressure gradient increases and draws more latex particles into the consolidation layer where they become trapped, eventually resulting in a latex-rich zone at the surface. Indeed, the Peclet and sedimentation numbers estimated based on the diameter of graphite particles were  $Pe = 5.62 \times 10^5$  ( $\gg Pe_c$ ) and  $N_s = 6.34 \times 10^{-1}$  for 0.5wt% CMC at drying temperature of 70°C, implying that both graphite and latex particles co-consolidate through evaporation-dominant migration without any gravity-driven settling. Furthermore, I estimated the pore-throat diameter by simply assuming a hexagonal particle packing in which the ratio of the radius of the pore throat to the radius of the particle was about 0.15. The estimated throat diameter was found to be 1.2  $\mu\text{m}$ , big enough to enable the latex particles to pass through the space. However, this physical picture is insufficient to explain why more latex particles migrate at the intermediate graphite concentration of 1wt%. To gain deeper insight, I focused on CMC adsorption onto graphite surfaces and the corresponding variations in the interparticle forces in graphite slurries.



Figure 4.3.9 indicates the isotherms for CMC adsorption onto graphite particles in slurries containing 5 wt% graphite and various concentrations of CMC. The amount of CMC that adsorbed onto the graphite particles increased with increasing CMC concentration and saturated at  $0.9 \text{ mg/m}^2$  above the critical concentration of 0.4 wt%, indicating that CMC had fully covered the graphite surface and that non-adsorbed polymers remained in the medium above the critical CMC/graphite mass ratio,  $r_c = 0.08$ .

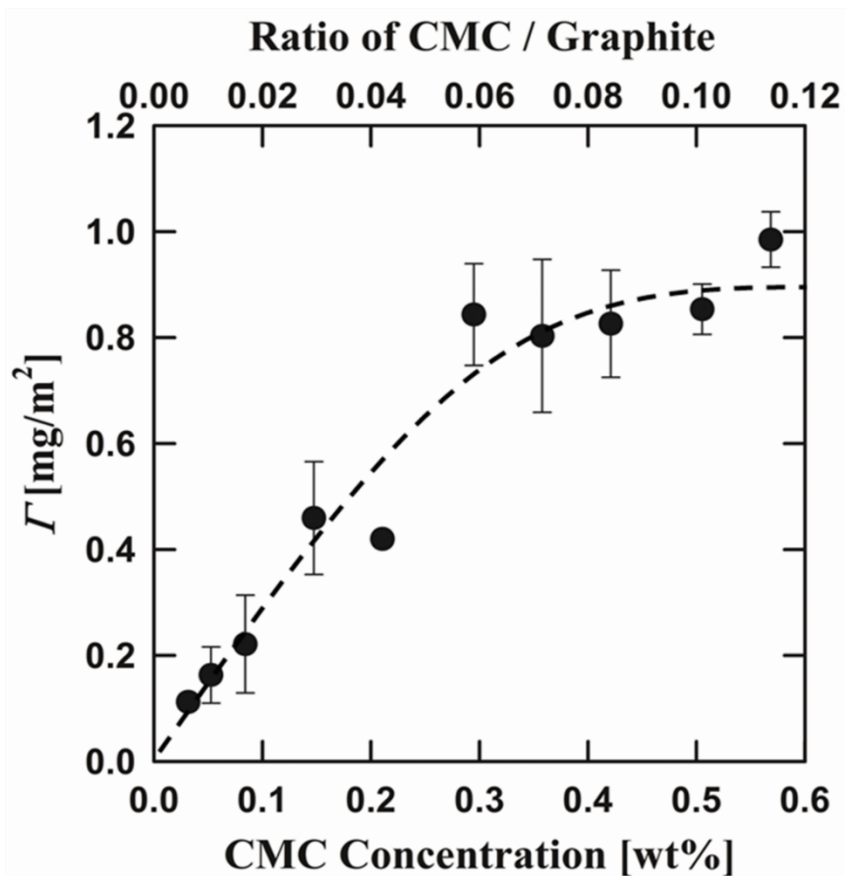


**Figure 4.3.9.** Isotherms for CMC adsorption onto surface of graphite particles, plotted as function of CMC concentration and ratio of CMC/graphite (graphite concentration was 5wt%).

CMC adsorption significantly affects the stability of slurries or suspensions [42,43,120]. Figures 4.3.10(a) and 4.3.10(b) indicate the sedimentation trends for slurries composed of 5wt% graphite and various concentrations of CMC and for those composed of 1wt% graphite and 0.7wt% CMC, respectively.

At low CMC/graphite mass ratios less than  $r_c$ , the graphite particles settled among adsorbing polymers by either gravity or bridging flocculation [121-123]. As the concentration of the polymer increased above  $r_c$ , the polymer fully covered the surfaces of the particles, and the slurry stabilized through steric repulsion (Figure 4.3.10a) [120]. The graphite particles resettled with a further increase in the concentration of the polymer, and the supernatant and graphite particles in the solution containing 1wt% graphite and 0.7wt% CMC (*i.e.*, the solution with a CMC/graphite mass ratio of 0.7) were completely separable (Figure 4.3.10b). A depletion flocculation occurred by non-adsorbed polymer [73-75]. As the particles moved closer to each other, the polymer located among the particles became excluded to the outside of the particles. The resulting difference in the concentration between in the bulk medium and in the overlap region among the particles promoted higher osmotic pressure in the bulk medium than in the overlap region, and induced flocculation of the particles [124]. When the graphite particles were flocculated, the curved menisci between the flocculated particles pulled the fluid to the surface because of capillary force, and, hence, the latex particles could easily migrate through the path between the flocculates toward the free surface, leading to a thicker consolidation layer at the top surface. This finding is consistent with the highest intensity of fluorescent light (Figure 4.3.6) emitted from the suspension and with the segregation of latex particles on top of the graphite consolidation layer (Figure

4.3.7c) for the 1.0wt% graphite slurry containing 0.7wt% CMC. As the water evaporated, the latex particles co-consolidated with the graphite particles and migrated through the pore throats among the graphite particles and toward the coating surface, leading to an increase in the intensity of the fluorescent light emitted. The segregated latex particles protruded into the air and then the curved menisci among the latex and graphite particles pulled the fluid further upward, giving rise to the second increase in the intensity of fluorescent light during late evaporation. This physical picture is consistent with the two-step development in the intensity of the fluorescent light emitted from the slurry (Figure 4.3.6). For the 5wt% graphite slurry whose CMC/graphite mass ratio,  $r = 0.12$ , on the other hand, steric forces among polymers adsorbing onto the surfaces of graphite particles pushed the graphite particles apart producing longer interparticle distances and possibly giving rise to weaker capillary forces and thus less migration of latex particles.

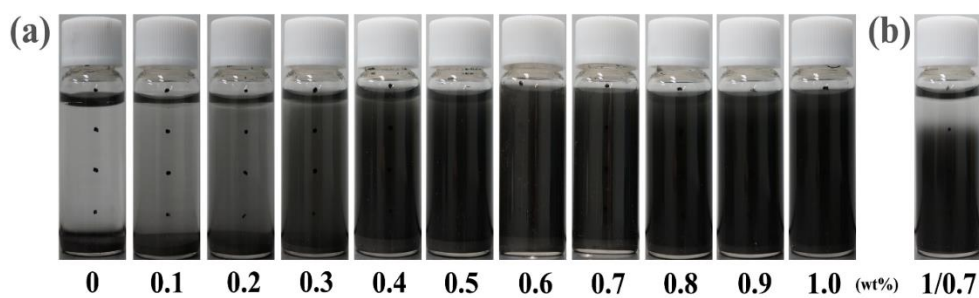


**Figure 4.3.10.** Sedimentation behavior of graphite slurries depending on concentration of CMC. (a) 5wt% graphite slurry (ratio of CMC/graphite varied from 0 to 0.2) and (b) 1wt% graphite slurry containing 0.7wt% CMC (ratio of CMC/graphite is 0.7).

Figure 4.3.11 summarizes the transitions in the minimum, maximum, and final intensities of the fluorescent light emitted from the samples with respect to CMC and graphite concentrations, taking into account the entanglements of neighboring CMC chains and CMC adsorption onto graphite particles.

As shown in Figure 4.3.11a, the minimum intensities of the fluorescent light emitted from the graphite-free suspension remained constant at approximately 0.9 and then increased with increasing concentration of CMC to 1.0wt%. The minimum intensity of fluorescent light indicated the dispersion state of latex particles during initial drying, regime I, before forming a consolidation layer on the top surface of the coating. While the latex particles in the CMC solution containing a low concentration of CMC are diffused toward the air-water interface of the coating, the migration of latex particles was suppressed by CMC entanglement in the solution containing a high concentration of CMC. The distribution of latex particles was almost unchanged so as to show the minimum intensity (i.e., unity) of fluorescent light. The minimum intensity of fluorescent light emitted from the 5wt% graphite slurry, on the other hand, remained constant regardless of the concentration of CMC.

The maximum intensity of fluorescent light emitted from the samples represented the formation of a consolidation layer during drying (Figure 4.3.11b). The intensity of the fluorescent light increased with the accumulation of latex particles in the consolidation layer during the drying stage in regime II. The maximum intensity of the fluorescent light emitted from the graphite-free suspension decreased and remained at unity with increasing CMC concentration. At low CMC concentrations, the latex particles could easily migrate toward the consolidation layer through capillary flow

induced by the consolidated particles. However, as the CMC concentration increased, the migration of latex particles was suppressed by the entanglement of CMC, resulting in an intensity of unity for the fluorescent light emitted from the samples. On the contrary, the maximum intensity of the fluorescent light emitted from the 5wt% graphite slurry was much higher than that emitted from the graphite-free suspension because of the strong capillary effect. The capillary pressure ( $\Delta P$ ) is known to be inversely related to the radius ( $a$ ) of a capillary as  $\Delta P \sim \sigma/a$  where  $\sigma$  is the surface tension. Assuming a Newtonian fluid with a viscosity  $\mu$  flowing in a tube with a length  $L$ , the mean fluid velocity in the tube can be written as  $v \sim \Delta P a^2 / (\mu L)$ , and thus scaled as  $v \sim \sigma a / (\mu L)$ , indicating that the velocity increases with increasing the particle radius. In our bimodal slurries containing graphite and latex particles, small latex particles distribute in a throat between large graphite particles and create capillary pressures as does in latex suspensions. The fluid underneath the throat is pulled toward the free surface with a speed faster than that in latex suspensions because of larger throat, giving rise to a stronger effect of capillary force compared to the suspensions of the smaller latex particles. Therefore, more latex particles could migrate to the consolidation layer in the graphite slurry. In addition, at around the critical ratio of CMC/graphite,  $r_c$ , the graphite particles were well dispersed in the medium because of the steric repulsion induced by adsorbed CMC. As a result, the graphite particles were separated from each other by steric hindrance, and the latex particles could migrate through the space among the graphite particles. However, the migration of latex particles was disturbed by non-adsorbing CMC above  $r_c$ , resulting in a decrease in the maximum intensity of fluorescent light with increasing CMC concentration above  $r_c$ .

The final intensity of the fluorescent light emitted from the samples represented the structure of the dried film (Figure 4.3.11c). The intense fluorescent light emitted from the dried film of 5wt% graphite slurry implied that more latex particles were distributed on top of the surface of the slurry than the dried film of the graphite-free suspensions, showing a trend similar to that of the maximum intensity.



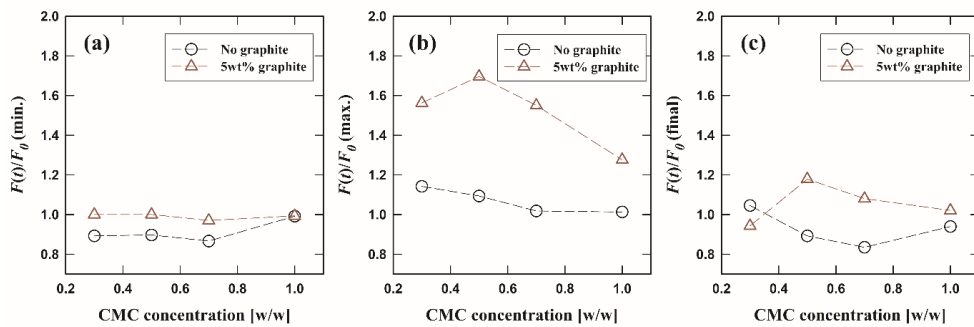


**Figure 4.3.11.** Critical development of intensity of fluorescent light emitted from graphite-free suspension ( $\circ$ ) and 5wt% graphite slurry ( $\Delta$ ) plotted as functions of CMC concentration at 30°C of drying temperature: (a) minimum, (b) maximum, and (c) final intensity of fluorescent light.

# **Chapter 5.**

## **Summary**

In this thesis, the effect of CMC and SBR, which are used as binders in the Li-ion battery anode slurry, on the microstructure formation as well as drying behavior was investigated. In addition, the latex migration in the slurry was studied during drying.

Firstly, the microstructural change depending on the CMC and SBR was investigated. The microstructure of the slurry could be estimated by analyzing the rheological properties of the slurry and it could be confirmed by observation of the cryo-SEM images. The graphite particles formed the gel structure by hydrophobic attraction in the aqueous solution. When the SBR was added to the slurry, the SBR adsorbed on the graphite surface and decreased the attractive force between the graphite particles. In addition, as the concentration of SBR was further increased, the graphite particles could not be aggregated any longer and were well dispersed in the medium, inducing liquid-like behavior of the slurry. The CMC could also adsorb on the graphite surface like SBR. In the case of graphite/CMC slurry, the microstructure of the slurry was changed depending on the concentration of CMC. For the slurry with low concentration of CMC, the graphite particles formed the gel structure by hydrophobic attraction. As the concentration of CMC increased, the adsorption amount of CMC on the graphite surface was also increased. The graphite particles were dispersed by electrostatic repulsion from adsorbed CMC. As the CMC concentration was further increased, the slurry showed a gel behavior again because the CMC molecules form the polymeric network structure at high concentration. The gel structure was formed at low and high CMC concentration, but the structures were different from each other. That is, the gel structure was formed by aggregation of graphite particles at low CMC concentration, while it was formed by polymeric network structure of CMC at high CMC

concentration in the slurry. In the graphite/CMC/SBR slurry, the microstructure of the slurry depended on the concentration of CMC and SBR. For the slurry with low concentration of CMC, the graphite particles could be dispersed by adsorbing SBR on the graphite surface. On the other hand, when the slurry with high CMC concentration, the SBR could not adsorb on the graphite surface due to adsorbed CMC and stayed in the medium. So, the microstructure of the slurry with high CMC concentration was affected only by CMC concentration.

Next, the development of drying stress during drying and the microstructure in the dried film for anode slurry was investigated. The drying mechanism of anode slurry was analyzed by the cantilever deflection method. In the slurry containing only graphite particles, the drying stress developed to a maximum followed by the stress relaxation to the stress-free state. This drying behavior did not change when a small amount of CMC or SBR was added to the slurry. As the concentration of CMC or SBR increased, the residual stress also increased indicating an increase in the mechanical strength of the film. However, excessive amount of organics in the slurry have to be avoided to guarantee the battery performance. Through the processing window map based on the behavior of drying stress, a proper concentration of CMC and SBR to attain the film with good mechanical strength was suggested to support optimizing the slurry design for Li-ion batteries.

It is expected that understanding the mechanism of microstructure formation and the drying behavior according to the binders will help optimizing the design for the Li-ion battery anode slurry.

Finally, migration of latex particles in drying CMC solution and graphite slurries during drying was investigated using FM, enabling us to determine the development of vertical particle distribution in coatings by analyzing the development of the intensity of the fluorescent light emitted from the samples. The development of the intensity of the fluorescent light represented the migration of latex particles during drying. The intensity of the fluorescent light decreased during initial drying, regime I, indicating that the latex particles were dispersed throughout the medium. As the water further evaporated, a consolidation layer was formed on the top surface of the coating, and the latex particles accumulated in that layer through capillary pressure-induced flow, leading to an increase in the intensity of the fluorescent light during this stage, regime II. The intensity of the fluorescent light dramatically decreased because of the strong scattering from the protruded consolidation of latex particles at the onset of the falling rate period in regime III, indicating that the air-water interface invaded into the consolidation layer. The intensity of the fluorescent light was independent for high concentrations of CMC, on the other hand, indicating that the migration of latex particles was suppressed by CMC molecules. The CMC chains showed different states such as dilute, semidilute unentangled, and semidilute entangled in the medium depending on the concentration of CMC with respect to two critical concentrations, overlap and entanglement concentrations. The CMC formed entanglements above the entanglement concentration, so the migration of latex particles was interrupted by CMC chains. Therefore, latex particles were more uniformly distributed throughout films produced with high concentrations of CMC, while it were non-uniformly distributed throughout films produced with low concentrations of CMC.

The CMC chains adsorbed onto the surfaces of the graphite particles, and the microstructures formed from the graphite particles and CMC were dependent upon the amount of adsorbed CMC. The microstructures of the graphite slurry affected the migration of latex particles during drying. The graphite particles aggregated because of depletion attraction by non-adsorbed CMC when the mass ratio of CMC/graphite was large, so there was sufficient space among the aggregation of graphite particles to enable the latex particles to migrate and segregate. When the mass ratio of CMC/graphite was close to  $r_c$ , on the other hand, the graphite particles maintained a stable structure because of steric repulsion, and the latex particles neither migrated nor segregated. This study shows that the migration of latex particles is significantly affected by the microstructures that form in graphite slurries. Thus, the microstructures formed by graphite and CMC in slurries should be studied in more detail to determine the drying mechanism of graphite slurry which shows diverse and complicated film structure.



## References

1. Tarascon, J. -M.; Armand, M. Issues and challenges facing rechargeable lithium batteries. *Nature* **2001**, *15*, 359-367.
2. Alias, N.; Mohamad, A. A. Advances of aqueous rechargeable lithium-ion battery: A review. *J. Power Sources* **2015**, *274*, 237-251.
3. Patil, A.; Patil, V.; Shin, D. W.; Choi, J. -W; Paik, D. -S.; Yoon, S. -J. Issue and challenges facing rechargeable thin film lithium batteries. *Mater. Res. Bull.* **2008**, *43*, 1913-1942.
4. Goodenough, J. B.; Park, K. -S. The Li-ion rechargeable battery: A perspective. *J. Am. Chem. Soc.* **2013**, *135*, 1167-1176.
5. Goriparti, S.; Miele, E.; De Angelis, F.; Di Fabrizio, E.; Zaccaria, R. P.; Capiglia, C. Review on recent progress of nanostructured anode materials for Li-ion batteries. *J. Power Sources* **2014**, *257*, 421-443.
6. Guerfi, A.; Kaneko, M.; Petitclerc, M.; Mori, M.; Zaghbi, K. LiFePO<sub>4</sub> water-soluble binder electrode for Li-ion batteries. *J. Power Sources* **2007**, *163*, 1047-1052.
7. Diftis, N.; Kiosseoglou, V. Improvement of emulsifying properties of soybean protein isolate by conjugation with carboxymethyl cellulose. *Food Chem.* **2003**, *81*, 1-6.
8. Pensini, E.; Yip, C. M.; O'Carroll, D.; Sleep, B. E. Carboxymethyl cellulose binding to mineral substrates: Characterization by atomic force microscopy-



- based Force spectroscopy and quartz-crystal microbalance with dissipation monitoring. *J. Colloid Interface Sci.* **2013**, *402*, 58-67.
9. Liu, Q.; Zhang, Y.; Laskowski, J. S. The adsorption of polysaccharides onto mineral surfaces: an acid/base interaction. *Int. J. Miner. Process.* **2000**, *60*, 229-245.
  10. Li, J.; Lewis, R. B.; Dahn, J. R. Sodium carboxymethyl cellulose: A potential binder for Si negative electrodes for Li-ion batteries. *Electrochem. Solid-State Lett.* **2007**, *10*, A17-A20.
  11. Lee, J. -H.; Paik, U.; Hackley, V. A.; Choi, Y. -M. Effect of carboxymethyl cellulose on aqueous processing of natural graphite negative electrodes and their electrochemical performance for lithium batteries. *J. Electrochem. Soc.* **2005**, *152*, A1763-A1769.
  12. Hoogendam, C. W.; de Keizer, A.; Cohen Stuart, M. A.; Bijsterbosch, B. H. Adsorption mechanisms of carboxymethyl cellulose on mineral surfaces. *Langmuir* **1998**, *14*, 3825-3839.
  13. Barbucci, R.; Magnani, A.; Consumi, M. Swelling behavior of carboxymethylcellulose hydrogels in relation to cross-linking, pH, and charge density. *Macromolecules* **2000**, *33*, 7475-7480.
  14. Guillot, S.; Delsanti, M.; Désert, S.; Langevin, D. Surfactant-induced collapse of polymer chains and monodisperse growth of aggregates near the precipitation boundary in carboxymethylcellulose-DTAB aqueous solutions. *Langmuir* **2003**, *19*, 230-237.

15. Lopez, C. G.; Rogers, S. E.; Colby, R. H.; Graham, P.; Cabral, J. T. Structure of sodium carboxymethyl cellulose aqueous solutions: A SANS and rheology study. *J. Polym. Sci. B: Polym. Phys.* **2015**, *53*, 492-501.
16. Truzzolillo, D.; Bordi, F.; Cametti, C.; Sennato, S. Counterion condensation of differently flexible polyelectrolytes in aqueous solutions in the dilute and semidilute regime. *Phys. Rev. E* **2009**, *79*, 011804.
17. Kästner, U.; Hoffmann, H.; Dönges, R.; Hilbig, J. Structure and solution properties of sodium carboxymethyl cellulose. *Colloid. Surf.* **1997**, *123-124*, 307-328.
18. Ansarifar, A.; Wang, L.; Ellis, R. J.; Kirtley, S. P.; Riyazuddin, N. Enhancing the mechanical properties of styrene-butadiene rubber by optimizing the chemical bonding between silanized silica nanofiller and the rubber. *J. Appl. Polym. Sci.* **2007**, *105*, 322-332.
19. Schuman, T.; Wikström, M.; Rigdahl, M. Dispersion coating with carboxylated and cross-linked styrene-butadiene lattices. 1. Effect of some polymer characteristics on film properties. *Prog. Org. Coat.* **2004**, *51*, 220-227.
20. Stephen, R.; Ranganathaiah, C.; Varghese, S.; Joseph, K.; Thomas, S. Gas transport through nano and micro composites of natural rubber (NR) and their blends with carboxylated styrene butadiene rubber (XSBR) latex membranes. *Polymer* **2006**, *47*, 858-870.
21. Zang, Y. -H.; Du, J.; Du, Y.; Wu, Z.; Cheng, S.; Liu, Y. The migration of styrene butadiene latex during the drying of coating suspensions: When and how does migration of colloidal particles occur?. *Langmuir* **2010**, *26*, 18331-18339.

22. Li, C. -C.; Wang, Y. -W. Importance of binder compositions to the dispersion and electrochemical properties of water-based LiCoO<sub>2</sub> cathodes. *J. Power Sources* **2013**, *227*, 204-210.
23. Hagiwara, H.; Suszynski, W. J.; Francis, L. F. A Raman spectroscopic method to find binder distribution in electrodes during drying. *J. Coat. Technol. Res.* **2014**, *11*, 11-17.
24. Lee, G. -W.; Ryu, J. H.; Han, W.; Ahn, K. H.; Oh, S. M. Effect of slurry preparation process on electrochemical performances of LiCoO<sub>2</sub> composite electrode. *J. Power Sources* **2010**, *195*, 6049-6054.
25. Ponrouch, A.; Palacín, M. R. On the impact of the slurry mixing procedure in the electrochemical performance of composite electrodes for Li-ion batteries: A case study for mesocarbon microbeads (MCMB) graphite and Co<sub>3</sub>O<sub>4</sub>. *J. Power Sources* **2011**, *196*, 9682-9688.
26. Kim, J.; Kim, B.; Lee, J. -G.; Cho, J.; Park, B. Direct carbon-black coating on LiCoO<sub>2</sub> cathode using surfactant for high-density Li-ion cell. *J. Power Sources* **2005**, *139*, 289-294.
27. Li, C. -C.; Lee, J. -T.; Peng, X. -W. Improvements of dispersion homogeneity and cell performance of aqueous-processed LiCoO<sub>2</sub> cathodes by using dispersant of PAA-NH<sub>4</sub>. *J. Electrochem. Soc.* **2006**, *153*, A809-A815.
28. Lee, J. -T.; Chu, Y. -J.; Peng, X. -W.; Wang, F. -M.; Yang, C. -R.; Li, C. -C. A novel and efficient water-based composite binder for LiCoO<sub>2</sub> cathodes in lithium-ion batteries. *J. Power Sources* **2007**, *173*, 985-989.

29. Lee, J. -H.; Paik, U.; Hackley, V. A.; Choi, Y. -M. Effect of poly(acrylic acid) on adhesion strength and electrochemical performance of natural graphite negative electrode for lithium-ion batteries. *J. Power Sources* **2006**, *161*, 612-616.
30. Nguyen, B. P. N.; Chazelle, S.; Cerbelaud, M.; Porcher, W.; Lestriez, B. Manufacturing of industry-relevant silicon negative composite electrodes for lithium ion-cells. *J. Power Sources* **2014**, *262*, 112-122.
31. Kim, S.; Hyun, K.; Kim, Y. S.; Struth, B.; Clasen, C.; Ahn, K. H. Drying of a charge-stabilized colloidal suspension in situ monitored by vertical small angle X-ray scattering. *Langmuir* **2013**, *29*, 10059-10065.
32. Lee, J. Y.; Hwang, J. W.; Jung, H. W.; Kim, S. H.; Lee, S. J.; Yoon, K.; Weitz D. A. Fast dynamics and relaxation fo colloidal drops during the drying process using multispeckle diffusing wave spectroscopy. *Langmuir* **2013**, *29*, 861-866.
33. Buss, F.; Roberts, C. C.; Crawford, K. S.; Peters, K.; Francis, L. F. Effect of soluble polymer binder on particle distribution in a drying particulate coating. *J. Colloid Interface Sci.* **2011**, *359*, 112-120.
34. Luo, H.; Cardinal, C. M.; Scriven, L. E.; Francis, L. F. Ceramic nanoparticle/monodisperse latex coatings. *Langmuir* **2008**, *24*, 5552-5561.
35. Lim, S.; Ahn, K. H.; Yamamura, M. Latex migration in battery slurries during drying. *Langmuir* **2013**, *29*, 8233-8244.
36. Porcher, W.; Lestriez, B.; Jouanneau, S.; Guyomard, D. Design of aqueous processed thick LiFePO<sub>4</sub> composite electrodes for high-energy lithium battery. *J. Electrochem. Soc.* **2009**, *156*, A133-A144.

37. Li, C. -C.; Wang, Y. -W. Binder distributions in water-based and organic-based LiCoO<sub>2</sub> electrode sheets and their effects on cell performance. *J. Electrochem. Soc.* **2011**, *158*, A1361-A1370.
38. Payne, J. A.; McCormick, A. V.; Francis, L. F. In situ stress measurement apparatus for liquid applied coatings. *Rev. Sci. Instrum.* **1997**, *68*, 4564-4568.
39. Lei, H.; Francis, L. F.; Gerberich, W. W.; Scriven, L. E. Stress development in drying coatings after solidification. *AIChE J.* **2002**, *48*, 437-451.
40. Francis, L. F.; McCormick, A. V.; Vaessen, D. M.; Payne, J. A. Development and measurement of stress in polymer coatings. *J. Mater. Sci.* **2002**, *37*, 4717-4731.
41. Kim, S.; Sung, J. H.; Hur, K.; Ahn, K. H.; Lee, S. J. The effect of adsorption kinetics on film formation of silica/PVA suspension. *J. Colloid Interface Sci.* **2010**, *344*, 308-314.
42. Kim, S.; Sung, J. H.; Ahn, K. H.; Lee, S. J. Drying of the silica/PVA suspension: Effect of suspension microstructure. *Langmuir* **2009**, *25*, 6155-6161.
43. Kim, S.; Sung, J. H.; Chun, S.; Ahn, K. H.; Lee, S. J. Adsorption-stress relationship in drying/PVA suspensions. *J. Colloid Interface Sci.* **2011**, *361*, 497-502.
44. Wedin, P.; Lewis, J. A.; Bergström, L. Soluble organic additive effects on stress development during drying of calcium carbonate suspension. *J. Colloid Interface Sci.* **2005**, *290*, 134-144.
45. Wedin, P.; Martinez, C. J.; Lewis, J. A.; Daicic, J.; Bergström, L. Stress development during drying of calcium carbonate suspensions containing

- carboxymethylcellulose and latex particles. *J. Colloid Interface Sci.* **2004**, *272*, 1-9.
46. Martinez, C. J.; Lewis, J. A. Shape evolution and stress development during latex-silica film formation. *Langmuir* **2002**, *18*, 4689-4698.
47. Tirumkudulu, M. S.; Russel, W. B. Role of capillary stresses in film formation. *Langmuir* **2004**, *20*, 2947-2961.
48. Kiennemann, J.; Chartier, T.; Pagnoux, C.; Baumard, J.F.; Huger, M.; Laméran, J. M. Drying mechanisms and stress development in aqueous alumina tape casting. *J. Eur. Ceram. Soc.* **2005**, *25*, 1551-1564.
49. Lewis, J. A.; Blackman, K. A.; Ogden, A. L.; Payne, J. A.; Francis, L. F. Rheological property and stress development during drying of tape-cast ceramic layers. *J. Am. Ceram. Soc.* **1996**, *79*, 3225-3234.
50. Price, K.; Wu, W.; Wood, K.; Kong, S.; McCormick, A.; Francis, L. Stress development and film formation in multiphase composite latexes. *J. Coat. Technol. Res.* **2014**, *11*, 827-839.
51. Leong, Y. K.; Boger, D. V.; Christie, G. B.; Mainwaring, D. E. Rheology of low viscosity, high concentration brown coal suspensions. *Rheol Acta* **1993**, *32*, 277-285.
52. Kapur, P. C.; Scales, P. J.; Boger, D. V.; Healy, T. W. Yield stress of suspensions loaded with size distributed particles. *AIChE J.* **1997**, *43*, 1171-1179.
53. Scales, P. J.; Johnson, S. B.; Healy, T. W.; Kapur, P. C. Shear yield stress of partially flocculated colloidal suspensions. *AIChE J.* **1998**, *44*, 538-544.

54. Walls, H. J.; Brett Caines, S.; Sanchez, A. M.; Khan, S. A. Yield stress and wall slip phenomena in colloidal silica gels. *J. Rheol.* **2003**, *47*, 847-868.
55. Boger, D. V.; Scales, P. J.; Sofra, F. Rheological concepts. In: Jewell, R.; Fourie, A.; Lord, E. (Eds.), *Paste and Thickened Tails. A Guide*. UWA Press, Perth, Australia, **2002**, 23-34.
56. Johnson, S. B.; Franks, G. V.; Scales, P. J.; Boger, D. V.; Healy, T. W. Surface chemistry-rheology relationships in concentrated mineral suspensions. *Int. J. Miner. Process.* **2000**, *58*, 267-304.
57. Zhou, Z.; Solomon, M. J.; Scales, P. J.; Boger, D. V. The yield stress of concentrated flocculated suspensions of size distributed particles. *J. Rheol.* 1999, *43*, 651-671.
58. Zhou, Z.; Scales, P. J.; Boger, D. V. Chemical and physical control of the rheology of concentrated metal oxide suspensions. *Chem. Eng. Sci.* **2001**, *56*, 2901-2920.
59. Nguyen, Q. D.; Boger, D. V. Yield stress measurement for concentrated suspensions. *J. Rheol.* **1983**, *27*, 321-349.
60. Nguyen, Q. D.; Boger, D. V. Measuring the flow properties of yield stress fluids. *Annu. Rev. Fluid Mech.* **1992**, *24*, 47-88.
61. Nguyen, Q. D.; Boger, D. V. Direct yield stress measurement with the vane method. *J. Rheol.* **1985**, *29*, 335-347.
62. Pashias, N.; Boger, D. V.; Summers, J.; Glenister, D. J. A fifty cent rheometer for yield stress measurement. *J. Rheol.* **1996**, *40*, 1179-1189.

63. Hunter, R. J.; Nicol, S. K. The dependence of plastic flow behavior of clay suspensions on surface properties. *J. Colloid Interface Sci.* **1968**, *28*, 250-259.
64. Firth, B. A. Flow properties of coagulated colloidal suspensions. II. Experimental properties of the flow curve parameters. *J. Colloid Interface Sci.* **1976**, *57*, 257-265.
65. Firth, B. A.; Hunter, R. J. Flow properties of coagulated colloidal suspensions. III. The elastic floc model. *J. Colloid Interface Sci.* **1976**, *57*, 266-275.
66. Flatt, R. J.; Bowen, P. Yodel: A yield stress model for suspensions. *J. Am. Ceram. Soc.* **2006**, *89*, 1244-1256.
67. Franks, G. V. Zeta potentials and yield stresses of silica suspensions in concentrated monovalent electrolytes: Isoelectric point shift and additional attraction. *J. Colloid Interface Sci.* **2002**, *249*, 44-51.
68. Jiang, J.; Oberdörster, G.; Biswas, P. Characterization of size, surface charge, and agglomeration state of nanoparticle dispersions for toxicological studies. *J. Nanopart. Res.* **2009**, *11*, 77-89.
69. Flood, C.; Cosgrove, T.; Espidel, Y.; Howell, I.; Revell, P. Effects of surfactants and electrolytes on adsorbed layers and particle stability. *Langmuir* **2008**, *24*, 7323-7328.
70. Dijt, J. C.; Cohen Stuart, M. A.; Hofman, J. E.; Fleer, G. J. Kinetics of polymer adsorption in stagnation point flow. *Colloids Surf.* **1990**, *51*, 141-158.
71. Vasina, E. N.; Déjardin, P. Adsorption of  $\alpha$ -chymotrypsin onto mica in laminal flow conditions. Adsorption kinetic constant as a function of tris buffer concentration at pH 8.6. *Langmuir* **2004**, *20*, 8699-8706.



72. Zhulina, E. B.; Borisov, O. V.; Priamitsyn, V. A. Theory of steric stabilization of colloid dispersions by grafted polymers. *J. Colloid interface Sci.* **1990**, *137*, 495-511.
73. Asakura, S.; Oosawa, F. Interaction between particles suspended in solutions of macromolecules. *J. Polym. Sci.* **1958**, *33*, 183-192.
74. Seebergh, J. E.; Berg, J. C. Depletion flocculation of aqueous, electrosterically-stabilized latex dispersions. *Langmuir* **1994**, *10*, 454-463.
75. Burns, J. L.; de Yan, Y.; Jameson, G. J.; Biggs, S. The effect of molecular weight of nonadsorbing polymer on the structure of depletion-induced flocs. *J. Colloid Interface Sci.* **2002**, *247*, 24-32.
76. Hintennach, A.; Novák, P. Influence of surfactants and viscosity in the preparation process of battery electrodes containing nanoparticles. *Phys. Chem. Chem. Phys.* **2009**, *11*, 9484-9488.
77. Patey, T. J.; Hintennach, A.; La Mantia, F.; Novák, P. Electrode engineering of nanoparticles for lithium-ion batteries –Role of dispersion technique. *J. Power Sources* **2009**, *189*, 590-593.
78. Li, C. -C.; Lin, Y. -S. Interactions between organic additives and active powders in water-based lithium iron phosphate electrode slurries. *J. Power Sources* **2012**, *220*, 413-421.
79. Basu, S. K.; Scriven, L. E.; Francis, L. F.; McCormick, A. V. Mechanism of wrinkle formation in curing coatings. *Prog. Org. Coat.* **2005**, *53*, 1-16.

80. Yamamura, M.; Nishio, T.; Kajiwara, T.; Adachi, K. Effect of stepwise change of drying rate on microstructure evolution in polymer films. *Drying Technol.* 2001, 19, 1397-1410.
81. Payne, J. A. Stress evolution in solidifying coatings. *Ph.D. thesis*, University of Minnesota, **1998**, available from University Microfilm International, Ann Arbor, MI.
82. Ma, Y.; Davis, H. T.; Scriven, L. E. Microstructure development in drying latex coatings. *Prog. Org. Coat.* **2005**, 52, 46-62.
83. Stamou, D.; Duschl, C. Long-range attraction between colloidal spheres at the air-water interface: The consequence of an irregular meniscus. *Phys. Rev. E* **2000**, 62, 5263-5272.
84. Trueman, R. E.; Lago Domingues, E.; Emmett, S. N.; Murray, M. W.; Keddie, J. L.; Routh, A. F. Autostratification in drying colloidal dispersions: Experimental investigations. *Langmuir* **2012**, 28, 3420-3428.
85. Nikiforow, I.; Adams, J.; König, A. M.; Langhoff, A.; Pohl, K.; Turshatov, A.; Johannsmann, D. Self-stratification during film formation from latex blends driven by difference in collective diffusivity. *Langmuir* **2010**, 26, 13162-13167.
86. Yamazaki, K.; Nishioka, T.; Hattori, Y.; Fujita, K. Print mottle effect of binder migration and latex film formation during coating consolidation. *Tappi J.* **1993**, 76, 79-84.
87. Engström, G.; Rigdahl, M.; Kline, J.; Ahlroos, J. Binder distribution and mass distribution of the coating layer – cause and consequence. *Tappi J.* **1991**, 74, 171-179.

88. Kline, J. E. Measuring binder migration with ultraviolet analysis. *Tappi J.* **1991**, *74*, 177-182.
89. Cardinal, C. M.; Jung, Y. D.; Ahn, K. H.; Francis, L. F. Drying regime maps for particulate coatings. *AIChE J.* **2010**, *56*, 2769-2780.
90. Routh, A. F.; Zimmerman, W. B. Distribution of particles during solvent evaporation from films. *Chem. Eng. Sci.* **2004**, *59*, 2961-2968.
91. Yamamura, M. In-situ characterization of drying particulate coatings. *KONA Powder Particle J.* **2011**, *29*, 39-52.
92. Deegan, R. D.; Bakajin, O.; Dupont, T. F.; Huber, G.; Nagel, S. R.; Witten, T. A. Capillary flow as the cause of ring stains from dried liquid drops. *Nature* **1997**, *389*, 827-829.
93. Deegan, R. D.; Bakajin, O.; Dupont, T. F.; Huber, G.; Nagel, S. R.; Witten, T. A. Contact line deposits in an evaporating drop. *Phys. Rev. E* **2000**, *62*, 756-765.
94. Hu, H.; Larson, R. G. Evaporation of a sessile droplet on a substrate. *J. Phys. Chem. B* **2002**, *106*, 1334-1344.
95. Hu, H.; Larson, R. G. Analysis of the microfluid flow in an evaporating sessile droplet. *Langmuir* **2005**, *21*, 3963-3971.
96. Ristenpart, W. D.; Kim, P. G.; Domingues, C.; Wan, J.; Stone, H. A. Influence of substrate conductivity on circulation reversal in evaporating drops. *Phys. Rev. Lett.* **2007**, *99*, 234502.
97. Yunker, P. J.; Still, T.; Lohr, M. A.; Yodh, A. G. Suppression of the coffee-ring effect by shape-dependent capillary interactions. *Nature* **2011**, *476*, 308-311.

98. Weon, B. M.; Je, J. H. Capillary force repels coffee-ring effect. *Phys. Rev. E* **2010**, *82*, 015305.
99. Corcoran, E. M. Determining stresses in organic coatings using plate beam deflection. *J. Paint Technol.* **1969**, *41*, 635-640.
100. Moraru, V.; Lebovka, N.; Shevchenko, D. Structural transitions in aqueous suspensions of natural graphite. *Colloids Surf. A Physicochem. Eng. Aspects* **2004**, *242*, 181-187.
101. Graessley, W. W.; Polymer chain dimensions and the dependence of viscoelastic properties on concentration, molecular weight and solvent power. *Polymer* **1980**, *21*, 258-262.
102. Chambon, F.; Winter, H. H. Linear viscoelasticity at the gel point of a crosslinking PDMS with imbalanced stoichiometry. *J. Rheol.* **1987**, *31*, 683-697.
103. Piau, J. M. Carbopol gels: Elastoviscoplastic and slippery glasses made of individual swollen sponges. Meso-and macroscopic properties, constitutive equations and scaling laws. *J. Non-Newtonian Fluid Mech.* **2007**, *144*, 1-29.
104. Müller, T.; Hakert, H.; Eckert, Th. Rheological and electron microscopic characterization of aqueous carboxymethyl cellulose gels Part II: Visualization of the gel structure by freeze-fracturing. *Colloid Polym. Sci.* **1989**, *267*, 230-236.
105. Shaw, D. J. The solid-gas interface. *Introduction to colloid and surface chemistry*, 4<sup>th</sup> edition; Butterworth-Heinemann Ltd.: London, **1992**; p 126.
106. Mattson, S.; Nyström, C. The use of mercury porosimetry in assessing the effect of different binders on the pore structure and bonding properties of tablets. *Eur. J. Pharm. Biopharm.* **2001**, *52*, 237.

107. Lestriez, B.; Bahri, S.; Sandu, I.; Roué, L.; Guyomard, D. On the binding mechanism of CMC in Si negative electrodes for Li-ion batteries. *Electrochem. Comm.* **2007**, *9*, 2801-2806.
108. Kajiya, T.; Kaneko, D.; Doi, M. Dynamical visualization of “Coffee stain phenomenon” in droplets of polymer solution via fluorescent microscopy. *Langmuir* **2008**, *24*, 12369-12374.
109. Ciddor, P. E. Refractive index of air: New equations for the visible and near infrared. *Appl. Opt.* **1996**, *35*, 1566-1573.
110. Schiebener, P.; Straub, J.; Levelt Sengers, J. M. H.; Gallagher, J. S. Refractive index of water and steam as function of wavelength, temperature and density. *J. Phys. Chem. Ref. Data* **1990**, *19*, 677-717.
111. Kasarova, S. N.; Sultanova, N. G.; Ivanov, C. D.; Nikolov, I. D. Analysis of the dispersion of optical plastic materials. *Opt. Mater.* **2007**, *29*, 1481-1490.
112. Hermans, J., Jr. Investigation of elastic properties of particle network in gelled solutions of hydrocolloids. I. Carboxymethyl cellulose. *J. Polym. Sci. Polym. Chem.* **1965**, *3*, 1859-1868.
113. Huggins, M. L. The viscosity of dilute solutions of long-chain molecules. IV. Dependence on concentration. *J. Am. Chem. Soc.* **1942**, *64*, 2716-2718.
114. Kraemer, E. O. Molecular weights of celluloses and cellulose derivatives. *Ind. Eng. Chem.* **1938**, *30*, 1200-1203.
115. Kurata, M.; Tsunashima, Y. Viscosity-molecular weight relationships and unperturbed dimensions of linear chain molecules. In *Polymer handbook*, 4<sup>th</sup>

- Edition; Brandrup, J.; Immergut, E. H.; Grulke, E. A., Eds.; John Wiley & Sons, Inc.: New York, **1999**; pp VIII-83.
116. Wang, Y. Z.; Li, B. H.; Xiong, X. M.; Wang, B.; Zhang, J. X. Universal scaling description of the strain-softening behavior in the semidilute uncross-linked polyacrylamide-water solution. *Soft Matter* **2010**, *6*, 3318-3324.
117. Hamada, H.; Enomae, T.; Shibata, I.; Isogai, A.; Onabe, F. In *Effects of water-soluble cellulose polymers on coating development and quality*, Proceedings of PITA Coating Conference, Edinburgh, Great Britain, March 4-5, **2003**; Edinburgh, Great Britain, March 4-5, 2003; pp 91-95.
118. Du, Y.; Zang, Y. -H.; Du, J. Effects of starch on latex migration and on paper coating properties. *Ind. Eng. Chem. Res.* **2011**, *50*, 9781-9786.
119. Bajpai, A. K.; Mishra, A. Ionizable Interpenetrating polymer networks of carboxymethyl cellulose and polyacrylic acid: Evaluation of water uptake. *J. Appl. Polym. Sci.* **2004**, *93*, 2054-2065.
120. Pawlik, M.; Laskowski, J. S.; Ansari, A. Effect of carboxymethyl cellulose and ionic strength on stability of mineral suspensions in potash ore flotation systems. *J. Colloid Interface Sci.* **2003**, *260*, 251-258.
121. Horigome, M.; Otsubo, Y. Long-time relaxation of suspensions flocculated by associating polymers. *Langmuir* **2002**, *18*, 1968-1973.
122. Pickrahn, K.; Rajaram, B.; Mohraz, A. Relationship between microstructure, dynamics, and rheology in polymer-bridging colloidal gels. *Langmuir* **2009**, *26*, 2392-2400.

123. Runkana, V.; Somasundaran, P.; Kapur, P. C. A population balance model for flocculation of colloidal suspensions by polymer bridging. *Chem. Eng. Sci.* **2006**, *61*, 182-191.
124. Keddie, J. L.; Routh, A. F. An introduction to latex and the principles of colloidal stability. In *Fundamentals of latex film formation: Processes and properties*, 1st Edition; Pasch, H.; Alig, I.; Janca, J.; Kulicke, W. -M., Eds.; Springer: Dordrecht, **2010**; pp 1-26.

## 국문 초록

본 연구에서는 리튬 이온 배터리 음극 슬러리에서 바인더가 슬러리의 미세 구조와 건조 경향에 미치는 영향에 대해 고찰하였다.

먼저, 슬러리의 유변 거동과 cryo-SEM 사진을 통하여 바인더가 슬러리의 미세 구조 형성에 미치는 영향에 대해 알아보았다. 흑연 입자는 수계 시스템에서 그들의 소수성에 의해 응집을 일으키고 겔 구조를 형성한다. 이 때 sodium carboxymethyl cellulose (CMC) 또는 styrene butadiene rubber (SBR) 이 첨가되었을 때, 이들 바인더는 흑연 입자 표면에 흡착함으로써 응집체를 분산 시키는 역할을 한다. 한편, CMC 와 SBR 이 동시에 함유된 슬러리의 경우 CMC 의 농도에 따라 서로 다른 미세 구조가 형성된다. 즉, 낮은 농도의 CMC 가 함유된 슬러리의 경우 SBR 이 흑연 입자 표면에 흡착하면서 입자 분산을 일으킨다. 반면, 높은 농도의 CMC 가 함유된 슬러리의 경우 흑연 입자 표면에 우선적으로 흡착된 CMC 에 의해 SBR 은 더 이상 흡착하지 못하고 입자 분산에 큰 영향을 미치지 못하는 것을 확인하였다.

다음으로 음극 슬러리의 건조 특성을 건조 스트레스 발달 경향을 통해 알아보았고, 바인더가 건조 후 필름의 미세 구조에 미치는 영향에 대해 알아보았다. 건조 스트레스 발달 경향은 켈틸레머 굴절 방법을, 그리고 필름 미세구조는 수은 주입법을 이용하였다. 흑연/SBR 슬러리에서 SBR 의 농도가 증가함에 따라 필름의 잔류 스트레스가 증가하게 되고 건조 후 필름 내 공극도 줄어들게 된다. 이는 SBR 이 흑연 입자들 사이에 형성된 공극을 메워줌으로써 나타나는 현상이다. 또한 흑연/CMC 슬러리에서는



CMC 가 흑연 입자 표면에 흡착함으로써 흑연 입자간의 응집력을 향상시키면서 건조 스트레스를 증가시키고 필름 내 공극을 줄여주는 역할을 한다. CMC 와 SBR 이 모두 함유된 슬러리의 경우 앞선 슬러리의 미세 구조와 마찬가지로 CMC 의 농도에 따라 다른 건조 특성이 나타난다. 즉, 낮은 농도의 CMC 가 함유된 슬러리의 경우 SBR 의 농도가 증가함에 따라 필름의 잔류 스트레스가 증가하는데 반해, 높은 농도의 CMC 가 함유된 슬러리의 경우 SBR 의 농도에 상관없이 일정한 잔류 스트레스를 갖는 것을 확인하였다. 필름의 잔류 스트레스는 필름의 기계적 강도로 생각할 수 있는데, CMC 가 필름의 기계적 강도를 증가시키는데 지배적인 역할을 하고 있음을 알 수 있다. 또한 건조 스트레스 발달 경향을 바탕으로 충분한 기계적 강도를 갖는 필름을 형성하는 바인더 농도에 관한 공정 윈도우를 작성하였다.

마지막으로, 슬러리 건조 공정 중 발생하는 입자의 이동 현상을 형광 현미경 방법을 통해 알아보았다. 형광 현미경 방법은 배터리 슬러리와 같이 불투명한 샘플도 사용이 가능하고, 입자의 이동 현상을 실시간으로 파악할 수 있는 장점이 있다. CMC 고분자 용액 내에서 높은 함량의 CMC 가 함유되었을 경우, CMC 의 망사 구조에 의해 라텍스 입자의 이동 현상이 억제되어 균일한 입자 분포를 갖는 필름이 형성된다. 반면 낮은 농도의 CMC 가 함유되었을 경우, 불균일한 입자 분포를 갖는 필름이 형성되는 것을 확인하였다. 흑연 입자가 함유된 슬러리의 경우, 슬러리의 미세 구조가 라텍스 입자의 이동 현상에 영향을 미치는 것을 확인하였다. 흡착되지 못한 CMC 에 의해 흑연 입자가 응집체를 형성하여 불안정한 상태의 슬러리의 경우, 건조 중 라텍스가 필름 표면 쪽으로 이동하는 반면,

흡착된 CMC 에 의해 흑연 입자가 분산되어 안정한 상태의 슬러리의 경우 입자 이동 현상이 나타나지 않았다.

본 연구를 통해 바인더가 슬러리의 미세구조, 그리고 건조 경향 및 필름의 미세구조에 미치는 영향에 대한 이해를 바탕으로 개선된 성능의 배터리를 위한 슬러리 디자인에 도움을 줄 수 있을 것이다. 또한 건조 공정 중 발생하는 입자 이동 현상 메커니즘을 알아봄으로써 균일한 입자 분포를 갖는 필름을 생산하는 데 기여할 것으로 기대된다.

주요어: 리튬 이온 배터리 음극 슬러리, 미세구조, 건조 스트레스, 필름  
미세구조, 입자 이동현상

학 번: 2012-30957

# Curriculum Vitae

---

**Sanghyuk Lim**

School of Chemical and Biological

Seoul National University

Bd.302, #615, 1 Gwanak-ro

Gwanak-gu, Seoul

Tel: +82-2-880-9125

Cell: +82-10-3371-5650

sh2098@snu.ac.kr

---

**Education**      **Seoul National University**

Ph.D., Chemical Engineering, expected 2015

M.S., Chemical Engineering, 2012

Thesis: Yield and flow measurement of fine and coarse binary  
particulate mineral slurries

Advisors: Professor Seung Jong Lee and Professor Kyung Hyun

Ahn

**Inha University**

B.S., Polymer Engineering, 2008

**Research**      **Seoul National University**

**Experience**      Coating

Investigation of rheological properties and flow characterization  
of oil paint

#### **Seoul National University and The University of Melbourne**

Rheological property of binary particulate slurry

Establish of methodology for predicting gel point, close packing  
fraction and shear rheology of particulate slurries containing a  
binary mixture of fine and coarse materials

#### **Seoul National University and Kyushu Institute of Technology**

Drying of battery slurry

Investigation of latex migration during drying in battery slurries  
using fluorescence microscopy

#### **Seoul National University**

Microstructure of battery slurry

Investigation of microstructure of battery slurry depending on  
particle and binder concentration

#### **Experience Visiting scholar**

Chemical and Biomolecular Engineering, The University of  
Melbourne, Australia (*July, 2010 ~ June, 2011*)

Advisor: Professor Peter J. Scales

Department of Applied Chemistry, Kyushu Institute of Technology,  
Japan (*Jan., 2012 ~ June, 2012*)

Advisor: Professor Masato Yamamura

### **Military service**

Served in Republic of Korea Army (March, 2004 ~ March 2006)

### **Research**

#### **Paper**

**Sanghyuk Lim**, Kyung Hyun Ahn, Seung Jong Lee, Ashish Kumar, Nicky Duan, Xiaodan Sun, Shane P. Usher, and Peter J. Scales\*. Yield and flow measurement of fine and coarse binary particulate mineral slurries. *International Journal of Mineral Processing* 119 (2013) 6-15

**Sanghyuk Lim** and Kyung Hyun Ahn\*. Rheological properties of oil paints and their flow instabilities in blade coating. *Rheologica Acta* 52 (2013) 643-659

**Sanghyuk Lim**, Kyung Hyun Ahn, and Masato Yamamura\*. Latex migration in battery slurries during drying. *Langmuir* 29 (2013) 8233-8244

**Sanghyuk Lim**, Sunhyung Kim, Kyung Hyun Ahn\*, and Seung Jong Lee. Stress development of Li-ion battery anode slurries during the drying process. *Industrial & Engineering Chemistry Research* 54 (2015) 6146-6155

### **Awards**

Academic Achievement Scholarship (undergraduate)

Inha University (2004, 2006, 2007)

Academic Achievement Scholarship (graduate)

	Seoul National University (2009)
<b>Industrial</b>	Samsung Medical Center (2008)
<b>Project</b>	The effect of preheating on the rheological properties of dental composite under different deformation condition
<b>Participated</b>	Korea Electric Power Corporation (2008)
	TiO <sub>2</sub> paste in solar cell (Rheological properties and drying stress measurement)
	SK Energy & SK Mobile Energy (2009)
	Stability and film formation of alumina suspension for Li-ion battery separator
	Drying mechanism and curl characterization of Tri-acetate cellulose film
	Characterization of film formation of Flexible Copper Clad Laminate
	Characterization of suspension stability and film formation of slurry for secondary battery
	SK Innovation (2011 ~ 2014)
	Characterization of suspension stability and film formation of slurry for Li-ion battery
	Dongjin Semichem (2013 ~ 2015)
	Characterization of rheological properties of paste for solar cell, touch panel display and Ag ink

Establish of relationship between rheological properties and printability of paste for screen printing and gravure printing

**Conference** Sanghyuk Lim, Jun Hee Sung, Kyung Hyun Ahn, and Seung Jong

**Proceedings** Lee. Oscillatory squeezing flow to measure the viscoelastic properties of dental composite resin. The Korean Society of Rheology 2008 Fall meeting. *Poster Presentation.*

**Sanghyuk Lim**, Jun Hee Sung, Kyung Hyun Ahn, and Seung Jong Lee. Shear and oscillatory squeezing flow to measure the viscoelastic properties of dental composite resin. The 4<sup>th</sup> International Workshop for Far East Asian Young Rheologists 2009, Thailand. *Poster Presentation.*

**Sanghyuk Lim**, Jun Hee Sung, Kyung Hyun Ahn, and Seung Jong Lee. Instabilities of oil paint in blade coating. The Korean Society of Rheology 2010 Spring meeting. *Oral Presentation.*

**Sanghyuk Lim**, Jun Hee Sung, Kyung Hyun Ahn, and Seung Jong Lee. Instabilities of oil paint in blade coating. The 5<sup>th</sup> International Workshop for Far East Asian Young Rheologists 2010, Korea. *Oral Presentation.*

**Sanghyuk Lim**, Shane P. Usher, Peter J. Scales, Kyung Hyun Ahn, and Seung Jong Lee. Yield and flow behavior of fine and coarse

particulate slurries. The 6<sup>th</sup> Korean-Australian Rheology Conference 2011, Korea. *Oral Presentation*.

**Sanghyuk Lim**, Kyung Hyun Ahn, and Masato Yamamura. Latex migration during drying of battery slurries. The 4<sup>th</sup> Asian Coating Workshop 2012, Taiwan. *Oral Presentation*.

**Sanghyuk Lim**, Kyung Hyun Ahn, and Masato Yamamura. Latex migration during drying of Li-ion battery slurry. The Korean Institute of Chemical Engineers 2012 Fall meeting. *Oral Presentation*.

**Sanghyuk Lim**, Kyung Hyun Ahn, and Masato Yamamura. The mechanism of latex migration during drying of battery slurry. The Korean Society of Rheology 2012 Fall meeting. *Oral Presentation*.

**Sanghyuk Lim** and Kyung Hyun Ahn. The mechanism of microstructural change during drying of PMMA suspension. The Korean Institute of Chemical Engineers 2013 Spring meeting. *Oral Presentation*.

**Sanghyuk Lim**, Kibyeok son, and Kyung Hyun Ahn. Microstructural change of PMMA suspension during drying. The 5<sup>th</sup> Asian Coating Workshop 2013, Korea. *Oral Presentation*.

**Sanghyuk Lim**, Kyung Hyun Ahn, and Masato Yamamura. The mechanism of latex migration in battery slurries during drying using



fluorescence microscopy. European Coating Symposium 2013, Belgium. *Poster Presentation*.

**Sanghyuk Lim**, Kyung Hyun Ahn, and Masato Yamamura. Mechanism of latex migration in battery slurries during drying. The 9<sup>th</sup> International Workshop for Far East Asian Young Rheologists 2014, Korea. *Oral Presentation*.

**Sanghyuk Lim** and Kyung Hyun Ahn. Latex migration in battery slurries during drying: Effect of microstructure of slurry. The Korean Institute of Chemical Engineers 2014 Spring meeting. *Oral Presentation*.

**Sanghyuk Lim**, Seung Jong Lee, and Kyung Hyun Ahn. The mechanism of latex migration in battery slurry during drying: Effect of microstructure of slurry. The 6<sup>th</sup> Asian Coating Workshop 2014, Japan. *Oral & Poster Presentation*.

**Sanghyuk Lim**, Kyung Hyun Ahn, and Seung Jong Lee. Microstructure of anode slurry for Li-ion battery and its stress development during drying process. The Korean Society of Rheology 2014 Fall meeting. *Oral Presentation*.

**Sanghyuk Lim**, Sunhyung Kim, Kyung Hyun Ahn, and Seung Jong Lee. Microstructure of anode slurry for Li-ion battery and its mechanism of stress development during drying process. The Korean

Institute of Chemical Engineers 2015 Spring meeting. *Oral Presentation.*

**Sanghyuk Lim**, Sunhyung Kim, Kyung Hyun Ahn and Seung Jong Lee. Microstructure of anode slurry for Li-ion battery and its mechanism of stress development during drying process. The Korean Institute of Chemical Engineers 2015 Spring meeting. *Oral Presentation.*

**Sanghyuk Lim**, Kyung Hyun Ahn and Seung Jong Lee. Effect of binders on microstructure formation in Li-ion anode slurry. The 7<sup>th</sup> Asian Coating Workshop 2015, China. *Oral & Poster Presentation.*

**Sanghyuk Lim**, Sunhyung Kim, Kyung Hyun Ahn and Seung Jong Lee. Mechanism of microstructure formation in anode slurry and dried film for Li-ion battery. The 31<sup>th</sup> International Conference of the Polymer Processing Society, Korea. *Oral Presentation.*